A NEW METHOD OF POSITION AND FORCE

CONTROL FOR

ROBOTIC DEBURRING AND GRINDING

By

KUO-SHU TING

Diploma

Mingchi Institute of Technology

Taipei, Taiwan

1991

Submitted to the Faculty of the
Graduate College of the
Oklahoma State University
in partial fulfillment of
the requirements for
the Degree of
MASTER OF SCIENCE
December, 1996

A NEW METHOD OF POSITION AND FORCE

CONTROL FOR

ROBOTIC DEBURRING AND GRINDING

Thesis Approved:

____
Thesis Adviser

____

____

Thomas C. Collins
____
Dean of the Graduate College

ACKNOWLEDGMENTS

Countless thanks to Dr. Lawrence L. Hoberock, my major adviser, for his encouragement, advice, and many hours of guidance throughout by graduate program. Many thanks also go to Dr. Eduardo Misawa and Dr. Gary E. Young for serving on my committee. Their suggestions and support were very helpful throughout this study.

Thanks to Duli Hong for his literature review and earlier work. Financial support during my graduate study was provided by the Oklahoma Center for Integrated Design and Manufacturing, together with the Oklahoma Center for the Advancement of Science and Technology.

This work is dedicated to my mother, Jin-Yueh Lin, for her love, understanding, and encouragement over the years.

TABLE OF CONTENTS

LIST OF TABLES

LIST OF FIGURES

NOMENCLATURE

B	desired damping matrix
b	width of cut
$C(q,\dot{q})$	centrifugal and Coriolis matrix in joint space
$C_t(q)$	centrifugal and Coriolis matrix in task space
d	depth of cut
D	wheel diameter
E	modulus of elasticity
e_f	force error matrix
e_p	position error matrix
F	force vector arising from actuator torque at the end effector
F_d	desired force vector
F_e	external force vector acting on the end effector of the manipulator
$F_f(q)$	Coulomb friction force vector in the joints
$F_{ft}(q, \dot{q})$	friction force vector in task space
F_{jlim}	component of force limit
F_n	normal grinding force
F_t	tangential grinding force
$G(q)$	gravity vector in joint space
$G_t(q)$	gravity vector in task space
I	moment of inertia
$J(q)$	Jacobian matrix
K	desired stiffness matrix
K_d	derivative position gain matrix
K_f	proportional force gain matrix
K_{fi}	integral force gain matrix
K_p	derivative position gain matrix

$M(q)$	inertia matrix in joint space
M_d	desired inertia matrix
$M_t(q)$	inertial matrix in task space
q	joint variable vector
$\dot{q}$	the time derivative of q
s	Laplace operator
V	Lyapunov function
$\dot{V}$	derivative of Lyapunov function
v_n	normal velocity of end effector.
v_t	tangential velocity of end effector
V_w	workpiece feed rate
X	position vector in task space
X_d	desired position vector in task space
$\ddot{X}$	position acceleration
Z	impedance matrix
Z_e	scalar impedance
Z_w	material removal rate
Λ_m	metal removal parameter
μ	coefficient of grinding fiction
τ	input torque vector

CHAPTER I

INTRODUCTION

Automation Using Robotics

Traditional deburring and grinding of metal parts has been considered labor intensive, monotonous, and tedious work, occurring off-line, and often undertaken in dirty and noisy environments. Such manual clean-up operations usually increase costs and parts inconsistency. An alternative is to automate such operations, implemented by employing robots. Robots can be employed to good advantage in deburring and grinding because of the following properties:

- They can operate three shifts per day.
- They accurately reproduce repetitive motions.
- They can process parts faster than humans.
- They can work in noisy and dirty environments without degradation in performance.

For many companies, the use of robots for automation has considerably reduced costs and improved quality.

Robots have been successfully employed in the foundry industry for grinding gates, risers, and flash, as well as for various chamfering of internal and external edges [1].

Other industries have successfully employed robotic operations for brushing, polishing, buffing, and grinding [2]. Automatic parts being deburred and finished with robots include transmission and steering knuckle housings, connecting rods, and plastic moldings [2]. Robots also have been used for automatic welding and spray painting [3].

Industrial robots have been used for various deburring and finishing operations, but most applications are dedicated to large quantities of a specific part with simple geometry, easily adapted for automatic operation. Unlike off-line manual operations, the use of robotic deburring and grinding requires considerable planning to ensure optimum results. In this thesis, we consider robotic deburring and grinding whereby a robot arm carries a grinding tool (end effector) to follow a desired trajectory. This involves motion of the end effector in both free space and in constrained space. Development of an effective and efficient position and force control strategy is the main focus of this research. In next section, the problems addressed by this application are described.

Problem Background

In many robot applications, manipulators are commanded in more or less unconstrained environments. An unconstrained or "free" environment is a 3 dimensional work space in which there is no contact between the moving robot arms and any other objects, and no external force, other than gravity, acts on the end effector or other robot moving parts. Control of the position of the end effector in such environments is relatively straightforward. More advanced robotic applications involve interaction between the robot end effector, or other moving robot links, and the environment. Robotic deburring and grinding requires the end effector to follow a desired trajectory in both constrained and unconstrained space as illustrated in Figure 1.1. An important issue here is to design a controller to achieve stable contact transition and external force regulation with minimum impact and bouncing. Such a control strategy usually may be divided into three operation modes: free motion mode, transition or impact mode, and constrained motion mode [4]. In the transition and constrained motion mode, if a large burr is encountered, a sharp surface change may cause the end effector to leave the workpiece. Limit cycle response or instability may be excited. Therefore, appropriate control is important for efficient tool utilization and accurate production of desired finished profiles. A further concern in grinding is the potential of burning the workpiece or destruction of the tool if the grinding forces are excessive. This can be avoided by controlling the normal and tangential grinding forces to lie below the burning or damage limits for the given cutting conditions.

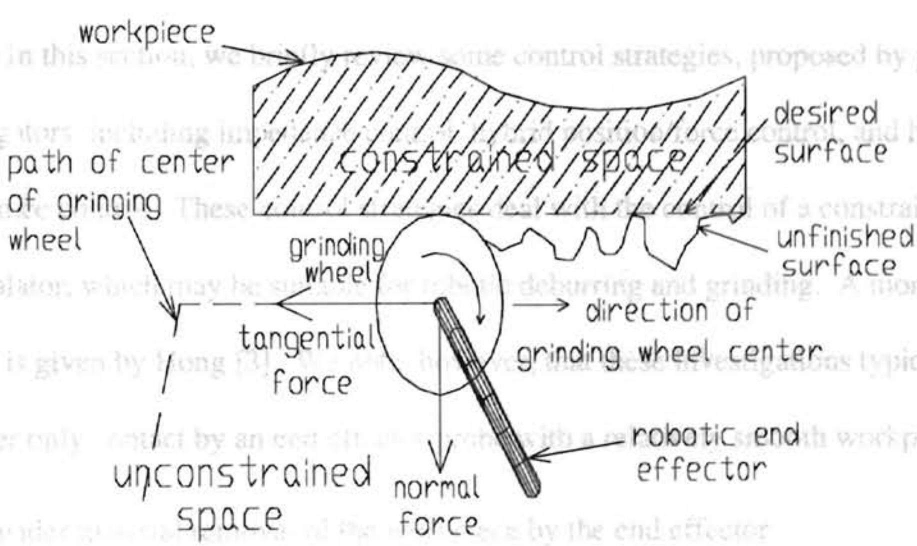

Figure 1.1 Grinding an Edge

Various investigators [5, 6, 7, 8] have proposed switching control strategies to handle the transition or impact modes. For example Marth, et al [8], employed position control in the unconstrained direction and force control in the constrained direction for a simple end effector probe contacting a smooth edge. However, such control approaches may not suitable for robotic deburring and grinding, because force control in a constrained direction requires tracking a desired force trajectory, which means a precise force model and known surface geometry are required. In robotic deburring and grinding, the end effector will encounter constrains in both tangential and normal directions, and we assume the geometry of the workpiece is not precisely known. Moreover force control in a constrained direction does not guarantee accurate production of a desired finished contour on the workpiece.

Literature Review

In this section, we briefly review some control strategies, proposed by previous investigators, including impedance control, hybrid position/force control, and hybrid impedance control. These control strategies deal with the control of a constrained manipulator, which may be suitable for robotic deburring and grinding. A more complete review is given by Hong [3]. We note, however, that these investigations typically consider only contact by an end effector probe with a relatively smooth workpiece, and do not consider material removal of the workpiece by the end effector.

Impedance Control

Impedance control was first proposed by Hogan in 1985 [9]. His central idea was to assume a relationship between the position of the end effector and the contact force exerted by the constraining environment. This relationship can be modeled by a generalized linear impedance consisting of inertial, damping, and stiffness characteristics. Impedance control regulates the relationship between the end effector position and the contact force, called the mechanical impedance [10]. The fundamental relationship is given by

$$Z(s) = \frac{F_e(s)}{X(s)} \tag{1.1}$$

where s is the Laplace operator and $F_e(s), X(s),$ and $Z(s)$ are the Laplace representations of the external force, position, and impedance, respectively. Typically, a generalized expression for the impedance is given by

$$Z(s) = M_d s^2 + Bs + K \tag{1.2}$$

where $M_d, B,$ and K represent desired inertia, damping, and stiffness, respectively. Impedance control has attracted a significant number of investigators, [11, 12, 13, 14], because it provides a stable and unified control structure for the three different regions of operation, namely, free motion, transition or impact, and constrained motion modes. On the other hand, unless the exact environment model is known and is integrated into the motion plan, the external force can not be independently regulated with impedance control after contact, such that, it is difficult to handle both position and force regulation in a constrained environment [4]. However, proper design of an impedance controller can guarantee the stability of manipulators in contact with environments. Details of impedance control will be addressed more completely in Chapter III, including stability analysis and controller design for robotic deburring and grinding.

Hybrid Position/Force Control

Hybrid position/force control, first proposed by Raibert and Craig [15], is a control strategy dealing with tasks requiring force control in some directions and position control in others. A hybrid position/force controller has the following three characteristics [16]:

- Position control is employed in directions for which a natural force constraint exists.
- Force control is employed in directions for which a natural position constraint exists.
- Appropriate combinations of force and position control modes are employed along the coordinates of an arbitrary reference frame.

Typically, a hybrid position/force controller is unable to regulate the relation between the end effector position and contact force because it neglects the manipulator's impedance. Moreover, the position of the end effector and contact force along one degree of freedom (DOF) can not be controlled independently, such that for complex tasks like robotic deburring and grinding, such a controller is unsuitable.

Hybrid Impedance Control

Hybrid impedance control combines impedance control and hybrid position/force control into one strategy [17]. It treats the contact environment as a linear impedance and assumes the manipulator can be effectively decoupled into single-DOF linear subsystems. Then, a duality principle is employed to decide which control should be used in each subsystem. In short, an inertial environment requires a position-controlled manipulator, a capacitive environment requires a force-controlled manipulator, and a resistive environment allows either force or position control [17]. Once the type of control method has been decided, the impedance of the end effector is chosen accordingly. Such a controller provides more flexibility than those mentioned earlier, and may be applied to robotic deburring and grinding. In Chapter III, we will further investigate and implement this control algorithm, and simulation results will presented in Chapter IV.

Impact Control

In robotic deburring and grinding, an impact force may occur when the end effector contacts the workpiece or encounters a large burr. This impulsive force may deviate the end effector off the workpiece. It could induce unstable dynamics and damage the end effector and workpiece. Strategies for impact control, or contact transition control, to solve this problem have been studied by several investigators. Such investigations may be broadly classified into two categories, namely, impedance control and switching control [4]. Impedance control is appealing because it provides a stable and unified control strategy for both free and constrained environments without the need for switching control algorithms on impact. Several switching (discontinuous) controllers have been investigated, mainly during the last five years. A common result is that while force can be regulated if contact is continuous, instability can arise if bouncing occurs after impact. Because of this, the overall contact stability problem has not been completely addressed for realistic deburring and grinding problems. Recently, Tarn, et al [4], proposed a new control strategy using "positive acceleration feedback to control the transient force response to reduce the peak impulsive force and bouncing". The new method employs a position control to eliminate the unexpected bouncing and reestablish contact. Tarn showed that the number of bounces is finite and that the last bounce always corresponds to the transition from free space to constrained space. Stable contact is guaranteed. Tarn's work may have potential for developing an improved control method for robotic deburring and grinding. In [18], Pagilla uses another approach for impact control. He assumes the end effector and environment are rigid, and there is no penetration. By employing a simple rigid body collision and coefficient of restitution to model impact, Pagilla experimentally and numerically shows that bouncing can be eliminated in finite time.

While the work reviewed above may have relevance to our problem herein, we note a significant difference. For robotic deburring and grinding, the robot arm carries a grinding wheel or deburring tool rotating at high speed. When the workpiece is contacted, such tools will immediately cut into workpiece such that the "hard" surface assumed by previous investigators immediately disappears. Accordingly, the impact force is likely much smaller in our operation, such that the approaches by Pagilla, Tarn, and others may not be suitable for robotic deburring and grinding.

Objectives of This Study

From our literature review, most proposed control algorithms for manipulators operating in constrained and unconstrained environments employ some type of force control for stable contact while tracking a desired trajectory. In the work herein, we seek high accuracy in the finished workpiece profile using robotic finishing. That is, we are interested in employing force control only when the normal or tangential forces exerted by the workpiece on the end effector exceed some pre-specified limits, at which point we are prepared to compromise on position accuracy, otherwise, we desire highly accurate position control. We assume that the actual geometry of the workpiece is unknown and we wish to finish workpieces of different materials. Employing a force-tracking strategy under these assumptions will be very difficult. On the other hand, impulsive forces may need to be regulated when the end effector contacts the workpiece or encounters a large burr. Such demands increase the difficulty in implementing robotic deburring and grinding.

This research investigates position control and force regulation of a simple two-arm SCARA robot carrying a powered tool at its end effector used for deburring and grinding. Based on Hong's work [3], we extend the grinding models to encompass easy to grind (ETG) materials and difficult to grind(DTG) materials. A new switched control method is developed for this operation, and other control algorithms are investigated to compare performance for robotic deburring and grinding. The remainder of this thesis will describe system modeling, the new control approach for robotic deburring and grinding, and computer simulation results. Chapter II describes the dynamics of the robot and the force model for ETG/DTG materials. In Chapter III, a new switched controller is presented for position control and force regulation in robotic deburring and grinding. We also investigate impedance control and hybrid impedance control in this application. Chapter IV discusses surface characteristics for various surface irregularities and burrs. Simulation results for various controllers are presented, together with analysis and discussion. Chapter V follows with conclusions and recommendations.

CHAPTER II

SYSTEM MODELING

In this chapter, we first address the equations describing the dynamics of a manipulator having n links. We have elected to use as our simulation test bed, a model of a SCARA robot developed at UC-Berkeley [19] using NSK drives. The grinding forces for our study are derived from conventional grinding models. The stiffness of the robotic arm will also be discussed. Control strategies and simulations are based on the models developed here.

Manipulator Dynamics

A robotic manipulator can be considered as a set of n rigid bodies connected in a serial chain with friction acting at the joints. The equation describing the dynamics of such a device in free space can be expressed in "joint space" as [10]:

$$M(q)\ddot{q} + C(q,\dot{q})\dot{q} + F_f(q,\dot{q}) + G(q) = \tau \tag{2.1}$$

where q is an $n \times 1$ joint variable vector, $\dot{q}$ is the time derivative of q, $M(q)$ is an $n \times n$ inertia matrix, $C(q,\dot{q})$ represents an $n \times n$ matrix that describes the centrifugal and Coriolis terms in the dynamics of the manipulator, $G(q)$ is an $n \times 1$ vector containing terms arising from forces due to gravity, $F_f(q)$ is an $n \times 1$ vector that specifies the effects of Coulomb friction force in the joints, and τ is an $n \times 1$ vector that defines input torques from the actuators of the manipulator.

Since the natural description of a desired trajectory and interaction force are given in "task space", it is desired to express the dynamics of a manipulator in task space as [3, 16]:

$$M_t(q)\ddot{X} + C_t(q,\dot{q})\dot{X} + F_{ft}(q,\dot{q}) + G_t(q) = F \tag{2.2}$$

where F is a $n \times 1$ force vector arising from actuator torque at the end effector, $M_t(q)$ and $C_t(q)$ are $n \times n$ matrices corresponding to the inertial matrix and centrifugal/Coriolis matrix in task space, and $G_t(q)$ and $F_{ft}(q, \dot{q})$ are $n \times 1$ vectors of gravity and friction force terms in task space. For simplicity, we consider the task space to be the Cartesian (reference) space in this study.

Note that the force term, F, arising from actuator torques at the end effector is applied by the actuators at the joints, using the relationship

$$\tau = J^T(q)F \tag{2.3}$$

where $J(q)$ is the $n \times n$ manipulator Jacobian matrix written in the same frame as F and $\ddot{X}$. The Jacobian matrix is defined by [3]

$$J(q) = \frac{\partial L(q)}{\partial q} \tag{2.4}$$

where $L(q)$ is a continuous function of the joint space vector found from manipulator kinematics and geometric relationships. It relates the $n \times 1$ task space vector X to generalized joint coordinates q by

$$X = L(q) \tag{2.5}$$

When the end effector contacts an object, such as a workpiece, a force term arises on the right of (2.1) due to the environment, such that (2.1) becomes

$$M(q)\ddot{q} + C(q,\dot{q})\dot{q} + F_f(q,\dot{q}) + G(q) = \tau - J^T F_e \tag{2.6}$$

where F_e is the $n \times 1$ vector that defines the task space force or torque acting on the end effector of the manipulator. Similarly, for such contact, (2.2) becomes

$$M_t(q)\ddot{X} + C_t(q,\dot{q})\dot{X} + F_{ft}(q,\dot{q}) + G_t(q) = F - F_e \tag{2.7}$$

We can derive the relationship between the terms of (2.6) and those of (2.7). First, premultiply (2.6) by the inverse of the Jacobian to obtain

$$J^{-T} M(q)\ddot{q} + J^{-T} C(q,\dot{q})\dot{q} + J^{-T} F_f(q,\dot{q}) + J^{-T} G(q) = J^{-T}\tau - J^{-T} J^T F_e \tag{2.8}$$

or from (2.3),

$$J^{-T} M(q)\ddot{q} + J^{-T} C(q,\dot{q})\dot{q} + J^{-T} F_f(q,\dot{q}) + J^{-T} G(q) = F - F_e \tag{2.9}$$

Now differentiate (2.5) twice with respect to time to obtain

$$\dot{X} = J(q)\dot{q} \tag{2.10}$$

$$\ddot{X} = J(q)\ddot{q} + \dot{J}(q)\dot{q} \tag{2.11}$$

Eq. (2.10) is assumed to be nonsingular. Solving for $\dot{q}$ and $\ddot{q}$ gives

$$\dot{q} = J^{-1}(q)\dot{X} \tag{2.12}$$

$$\ddot{q} = J^{-1}(q)(\ddot{X} - \dot{J}(q)\dot{q}) \tag{2.13}$$

Substituting from (2.12) and (2.13) into (2.9) yields

$$J^{-T}M(q)J^{-1}\ddot{X} - J^{-T}M(q)J^{-1}\dot{J}J^{-1}\dot{X} + J^{-T}C(q,\dot{q})J^{-1}\dot{X} + J^{-T}F_f(q,\dot{q}) + J^{-T}G(q) = F - F_e \tag{2.14}$$

from which we derive the expressions for the terms in the task space dynamics in (2.7) as

$$\begin{aligned} M_t &= J^{-T}(q)M(q)J^{-1}(q) \\ C_t &= J^{-T}(q)[C(q,\dot{q})J^{-1} - M(q)J^{-1}\dot{J}(q)J^{-1}(q)] \\ F_{ft} &= J^{-T}(q)F_f(q,\dot{q}) \\ G_t &= J^{-T}(q)G(q) \end{aligned} \tag{2.15}$$

In practical applications, the control input, torques τ, are commanded in joint space, and encoders and tachometers are usually placed on the motor shafts, such that positions and velocities are measured in joint space. To obtain motion of the end effector in task space, "forward kinematics" is employed for transformation. Accordingly, we can derive a more convenient and useful expression for the manipulator dynamics by substituting from (2.13) into (2.6), which yields

$$M(q)J^{-1}(q)(\ddot{X} - \dot{J}(q)\dot{q}) + C(q,\dot{q})\dot{q} + F_f(q,\dot{q}) + G(q) = \tau - J^T F_e \tag{2.16}$$

These new manipulator dynamics will be used to design the control laws for deburring and grinding in Chapter III.

UC-Berkeley/NSK SCARA Robot

Detailed information on typical robot installations for deburring and grinding can not be readily obtained because of a certain degree of proprietary information surrounding many of these installations. This is because robot manufacturers desire to withhold information about their robots from their actual and potential competitors. Thus, detailed modeling information is typically not reported in trade publications, nor is such information provided by robot manufacturers to customers. In this study, we employ a UC-Berkeley/NSK SCARA robot, which consists of only four major mechanical parts, two direct drive motors from Nippon Seiko K.K. (NSK) and two aluminum links, as a benchmark for our simulations because the technical data for this robot have been published [19], and its configuration as a two axis robotic arm provides a planar workspace, appropriate for our study.

In this work, we are concerned with end effector motion and force acting only in a horizontal plane, parallel to the planes of motion of the SCARA planar robot. We employ a model with only two degrees of freedom, namely rotations of the two main arms of the SCARA robot about their vertical axes, as shown in Figure 2.1. Because gravity has no effect in the horizontal plane, the gravity term in (2.6) vanishes, and the dynamic equation in joint space for this simple model reduces to a second-order nonlinear differential equation given by [19]

$$M(q)\ddot{q} + C(q,\dot{q})\dot{q} + F_f(q,\dot{q}) = \tau - J^T F_e \tag{2.17}$$

where q, τ and F are 2×1 vectors as defined previously, and

$$M = \begin{bmatrix} m_{11} & m_{12} \\ m_{21} & m_{22} \end{bmatrix} \quad , \quad C = \begin{bmatrix} c_{11} & c_{12} \\ c_{21} & c_{22} \end{bmatrix} \tag{2.17a}$$

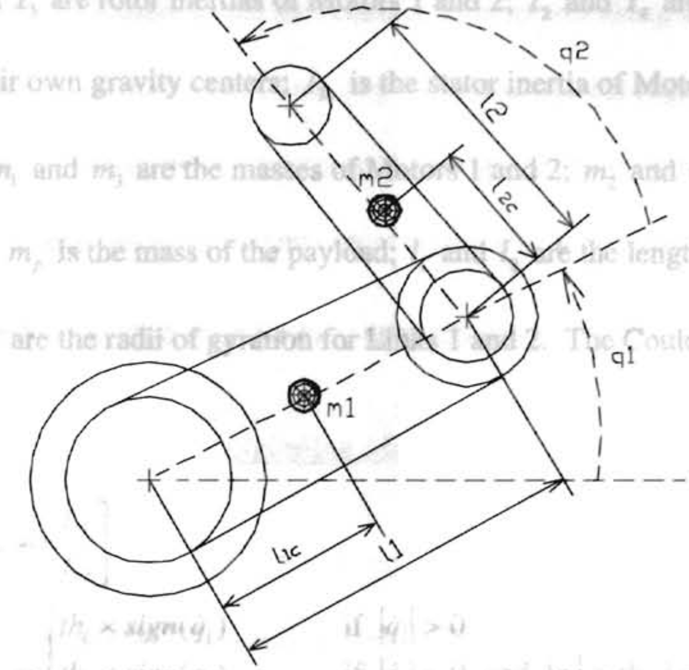

Figure 2.1 Schematic Diagram of Two-Arm SCARA Robot

with

$$\begin{aligned} m_{11} &= p_1 + 2p_2\cos(q_2) \\ m_{12} &= m_{21} = p_3 + p_2\cos(q_2) \\ m_{22} &= p_3 \\ c_{11} &= -2p_2\sin(q_2)\dot{q}_2 \\ c_{12} &= -p_2\sin(q_2)\dot{q}_2 \\ c_{21} &= p_2\sin(q_2)\dot{q}_1 \\ c_{22} &= 0 \end{aligned} \tag{2.17b}$$

where p1, p2, and p3 are constant terms dependent on the manipulator's geometric dimensions and masses of components, given by [19]

$$
\begin{aligned}
p_2 &= l_1 l_{2c} m_1 + l_1 l_2 m_p \\
p_3 &= I_3 + I_4 + I_p + (l_{2c}^2 m_4 + l_2^2 m_p) \qquad (2.17c) \\
p_1 &= I_1 + I_2 + I_{3c} + l_{1c}^2 m_2 + l_1^2 (m_3 + m_4 + m_p) + p_3
\end{aligned}
$$

In (2.17c) I_1 and I_3 are rotor inertias of Motors 1 and 2; I_2 and I_4 are inertias of Links 1 and 2 about their own gravity centers; I_{3c} is the stator inertia of Motor 2; I_p is the payload inertia; m_1 and m_3 are the masses of Motors 1 and 2; m_2 and m_4 are the masses of Links 1 and 2; m_p is the mass of the payload; l_1 and l_2 are the lengths of Links 1 and 2; and l_{1c} and l_{2c} are the radii of gyration for Links 1 and 2. The Coulomb friction matrix is described by:

$$
F_f = \begin{bmatrix} f_{s1} \\ f_{s2} \end{bmatrix}
$$

$$
f_{si} = \begin{cases} th_i \times sign(\dot{q}_i) & \text{if } |\dot{q}_i| > 0 \\ th_i \times sign(q_i) & \text{if } |\dot{q}_i| = 0 \text{ and } |q_i| > th_i \quad \mathrm{i} = 1{,}2 \\ q_i & \text{if } |\dot{q}_i| = 0 \text{ and } |q_i| \le th_i \end{cases}
$$

where th_i is the magnitude (unitless) of the friction torque and $i = 1{,}2$. Note that this number th_i is also used as the switch limit for $|q_i|$.

Similarly, the dynamic equation in task space for this simple model can reduce to a second-order nonlinear differential equation from (2.7) as

$$
M_t(q)\ddot{X} + C_t(q,\dot{q})\dot{X} + F_{ft}(q,\dot{q}) = F - F_e \qquad (2.18)
$$

with coefficient matrices defined by (2.15) and the appropriate matrices and vectors defined as for (2.17). For simplicity to implement dynamic analysis and control based on (2.18), we define the x-y horizontal reference system plane as identical with the task space t-n, defined by two orthogonal axes normal and tangential to the surface at an idealized point of contact of the grinding tool. Thus, we assume a straight-line nominal surface edge aligned with the x axis. Considering the implications of following a curved edge, the task coordinate system changes as the tool contact point moves along an arbitrary curved edge in the reference system. At each time step in simulation, this requires two steps of transformation namely, from robot joint space to task space and from task space to reference space. A very fast and efficient computation will be an important issue in the design of a manipulator system used for such applications.

Grinding Modeling

In this section we model the grinding forces based on conventional grinding operations. The grinding conditions will be specified for calculating the grinding forces. Force limits to prevent damage to the workpiece and breakdown forces for a selected grinding wheel will also be discussed. Finally, we investigate the effects of different workpiece materials.

Force Modeling

In steady grinding operations, the grinding forces can usually be treated as two orthogonal forces: F_n normal to the contact surface and F_t tangential to the contact surface, as shown in Figure 2.2. Hahn and Lindsay [20] have experimentally investigated the grinding process and developed an empirical equation for the normal grinding force as

$$F_n = \frac{Z_w}{\Lambda_m} \tag{2.19}$$

where

F_n = normal grinding force

Z_w = material removal rate

Λ_m = metal removal parameter

By definition [3],

$$Z_w = V_w db \tag{2.20}$$

where V_w is the workpiece feed rate, d is the depth of cut, and b is the width of cut. Hahn and Lindsay have also proposed an empirical equation to predict Λ_m based on experimental data, which yields errors of +/- 20 % for easy-to-grind (ETG) materials [20].

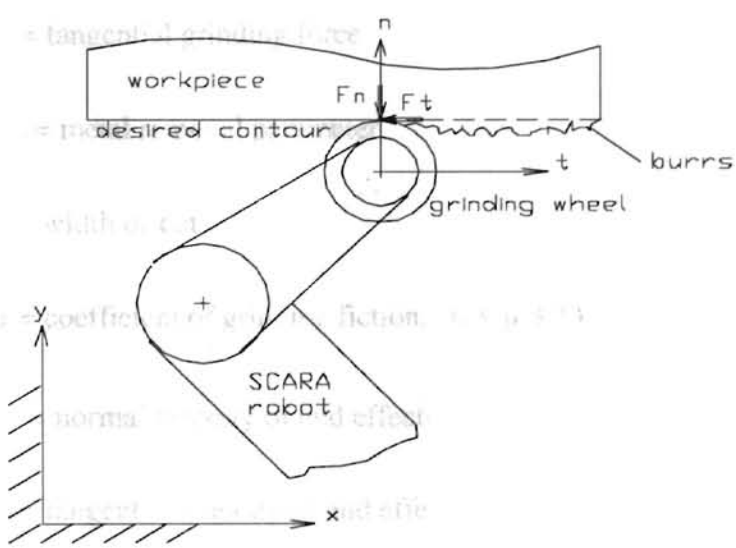

Figure 2.2 Robotic Grinding Schematic [3]

Robotic deburring and grinding differs from conventional grinding because of the compliant structure and mobility of the robot. Material feeding is accomplished by moving the robot relative to the workpiece rather than feed-in of the workpiece to a stationary grinding wheel as in conventional grinding. Hong [3] developed normal and tangential grinding force equations for robotic deburring and grinding by employing Hahn and Lindsay's experimental equations for conventional grinding forces, together with geometry and kinematics. His results yielded

$$\begin{aligned} F_n &= [v_t + (0.285D / d + 1)v_n]db / \Lambda_m \\ F_t &= \mu F_n \end{aligned} \tag{2.21}$$

where

D = the wheel diameter

d = depth of cut

F_n = normal grinding force

F_t = tangential grinding force

Λ_m = metal removal parameter

b = width of cut

μ = coefficient of grinding fiction, ($0 \le \mu \le 1$)

v_n = normal velocity of end effector

v_t = tangential velocity of end effector

In our simulation work in Chapter IV, we will employ (2.21) to calculate grinding forces. In actual implementation, normal and tangential grinding forces would be measured directly by a force sensor at the end effector.

ETG and DTG Materials

The grinding wheel speed, workpiece hardness, dressing lead, and depth of dress are the four most important parameters affecting the metal removal parameter, Λ_m, [20]. The workpiece hardness can usually be classified into two categories: easy-to-grind (ETG) and difficult-to-grind (DTG) materials [20]. Materials classified as ETG are chrome, cast iron, aluminum, and soft steel. DTG materials are many steels in the M and T categories of tool steels, titanium alloys, and high-nickel steels. In this section, we calculate the metal removal parameter, Λ_m, for an ETG and a DTG material.

For ETG materials, Λ_m, the metal removal parameter can be predicted within 20 % by a semi-empirical equation given by [20]

$$\Lambda_m = (0.021\ \frac{in.^{515/304}}{lb}) \frac{(\frac{V_w}{V_s})^{3/19}\ (1+\frac{2\,C}{3\,l})\ l^{11/19}\ V_s}{D_e^{\ 43/304}\ (vol)^{0.47}\ d^{5/38}\ R_c^{\ 27/19}} \tag{2.22}$$

where

Λ_m = in^3/(min, lb) $\qquad$ V_w = workspeed, fpm

V_s = wheel speed, fpm $\qquad$ l = inch per wheel revolution

D_e = conformity, or the equivalent diameter, inch

d = grain size in wheel, inch

vol = approx. volume percent of bonding material in the wheel

C = diametric depth of dress, inch

R_c = value of Rockwell Hardness

In (2.22), $\frac{in.^{515/304}}{lb}$ is used to cancel the power of units for Λ_m. The parameter vol can be estimated from the empirical relationship given by

$$vol = 1.33\ H_d + 2.2\ S - 8.0 \tag{2.23}$$

where

H_d = wheel hardness, denoted by H, I, J, K, L, M, etc. with H = 0, I = 1, J = 2, K = 3, etc.

S = wheel structure number, 4, 5, 6, etc.

D_e, conformity, or equivalent diameter, is the degree to which the wheel surface fits or conforms to the workpiece surface. For surface grinding, $D_e = D_s$, grinding wheel diameter. For the workspeed, V_w, we will use the relative speed of workpiece to the end effector, which is chosen as 0.012 m/s for our simulation later. As an example, we calculate the metal removal parameter, Λ_m, for an ETG material as follows [20, 21].

Material:	R_c 60, AISI 52100 steel, width 10 mm.	
Grinding wheel:	D_s = 2 inch,	V_s = 18000 fpm
	type: 80K5V,	grain size (d): 0.01 inch

dress lead (l): 0.004 ipr

dressing compensation (C): 0.001 inch

V_w = 2.362 fpm (0.012 m/s)

$$\Lambda_m = (0.021)\frac{(\frac{2.362}{18000})^{3/19}(1+\frac{2\cdot 0.001}{3\cdot 0.004})\cdot(.004)^{11/19}\cdot 18000}{2^{43/304}\cdot(1.33\cdot 3+2.2\cdot 5-8)^{0.47}\cdot 0.01^{5/38}\cdot 60^{27/19}}$$

$$= 0.00871 \text{ in}^3/(\text{min, lb}) = 5.3484\times 10^{-10} \text{ m}^3/(\text{sec, N})$$

For DTG materials, we have been unable to locate a suitable equation to calculate Λ_m. Thus we use values from experimental data and assume that grinding conditions, wheel dressing, and rotary speed are the same as described for experiments in [20]. For an R_c 64, M4 material, the value for Λ_m ranged from 0.000035 to 0.0028 in^3/(min, lb) [20]. As a reasonable example, we choose Λ_m = 0.002 in^3/(min, lb) (1.228×10^{-10} m^3/(sec-N)) to simulate the grinding force for a DTG material.

Eq. (2.21) and the value for Λ_m developed here for an ETG and a DTG material will be used for computer simulations in Chapter IV.

Grinding Force Limits

In considering possible limits to applied grinding forces, we consider potential thermal damage to the workpiece and breakdown forces of the grinding wheel. Thermal damage to a workpiece may be caused by excessive grinding temperature and can be classified into three common types: workpiece burn, workpiece tempering, and induced residual stresses in the workpiece [22]. Workpiece burn and tempering have apparently not been studied extensively in grinding operations, perhaps because induced residual stresses are more commonly encountered. Accordingly, we focus on induced residual stress as the major concern for thermal damage in this work.

The grinding process invariably produces residual stresses in the vicinity of the finished surface. When residual tensile stresses exist, a workpiece surface is thermally damaged because such stresses lead to reduced fatigue strength and cracking. Although residual compressive stresses can also be generated, their magnitudes are much smaller than residual tensile stresses. Usually, residual compressive stresses are induced after grinding by cold working operations. There are three principal means to reduce thermal damage: decrease contact time by increase grinding speed, decrease force intensity and wheelspeed, and maintain wheel sharpness.

The normal grinding force to cause thermal cracking for an ETG material with $\Lambda_m = 0.0064$ in^3/(min, lb) and work surface speed = 1200 fpm is about 320 lb/in (56.04 N/mm) [20]. The normal grinding force to cause thermal cracking for our ETG materials will be larger than 320 lb/in because our value for Λ_m is greater than 0.0064 in^3/(min, lb). However, the normal grinding force to cause thermal cracking for our DTG material is unavailable from the literature. Our workpiece width is 10 mm, such that the normal grinding force to cause thermal cracking is at least 560.4 N for our ETG material. Following [21], we select a grinding wheel designated 80K5V for our ETG and DTG materials, for which the breakdown force is 483 N (48.3 N/mm $\times$ 10 mm). Since this wheel breakdown force is lower than our workpiece thermal damage limiting force, we will use the breakdown force as a force limit in our simulation in Chapter IV.

Motor and Robot Arm Stiffness

The stiffness of the UC-Berkeley NSK SCARA robot is not given in the available literature. In this section, we estimate the stiffness of the NSK motors and our robot links for worst-case conditions, which will allow us to determine if our robot is sufficiently rigid to justify ignoring robot arm flexibility. The robot links are made from aluminum, and the specifications are given in Table 1 [19].

Table 1 Robot Links Specifications

	Inertia	Length
Link 1	0.360 kg m^2	0.36 m
Link 2	0.051 kg m^2	0.24 m

The two robot joint motors used are made by NSK, Model 1410 for the first (lower) axis and Model 608 for the second (upper) axis. The moment rigidities of these two motors are: Motor 1 (first axis), $M_{k1} = 3.27 \times 10^6$ N - m / rad, and Motor 2 (second axis), $M_{k2} = 2.80 \times 10^5$ N - m / rad [23]. Motor specifications from [23] are given in Appendix A. The most compliant configuration for the motors and robot arms is that for which both links lie along a straight line in the fully extended position, illustrated in

Figure 2.3(a).

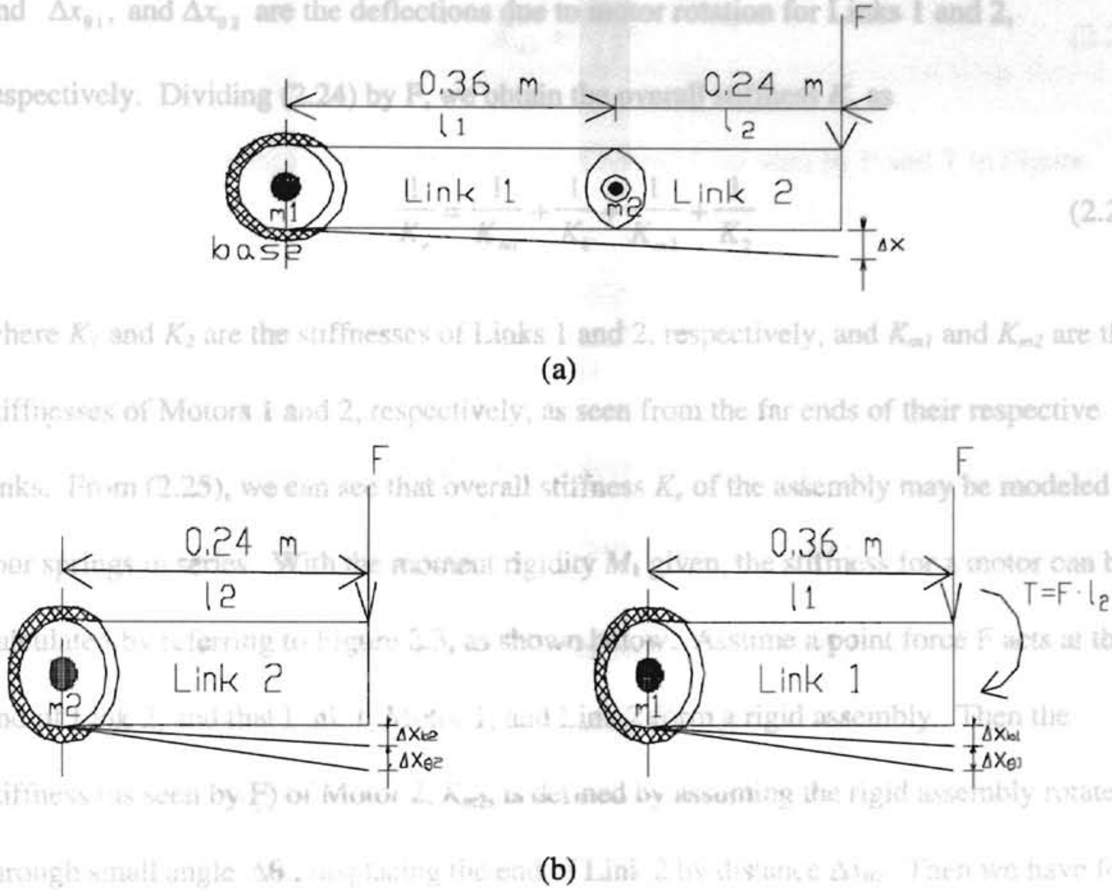

Figure 2.3 Motor and Arm Configuration for Stiffness Calculation

We assume there is no reduction gear, such that the robot arm joints are directly coupled to the rotors of the motors. By considering Figure 2.3(b), it can be seen that including the deflections of Motor 1, Link 1, Motor 2, and Link 2, the total deflection ΔX is

$$\Delta x = \Delta x_{b2} + \Delta x_{\theta 2} + \Delta x_{b1} + \Delta x_{\theta 1} \tag{2.24}$$

where Δx_{b1} and Δx_{b2} are the deflections due to bending of Links 1 and 2, respectively, and $\Delta x_{\theta 1}$, and $\Delta x_{\theta 2}$ are the deflections due to motor rotation for Links 1 and 2, respectively. Dividing (2.24) by F, we obtain the overall stiffness K_e as

$$\frac{1}{K_e} = \frac{1}{K_{m1}} + \frac{1}{K_1} + \frac{1}{K_{m2}} + \frac{1}{K_2} \tag{2.25}$$

where K_1 and K_2 are the stiffnesses of Links 1 and 2, respectively, and K_{m1} and K_{m2} are the stiffnesses of Motors 1 and 2, respectively, as seen from the far ends of their respective links. From (2.25), we can see that overall stiffness K_e of the assembly may be modeled as four springs in series. With the moment rigidity M_k given, the stiffness for a motor can be calculated by referring to Figure 2.3, as shown below. Assume a point force F acts at the end of Link 2, and that Link 1, Motor 1, and Link 2 form a rigid assembly. Then the stiffness (as seen by F) of Motor 2, K_{m2}, is defined by assuming the rigid assembly rotates through small angle $\Delta\theta$, displacing the end of Link 2 by distance $\Delta x_{\theta 2}$. Then we have for K_{m2},

$$K_{m2} = \frac{F}{\Delta x_{\theta 2}} \tag{2.26}$$

Now assuming the small angle approximation

$$\Delta x_{\theta 2} \approx l_2 \cdot \Delta\theta \tag{2.27}$$

together with the definition of motor rigidity [23] for Motor 2, we obtain

$$M_{k2} = \frac{F \cdot l_2}{\Delta\theta} \tag{2.28}$$

Employing (2.28) and (2.27) in (2.26) yields

$$K_{m2} = \frac{M_{k2}}{l_2^{\,2}} \tag{2.29}$$

Using a similar development for the stiffness of Motor 1 (as seen by F and T in Figure 2.3b), we obtain

$$K_{m1} = \frac{M_{k1}}{(l_1 + l_2)l_1} \tag{2.30}$$

Using the rigidity values above for the two motors and the lengths of the two robot arms given in Table 1, we obtain $K_{m1} = 1.51 \times 10^7$ N / m and $K_{m2} = 4.86 \times 10^6$ N / m.

To determine K_1 and K_2, we assume that each link is a cantilever beam fixed at its left end with a point load applied at the free end on the right of Link 1, and a point load and moment load applied at the free end on the right of Link 2. We consider two cases of area section for each link: a circular ring and a square tubular section. The end deflection of a cantilever beam with a point load at the free end is given by [24]

$$\Delta x_b = \frac{FL^3}{3EI} \tag{2.31}$$

where Δx_b is the free end deflection, F is end load, L is length, E is modulus of elasticity, and I is moment of inertia. The stiffness K can then be defined as

$$K = \frac{F}{\Delta x_b} = \frac{3EI}{L^3} \tag{2.32}$$

Therefore K_2 is given by

$$K_2 = \frac{3EI_2}{l_2^3} \tag{2.33}$$

For Link 1, there is a moment, T, applied at the free end, in addition to the point load F. The deflection Δx_m caused by this moment is given by [25]

$$\Delta x_m = \frac{T \cdot l_1^2}{2EI_1} \tag{2.34}$$

where $T = F \times l_2$. Then, the stiffness of Link 1 is

$$K_1 = \frac{F}{\Delta x_m + \Delta x_b} = \frac{6EI_1}{2l_1^3 + 3l_2 l_1^2} \tag{2.35}$$

The mass density, ρ, of aluminum is 2800 kg/m^3 and the link inertia, I, is 0.36 kg m^2 for Link 1 and 0.051 kg m^2 for Link 2. The equation for arm inertia is given by

$$I_a = mr^2 \tag{2.36}$$

where m is the link mass and r is the link radius of gyration, which from Figure 2.3 is 0.18 m for Link 1 and 0.12 m for Link 2. The mass can be calculated by

$$m = \rho AL \tag{2.37}$$

where A is the link section area and L is the link length. From (2.32), (2.33), and given parameters, we obtain $A_1 = 0.011$ m^2 and $A_2 = 5.27 \times 10^{-3}$ m^2 for Link 1 and Link 2, respectively. With these values for A_i, the stiffness for different cross sections of each link can be calculated as shown below.

Case I: Circular Ring Cross Section

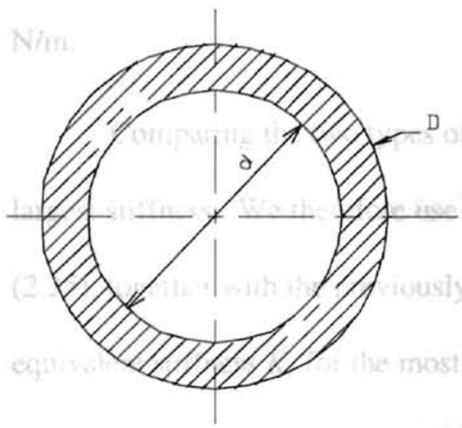

Assume $d_i = 0.8D_i$

$$A_i = \frac{\pi(D_i^2 - d_i^2)}{4}$$

$D_1 = 0.1972$ m, $d_1 = 0.1578$ m

$D_2 = 0.1365$ m, $d_2 = 0.1092$ m

The modulus of elasticity, E, for aluminum is 70×10^9 N/m^2 and the moment of inertia, I, for a circular ring is defined as [24]

$$I_i = 0.049087(D_i^4 - d_i^4) \tag{2.38}$$

Then (2.38) and (2.35), (2.33) yield $K_1 = 9.8564 \times 10^7$ N/m, $K_2 = 1.5284 \times 10^8$ N/m.

Case II: Square Tubular Section

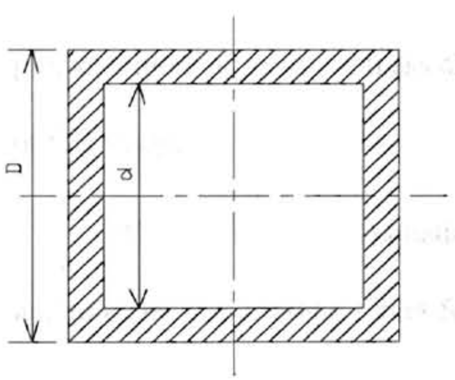

Assume $d_i = 0.8D_i$

$A_i = D_i^2 - d_i^2 = 0.36\ D_i^2$

$D_1 = 0.1748$ m, $d_1 = 0.1398$ m

$D_2 = 0.1210$ m, $d_2 = 0.0968$ m

The moment of inertia, I, for a square tubular section is [24]

$$I_i = \frac{(D_i^4 - d_i^4)}{12} \tag{2.39}$$

Combining (2.39) and (2.35), (2.33) yields $K_1 = 1.0346 \times 10^8$ N/m, $K_2 = 1.6021 \times 10^8$ N/m.

Comparing the two types of beams, we see that the square tubular section has the largest stiffness. We therefore use the values for K_1 and K_2 for a square tubular section in (2.25), together with the previously determined values for K_{m1} and K_{m2}, to obtain the equivalent stiffness K_e for the most compliant robot arm orientation as

$$K_e = 3.4735 \times 10^6 \text{ N/m} = 19836.58 \text{ lb/in}$$

For a maximum normal force of 450 N, which we will employ in Chapter IV, this corresponds to a "worse-case" end deflection of 0.1296 mm. For a more reasonable robot configuration than worst case, we assume that 1/2 of this value is more representative, namely 0.0648 mm. As we shall see, such deflection is small compared to most position errors in our simulations. We conclude that this value of K_e is sufficiently large to ignore robot flexibility. However, this prediction may not truly represent overall robot compliance because the drive train may introduce more flexibility than the links. To predict a more accurate stiffness of more realistic structural elements is beyond the scope of this study.

We have developed equations describing the dynamics of a two-link SCARA robot and modeled the grinding forces for robotic deburring and grinding. In the next chapter, we will employ these models to investigate and design control methods for these operations.

CHAPTER III

CONTROL APPROACHES

In this chapter, several control approaches are investigated. A well known feedback linealization method is used to linealize manipulator dynamics. Based on feedback linealization, several control laws are developed for robotic deburring and grinding. A new switched control method is proposed for this operation to improve position accuracy and force regulation.

Feedback Linealization

Feedback linealization is an approach used to control nonlinear systems, which has attracted considerable study recently. The basic idea of feedback linealization is to transform a nonlinear dynamic system into a linear one, in order that linear control theory can be applied to the transformed dynamic system. It is achieved by "exact state transformations and feedback, rather than by linear approximations of the dynamics" [27]. The nonlinear control used to produce the transformation is constructed by feedback linealization and is called inner loop control [10]. The designer can then design an outer loop control using classical linear control approaches by specifying performance such as tracking, disturbance rejection, and robustness.

The dynamic equations of a two degree of freedom SCARA robot are nonlinear and coupled. Feedback linealization is employed to linealize the manipulator dynamics by inner loop control before considering the design of position and force controllers by outer loop control. Computed-torque control [16] is a special application of feedback linearization for manipulator dynamic nonlinearities, which has been widely applied in robot control. This approach amounts to canceling the nonlinearities of a nonlinear system so that the closed-loop dynamics become linear. In this project, we employ this method to construct an inner loop control structure before designing the outer loop controllers. The manipulator dynamic equation given by (2.16) is repeated here as

$$M(q)J^{-1}(q)(\ddot{X} - \dot{J}(q)\dot{q}) + C(q,\dot{q})\dot{q} + F_f(q,\dot{q}) + G(q) = \tau - J^T F_e \tag{3.1}$$

The problem of controlling a complicated system such as described by (3.1) can be handled by a partitioned controller [16], with torque τ given by

$$\tau = \alpha\tau' + \beta \tag{3.2}$$

where τ is the $n \times 1$ vector of joint torques, τ' is the "servo" portion of the control law and is based on outer loop considerations, and α and β are functions chosen to decouple and cancel the nonlinear terms in the complete dynamic system. The control law given by (3.2) is the model-based portion of the controller [16], which establishes an inner control loop as shown in Figure 3.1. Following Craig [16], we choose

$$\begin{aligned} \alpha &= M(q)J^{-1}(q) \\ \beta &= -M(q)J^{-1}(q)\dot{J}(q)\dot{q} + C(q,\dot{q})\dot{q} + F_f(q,\dot{q}) + G(q) + J^T F_e \end{aligned} \tag{3.3}$$

In Figure 3.1, the inner loop feedback term $N(q,\dot{q})$ is given by

$$N(q,\dot{q}) = -M(q)J^{-1}(q)\dot{J}(q)\dot{q} + C(q,\dot{q})\dot{q} + F_f(q,\dot{q}) + G(q) \tag{3.3a}$$

Substituting (3.3) into (3.2), the model-based portion of the control law becomes

$$\tau = M(q)J^{-1}(q)\tau' - M(q)J^{-1}(q)\dot{J}(q)\dot{q} + C(q,\dot{q})\dot{q} + F_f(q,\dot{q}) + G(q) + J^T F_e \tag{3.4}$$

Now employing the right of (3.4) for τ in (3.1) yields

$$\ddot{X} = \tau' \tag{3.5}$$

Eq. (3.5) shows that the acceleration of the end effector is equal to the servo portion of the control law, which can be designed to achieve design specifications, such as minimum tracking error and (desired) disturbance rejection. If we design the servo controller for τ' properly, the desired motion of the manipulator can be achieved from the computed torque control law (3.4), assuming available motor torque does not saturate.

In order to employ (3.4), it must be assumed that the manipulator dynamics are known exactly with perfect sensors for the measurement of forces, positions, and velocities. However, in practice there exist modeling and measurement errors, which may cause inexact cancellation of dynamics of the nonlinearities in (3.4). It is possible that a lack of robustness could arise from inexact cancellation of dynamics of the nonlinearities, but treatment of this problem is beyond the scope of this research. We are concerned here mainly with outer loop design in the absence of inner loop uncertainty. In the following sections, we design and analyze some outer loop controllers, based on the control structure developed above.

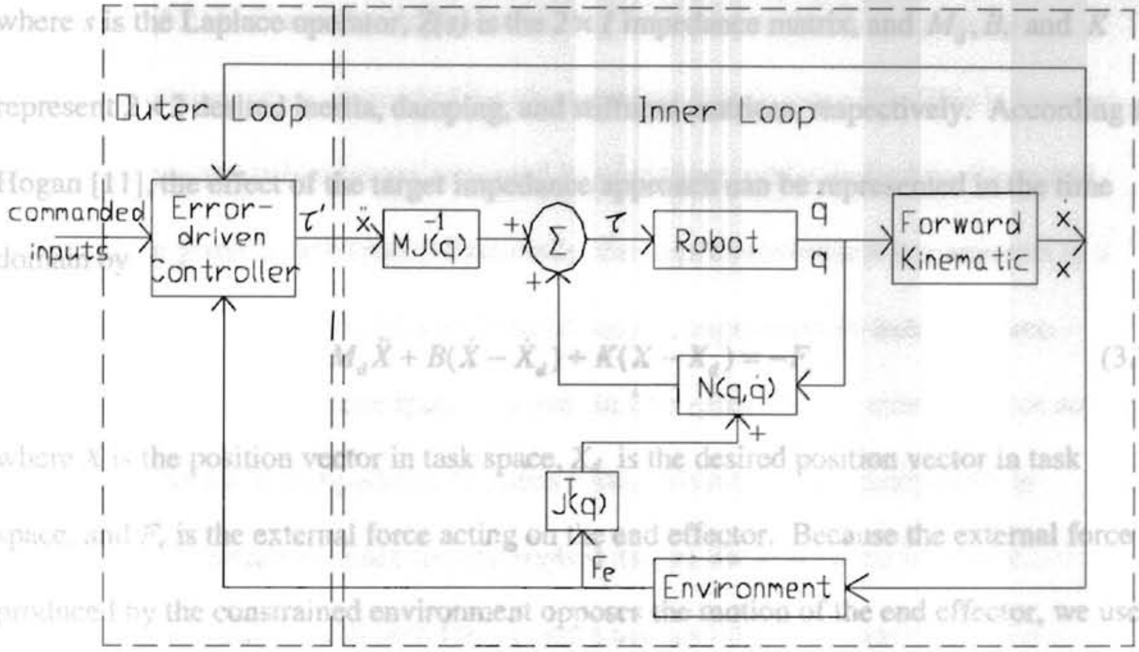

Figure 3.1 Diagram of Control Structure [3]

Impedance Control

Impedance control regulates the relation of position to force and changes the dynamic behavior of the system. It may be suitable for robotic deburring and grinding to track a desired trajectory while accommodating the cutting forces produced by the cutting process. To implement impedance control, the first step is to specify the desired behavior of the target impedance. Hogan [9] points out that the target impedance consists of some inertial, damping, and stiffness characteristics that describe the relation between the position of the end effector and the force exerted by the environment. Typically , this impedance can be expressed as

$$Z(s) = M_d s^2 + Bs + K \tag{3.6}$$

where s is the Laplace operator, $Z(s)$ is the 2×1 impedance matrix, and $M_d, B,$ and K represent 2×2 desired inertia, damping, and stiffness matrices, respectively. According to Hogan [11], the effect of the target impedance approach can be represented in the time domain by

$$M_d \ddot{X} + B(\dot{X} - \dot{X}_d) + K(X - X_d) = -F_e \tag{3.7}$$

where X is the position vector in task space, X_d is the desired position vector in task space, and F_e is the external force acting on the end effector. Because the external force produced by the constrained environment opposes the motion of the end effector, we use a minus sign for F_e in (3.7). Solving for $\ddot{X}$ gives

$$\ddot{X} = -\frac{1}{M_d}[F_e + B(\dot{X} - \dot{X}_d) + K(X - X_d)] \tag{3.8}$$

Substituting the right side of (3.8) for $\ddot{X}$ in (3.1) yields the control law torque as

$$\tau = G_1 F_e + G_2 B \Delta\dot{X} + G_2 K \Delta X - G_3 \dot{J}(q)\dot{q} + G_4 \tag{3.9}$$

where we have defined errors $\Delta\dot{X}$ and ΔX by

$$\Delta\dot{X} = \dot{X}_d - \dot{X}$$
$$\Delta X = X_d - X$$

and nonlinear "gains" G_1, G_2, G_3, and G_4 by

$$G_1 = J^T(q) - G_2$$
$$G_2 = M(q) J^{-1} M_d^{-1}$$
$$G_3 = G_2 M_d$$
$$G_4 = C(q,\dot{q})\dot{q} + F_f(q,\dot{q}) + G(q)$$

Eq. (3.9) has been developed containing both joint and task space terms to facilitate implementation, instead of developed solely in task space [3]. This is because robot positions and velocities are measured in joint space, while desired positions and velocities are given in task space. Essentially, the impedance control law amounts to a proportional plus derivative (PD) position controller, augmented by external force feedback. Note that if the manipulator moves in free space with no external force acting on the end effector, the impedance becomes zero. Conversely if a manipulator is motionless in constrained space for any applied torque, the impedance is infinite. Therefore, pure position and pure force control are considered as special cases of impedance control.

Hong [3] and McCormick and Schwartz [12] discuss an alternate impedance control strategy described by

$$M_d\ddot{X} + B(\dot{X} - \dot{X}_d) + K(X - X_d) = F_d - F_e \tag{3.10}$$

where F_d is a desired force vector (required for material removal during grinding in our case). Solving for $\ddot{X}$ and substituting in (3.1) yields a control law torque given by

$$\tau = G_1F_e + G_2F_d + G_2B\Delta\dot{X} + G_2K\Delta X - G_3\dot{J}(q)\dot{q} + G_4 \tag{3.11}$$

This alternate impedance control strategy commands desired forces along with desired positions and velocities for robotic deburring and grinding operations. If the needed grinding force F_d is modeled well and surface geometry is known, desired forces may be commanded to increase the performance of impedance control. We will evaluate these two types of impedance controllers in Chapter IV.

System stability using impedance control is dependent on the target impedance parameter matrices, manipulator dynamics, and the constrained environment. If the target impedance matrices M_d, B, and K are selected as symmetric, positive definite matrices, Kazerooni, et al [14], show the linear impedance control is stable in contact with any directly coupled, stable, linear environment. Colgate and Hogan [13] use the Nyquist criterion to show the stability of the feedback linearlized impedance controller (differents from local linear approximation), which is employed here, in contact with a linear, passive environment. The drawback of these analyses is the modeling of contact interactions as a directly coupled linear system. Such a model of interactions is extremely restrictive. McCormick and Schwartz [12] observed that contact dynamics cause instability when the level of force feedback is sufficiently increased. Based on the small gain theorem, Kazerooni, et al [26], presented an input/output stability proposition for bounded force feedback gain, but two difficulties arise. First, an accurate model of the force environment must be known in order to insure certain necessary conditions, and second, a design based on given sufficient conditions may result in an overly conservative control law [12]. In general, achieving a guarantee of global stability of an impedance control law is very difficult in practice.

Hybrid Impedance Control

Hybrid impedance control (HIC) was proposed by Anderson and Spong [17], combining impedance control and hybrid position/force control. It treats the contact environment as a linear impedance and assumes manipulator dynamics can be decoupled into single-DOF linear subsystems in task space, which in our deburring and grinding operation is described by directions tangential with and normal to the surface. The main idea of HIC is to employ a duality principle to decide which control should be used for different environments in each subsystem. Before using this "duality principal", the environment must be modeled. The scalar impedance Z_e defined here is the ratio of the Laplace transforms of scalar force F and scalar velocity V. It can be represented by a complex number with real part $R(w)$ and imaginary part $X(w)$ for any given frequency w as

$$Z_e(w) = R(w) + jX(w) \tag{3.12}$$

According to Anderson and Spong [17], the impedance of the environment can be classified into three categories: inertial, resistive, and capacitive impedances given by

$$Z_e(0) = \begin{cases} 0 & \text{Inertial impedance} \\ c & \text{Resistive impedance} \\ \infty & \text{Capacitive impedance} \end{cases} \tag{3.13}$$

where $0 < c < \infty$. In Laplace notation, Z_e is given by

$$Z_e(s) = \begin{cases} M_d s & \text{Inertial impedance} \\ M_d s + B & \text{Resistive impedance} \\ M_d s + B + \dfrac{K}{s} & \text{Capacitive impedance} \end{cases} \tag{3.14}$$

where M_d, B, and K represent desired scalar inertia, damping, and stiffness, respectively. By the duality principle, if the environment is capacitive, a force-controlled manipulator with noncapacitive impedance is required; if the environment is inertial, a position-controlled manipulator with noninertial impedance is applied; and if the environment is resistive, either a force-controlled manipulator or a position-controlled manipulator with nonresistive impedance may be applied.

In our deburring and grinding task, the environment is inertial when the end effector moves in free space before contact. According to the duality principle, the inertial environment requires a position-controlled manipulator. Thus, we choose a capacitive manipulator impedance as

$$Z_e = M_d s + B + \frac{K}{s} \tag{3.15}$$

The corresponding differential equation is

$$M_d(\ddot{X} - \ddot{X}_d) + B(X - X_d) + K(X - X_d) = -F \tag{3.16}$$

which is an impedance control identical to that in (3.7), except that the external force, F, is zero in free space. As for impedance control, we obtain our outer loop control from (3.16) with $F = 0$ as

$$\ddot{X} = \ddot{X}_d - \frac{1}{M_d}[B(\dot{X} - \dot{X}_d) + K(X - X_d)] \tag{3.17}$$

for the manipulator with unconstrained motion. After contact, we consider the environment to be capacitive in the normal direction (assuming the material to be deburred acts like a spring in the normal direction), and resistive in the tangential direction [3]. Based on the duality principle, we use a force-controlled manipulator with noncapacitive impedance in the normal direction. For the resistive environment in the tangential direction, either position control or force control should be applied. Considering the nature of the deburring and grinding task, we prefer a position control with a capacitive manipulator impedance in tangential direction [3]. Based on (3.14), we can select our target manipulator impedances as

$$\text{normal direction} \qquad Z_n = M_{dn}s + B_n$$

$$\text{tangential direction} \qquad Z_t = M_{dt}s + B_t + \frac{K_t}{s} \tag{3.18}$$

A force control in the normal direction needs to command a desired normal force F_{dn} and a position control in the tangential direction needs to command desired tangential position x_{dt}, velocity v_{dt}, and acceleration a_{dt}. Then, in the time domain, the corresponding differential equations are

$$\text{normal direction} \qquad M_{dn}a_n + B_n v_n = F_{dn} - F_n$$

$$\text{tangential direction} \qquad M_{dt}(a_t - a_{dt}) + B_t(v_t - v_{dt}) + K_t(x_t - x_{dt}) = -F_t \tag{3.19}$$

where a, v, and x represent scalar acceleration, velocity, and position, respectively, subscripts n and t denote normal and tangential directions, respectively, subscript d shows desired quantities, M, B, and K are positive scalars of desired mass, damping, and stiffness, respectively, and F is external force. Now rearrange (3.19) to fit the servo portion of the control law in (3.2), which yields

$$\ddot{X} = \begin{bmatrix} a_t \\ a_n \end{bmatrix} = \tau' \tag{3.20}$$

where

$$a_n = \frac{(F_{dn} - F_n) - B_n v_n}{M_{dn}}$$

$$a_t = a_{dt} + \frac{B_t(v_{dt} - v_t) + K_t(x_{dt} - x_t) - F_t}{M_{dt}}$$

Eq. (3.20) is the outer loop control in Figure 3.1. Combining (3.20) and (3.4), we obtain the control law for hybrid impedance control, as illustrated in Figure 3.2, for the manipulator with constrained motion, which fits the general structure given in Figure 3.1.

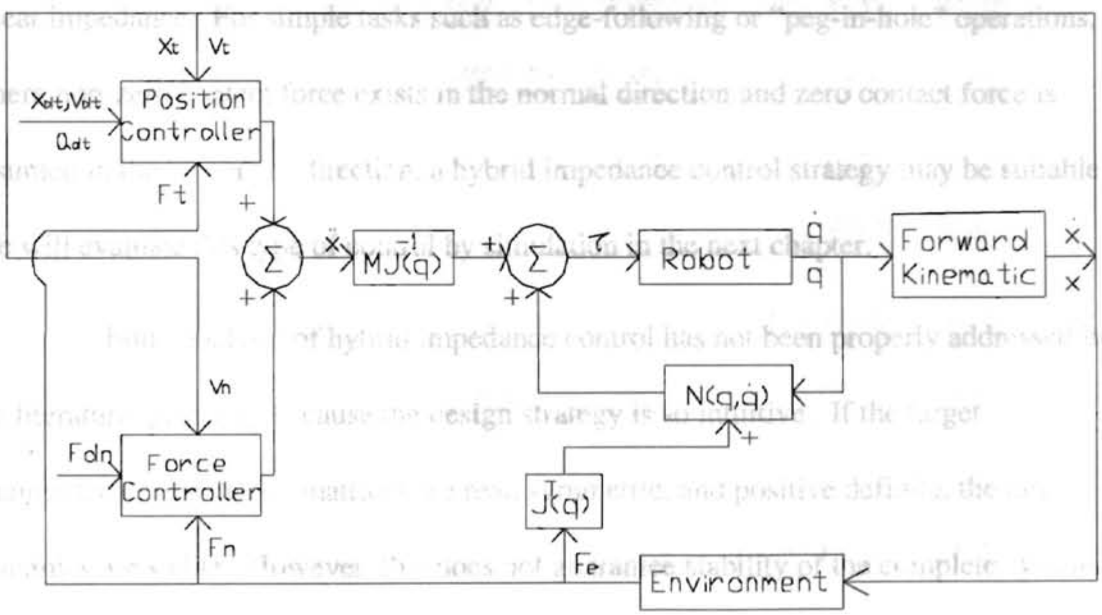

Figure 3.2 Hybrid Impedance Control Diagram

In robotic deburring and grinding, it is intuitive to design the manipulator with a large impedance (small compliance) in the normal direction and small impedance (large compliance) in the tangential direction. A large impedance in the normal direction can cause the end effector to remain insensitive to the grinding forces and remain very close to the commanded (desired) trajectory. A large impedance implies that a position control should be applied in the normal direction. This contrasts with force control used in the hybrid impedance control law developed above. Although using force control in the normal direction may provide stable contact with the workpiece, since displacement in this direction is adjusted indirectly by force control, large position errors may occur with this approach. However, the force environment for the deburring and grinding task is more complicated than mere contact or loss of contact, and can not be represented by a simple linear impedance. For simple tasks such as edge-following or "peg-in-hole" operations, where non-zero contact force exists in the normal direction and zero contact force is assumed in the tangential direction, a hybrid impedance control strategy may be suitable. We will evaluate this type of control by simulation in the next chapter.

Stability analysis of hybrid impedance control has not been properly addressed in the literature, probably because the design strategy is so intuitive. If the target (manipulator) impedance matrices are real, symmetric, and positive definite, the target dynamics are stable. However, this does not guarantee stability of the complete system. Moreover, hybrid impedance control developed for deburring and grinding operations involves switching control after contact because of the change of environment. Contact stability is a difficult problem, which we discuss in the stability analysis of the next section.

Switching Control

In this study, we seek high accuracy in the finished workpiece profile using robotic deburring and grinding. We assume that the actual geometry of the workpiece is unknown, and we wish to finish workpieces of different materials. From our literature review, most proposed control methods for manipulators operating in constrained and unconstrained environments employ some type of force control to obtain stable contact while tracking a desired trajectory. To employ a force-tracking strategy under our assumptions would be very difficult because the surface geometry is unknown and a precise force generation model is required. Moreover, impulsive forces need to be considered when the end effector contacts the workpiece or encounters a large burr. Such demands increase the difficulty in implementing robotic deburring and grinding.

We have reviewed in Chapter I previous work on impact control. Pagilla, et al [18], employed a simple rigid body collision and coefficient of restitution to model impact to demonstrate that bouncing can be eliminated in finite time. However, this approach is not suitable when penetration of the workpiece occurs, as in our deburring problem. Tarn's work [4] may have potential for developing an improved control method for robotic deburring and grinding. In the problem at hand, we consider position control and force regulation of a simple two-arm SCARA robot carrying at its end effector a powered tool used for deburring and grinding. This tool rotates at high speed, while the end effector moves at low speeds in directions tangential with and normal to the nominal surface of the workpiece. When the workpiece is contacted, such tools immediately cut into workpiece, such that the "hard" surface assumed by previous investigators, [4, 8, 18], immediately disappears. Accordingly, impact forces are likely much smaller in our operation, assuming the grinding and robot motor torques can accommodate such forces and provide stable contact. Consider a grinding or deburring tool in contact with a large burr, which suddenly ends, such that the tool momentarily looses contact with workpiece material. We assume that the normal distance from this point to the next point of surface contact is sufficiently small and that the normal distance to the desired trajectory is also small such that the normal velocity of the end effector, under position control in free space, does not become large. This implies that the tool approaches the next surface contact with a relatively low normal velocity. A low approach velocity, coupled with the material removal capacity by the tool, is expected to eliminate bouncing of the tool. A further concern in grinding and deburring is the potential of burning the workpiece or damage to the grinding or deburring tool if the material removal forces are excessive. This can be avoided by controlling the robot such that normal and tangential forces lie below the burning or damage limits, which were addressed in Chapter II. Based on these considerations, we examine a new switching control to implement deburring and grinding. First, we divide our deburring and grinding operations into two phases, namely free space motion and constrained space motion. In free space, a position controller is used to follow a desired trajectory. After contact, when the material removal forces are below the force limits developed in Chapter II, we employ the same position controller to guarantee high accuracy of workpiece edge position. When the grinding forces approach the force limits, force control will be employed to maintain material removal forces below the grinding force limit. This control strategy is different from Hong's approach [3], which under simultaneous position (PD) and force (PI) control will degrade the position accuracy of the workpiece edge and require the command of a desired (but difficult to determine) force.

A position controller can be easily implemented using proportional and derivative control [4]:

$$\ddot{X} = \tau' = \ddot{X}_d + K_d(\dot{X}_d - \dot{X}) + K_p(X_d - X) \tag{3.21}$$

or

$$\ddot{X} = \tau' = \ddot{X}_d + K_d\dot{e}_p + K_p e_p \tag{3.22}$$

where K_d and K_p represent derivative and proportional position gain matrices, respectively, and the position and velocity error matrices $\dot{e}_p$ and e_p are defined by

$$\begin{aligned} \dot{e}_p &= \dot{X}_d - \dot{X} \\ e_p &= X_d - X \end{aligned} \tag{3.22a}$$

This position controller will be employed for position control in free space and constrained space if the material removal forces are below the force limits.

Based on Tarn's work [4], force control using measured position acceleration, $\ddot{X}$, can be developed as

$$\tau' = \ddot{X} + K_f e_f + K_{fi}\int_0^t e_f d\tau \tag{3.23}$$

where K_f and K_{fi} are proportional and integral force gain matrices, respectively, and e_f is a force error matrix defined by

$$e_{fj} = F_{j\lim} - F_j \leq 0 \tag{3.24}$$

where subscript j indicates a vector component and F_{jlim} is a force component limit. We avoid a force time derivative in (3.23) because it is difficult to obtain a noise-force time derivative from a force sensor, which typically contains high frequency components in its measurements. Implementing position acceleration feedback can be difficult, and it adds an acceleration sensor, which will increase hardware cost and typically would provide a very noisy signal. As a tradeoff, we propose eliminating the position acceleration feedback in (3.23), such that the force controller becomes

$$\tau' = K_f e_f + K_{fi} \int_0^t e_f d\tau \tag{3.25}$$

Eq. (3.4) combined with (3.22) and (3.24) establishes our proposed new switching controller. To implement such a control strategy requires measurements of joint position, velocity, and force acting on the end effector by the environment. We assume encoders and tachometers exist on the shafts of the actuators to measure the position and velocity of each joint. A 2-axis force sensor mounted at the end effector on the second link is assumed for force measurements.

Stability Analysis

Stability of Position Control. For the position tracking we use a PD controller, as given by (3.21), which after introducing (3.22a) yields the equation for error dynamics as

$$\ddot{e}_p + K_d\dot{e}_p + K_p e_p = 0 \tag{3.26}$$

From (3.26), it can be seen that $e_{pj} = 0$ is an asymptotically stable equilibrium point for the closed-loop system when K_d and K_p are positive diagonal matrices.

<u>Stability of Force Control</u>. Once the external forces F_j equal F_{jlim}, we switch to PI force control to insure normal and tangential forces remain below their limits to avoid damage to the workpiece and tool. If we employ Tarn's [4] force control in (3.23), where position acceleration feedback is introduced to cancel the effect of acceleration in closed-loop dynamics, we substitute the right side of (3.23) in (3.5) to obtain

$$K_{fj} e_{fj} + K_{fij}\int_0^t e_{fj}\, d\tau = 0 \tag{3.27}$$

for each degree of freedom because the components e_{fj} of vector e_f are decoupled. K_{fj} and K_{fij} are the non-zero elements of diagonal matrices K_f and K_{fi}, respectively. Obviously, the equilibrium point is $e_{fj} = 0$. We assume (i) the trajectory remains in the constrained space and (ii) the gains are positive. Because of decoupling, choose Lyapunov functions V_j as

$$V_j = K_{fij}\left(\int_0^t e_{fj}\, d\tau\right)^2 \tag{3.28}$$

Since we know $e_{fj} < 0$ except at the equilibrium point, V_j is positive and $V_j \to \infty$ as $\|e_{fj}\| \to \infty$. Differentiating the right side of (3.28) with respect to time and employing (3.27) gives

$$\dot{V}_j = 2K_{fij} \cdot \int_0^t e_{fj}\, d\tau \cdot e_{fj} = \frac{-2K_{fij}^{\;2}}{K_{fj}}\left(\int_0^t e_{fj}\, d\tau\right)^2 \tag{3.29}$$

Thus, we see that $\dot{V}_j$ is negative definite and the system is asymptotically stable [27].

Now suppose we eliminate $\ddot{X}$ in (3.23) to obtain a force control in (3.25) that is easier to implement. The error dynamic equation then becomes

$$K_f e_f + K_{fi} \int e_f d\tau - \ddot{X} = 0 \tag{3.31}$$

While we have not been able to prove stability for (3.31), extensive simulations show that the results of this force controller are very close to those of Tarn's controller with acceleration feedback. In what follows, we consider switching between position and force control by partitioning the problem into the two areas of concern, namely, switching stability at contact and switching stability in constrained space.

Stability at Contact. If the material removal forces are below the force limits after contact, our pure position controller is employed for both free space and constrained space. The grinding forces are treated as undesired disturbances and there is no controller switch. The nominal stability of the position control has been established, above, by assuming the grinding and robot motor torques can accommodate such forces and provide a stable contact. If the torques exceed saturation limits, which means robot nonlinearities cannot be properly canceled, multiple deburring passes will be needed to insure torques remain under the limits. However we have been unable to prove stability under torque saturation.

If at contact the material removal forces exceed the force limits during contact, switching occurs from position control to force control. This is similar to Tarn's problem [4], if acceleration feedback is used. His and our switching control strategy employ a position control in free space to eliminate unexpected bouncing and reestablish contact.

Our employment of material removal at contact is expected to soften any bouncing tendency. Tarn has showed that the number of switches is finite and that the last switch always corresponds to the transition from free space to constrained space [4, 8]. In implementation, this requires that the sampling rate of measurement be higher than the bouncing frequency. Without acceleration feedback as proposed by Tarn, we have no contact stability guarantee.

Switching Stability in Constrained Space. First consider that a single switch from position control in steady state to force control occurs in constrained space and that the trajectory remains in constrained space, meaning no loss of contact or "bounce-off". A non-oscillatory force transient response can be achieved, if the integral gain is small enough. Even for relatively large integral gain, a desired non-oscillatory transient response can still be obtained by an appropriate choice of K_f and K_{fi}, such that no loss of contact occurs after switching [4]. Therefore, a single switch from a steady state of position control to force control may remain stable. A single switch from steady state force control to position control is stable if gains are properly chosen. Now, considering frequent switching between the two controllers around F_{limit}, while our simulations indicate stability and good dynamic behavior with suitable gains choices, we have been unable to prove stability of the complete system. While such proof is important, it is beyond the scope of this work.

In this chapter, we have discussed and proposed several controllers which may be suitable for robotic deburring and grinding. In next chapter, we will use computer simulation to test and evaluate the performance of these approaches.

CHAPTER IV

COMPUTER SIMULATIONS

In this chapter, we numerically evaluate several control approaches for robotic deburring and grinding using the Berkeley two-arm SCARA robot described in Chapter II. Several types of burrs have been generated numerically to simulate rough edges, and a motion plan has been designed for computer simulations. The simulation results are presented for different controllers for an "easy-to-grind" (ETG) and a "difficult-to-grind" (DTG) material. We assume that the computations can be performed quickly enough that the continuous time assumption is valid.

Simulation Parameters and Motion Plan

A UC-Berkeley/NSK SCARA robot [19] has been employed as a benchmark for our simulations because its configuration as a two axis robotic arm provides a planar workspace, and because the technical data for this robot are available. The manipulator parameters used in (2.17) for this robot are given as [3]:

$I_1 = 0.2675$ kg m^2, $I_2 = 0.36$ kg m^2, $I_3 = 0.0077$ kg m^2, $I_4 = 0.051$ kg m^2,
$I_{3c} = 0.04$ kg m^2, $I_p = 0.046$ kg m^2;
$m_1 = 73$ kg, $m_2 = 10.6$ kg, $m_3 = 12$ kg, and $m_4 = 4.85$ kg, $m_p = 6.81$kg;
$l_1 = 0.36$ m, $l_2 = 0.24$ m, $l_{1c} = 0.139$ m, and $l_{2c} = 0.099$ m;

$th_1 = 5.5$ N - m, and $th_2 = 0.9$ N - m.

The maximum torques for motors 1 and 2 are 245.0 N-m and 39.2 N-m, respectively. These torque limits are used in a saturation function in computer simulations to avoid overloads of the robot actuators.

The ETG and DTG workpieces to be deburred, or ground, in our examples are metal plates of R_c 60, AISI 52100 steel and R_c 64, M4 alloy, respectively, with a thickness of 10 mm. We propose to grind the edges of these plates, such that we take this thickness as the active width of cut b. The diameter of grinding wheel is 50.8 mm (2 in.). We assume the grinding wheel diameter is large compared to the peak heights of burrs, and that the thickness of the grinding wheel is greater than the thickness of workpiece. The grinding wheel and grinding conditions are described in Chapter II. The values of the metal removal parameter Λ_m are repeated here as 0.00871 in^3/(min, lb) (5.3484×10^{-10} m^3/(sec, N)) for the ETG material and 0.002 in^3/(min, lb) (1.228×10^{-10} m^3/(sec, N)) for the DTG material. For simplicity, in the simulations of this study, we set the grinding friction coefficient at $\mu = 0.7$. Note from (2.21) that this reasonably high friction coefficient means that the tangential grinding forces will be relatively large, although this could be reduced by employing lubricating coolant.

The desired position and velocity of the grinding trajectory are given in Cartesian space. The total simulation time is set at 10 seconds, and the workpiece edge to be ground is aligned in the x direction of Cartesian space and is designated by $0.1\ m \le x \le 0.2\ m$. The desired motion plan for simulations is as follows:

- Desired velocity $\dot{X}_d = \begin{bmatrix} 0.012 \\ 0 \end{bmatrix}$ m/s

- Desired position $X_d = \begin{bmatrix} 0.08 + 0.012\,t \\ 0.4 \end{bmatrix}$ m

- Desired acceleration $\ddot{X}_d = \begin{bmatrix} 0 \\ 0 \end{bmatrix}$ m/s^2

where the matrix notation $\begin{bmatrix} x \\ y \end{bmatrix}$ indicates components in the x and y directions, and t is the current simulation time. The starting point of the end effector is $\begin{bmatrix} 0.08 \\ 0.399 \end{bmatrix}$ m. Figure 4.1 illustrates a sample of end point motion of the robot reaching the desired trajectory in Cartesian space.

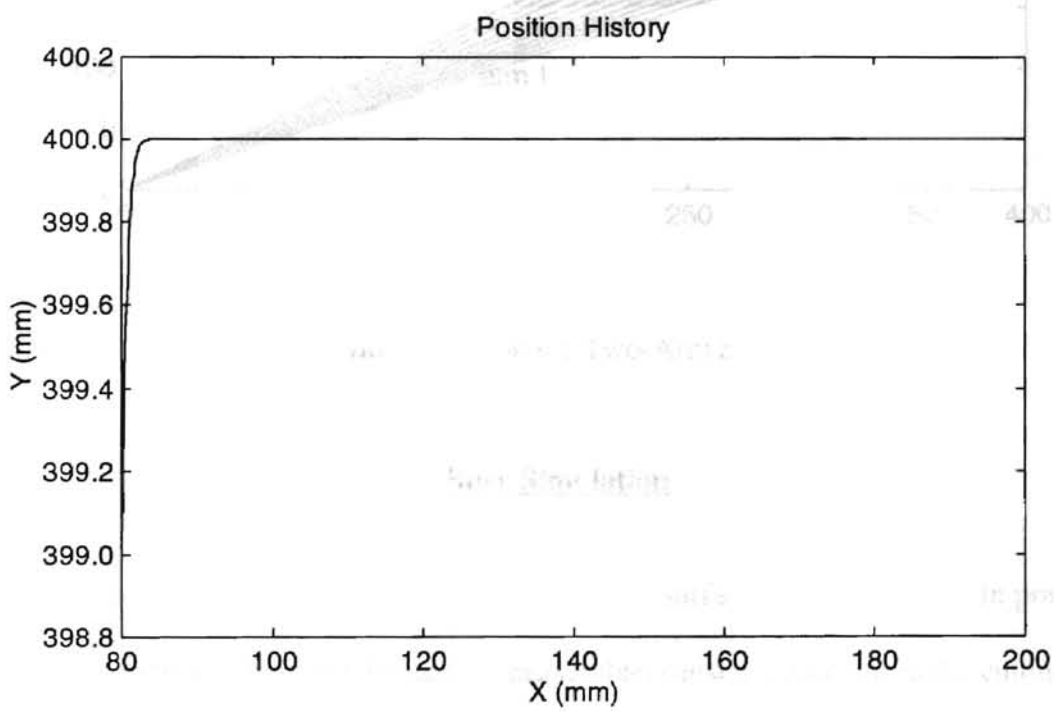

Figure 4.1 End Point Motion of Robot to Desired Trajectory

A scaled line drawing of the robot link positions at the beginning and end of the desired trajectory is given in Figure 4.2. For force control, we employ an absolute force limit of 483 N, as developed in Chapter II. In our simulations, we employ a somewhat smaller value of 450 N to provide a small margin for error.

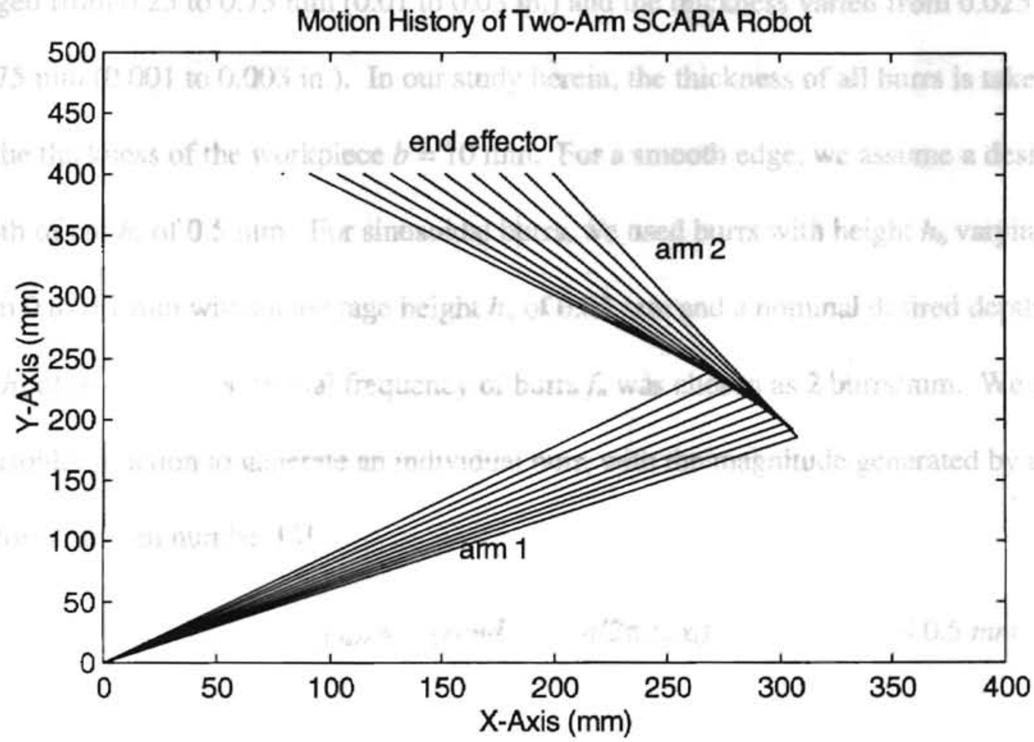

Figure 4.2 Motion History of Two-Arm SCARA Robot

Burr Simulation

Burrs are unwanted irregularities on the edge surface of a workpiece. In practice, we assume they are unpredictable and unmeasurable, causing variations in the cutting force. In this section, we numerically generate three different types of burrs, namely random-height sinusoidal, large upset, and scallop to simulate rough surfaces of workpieces.

A typical burr is highly variable. Kazerooni, et al [28], generated a geometric model of a burred workpiece edge from statistical data based on the burr height and root thickness measurements made on aircraft engine parts. In this work, average burr height ranged from 0.25 to 0.75 mm (0.01 to 0.03 in.) and the thickness varied from 0.025 to 0.075 mm (0.001 to 0.003 in.). In our study herein, the thickness of all burrs is taken to be the thickness of the workpiece $b = 10$ mm. For a smooth edge, we assume a desired depth of cut h_c of 0.5 mm. For sinusoidal burrs, we used burrs with height h_b varying from 0 to 0.1 mm with an average height h_a of 0.05 mm and a nominal desired depth of cut h_c of 0.5 mm. The spatial frequency of burrs f_b was chosen as 2 burrs/mm. We use a sinusoidal function to generate an individual burr, with the magnitude generated by a uniform random number [3]

$$y_{burr} = h_b(rand) \times \sin(2\pi f_b x_t) \qquad 0 \le x_t \le 0.5\ mm \tag{4.1}$$

where

y_{burr} = y-coordinate of burr edge

$h_b(rand)$ = burr height randomly generated every 0.5 mm

Examples of burr geometry and the sinusoidal burr edge are illustrated in Figure 4.3a and b, respectively.

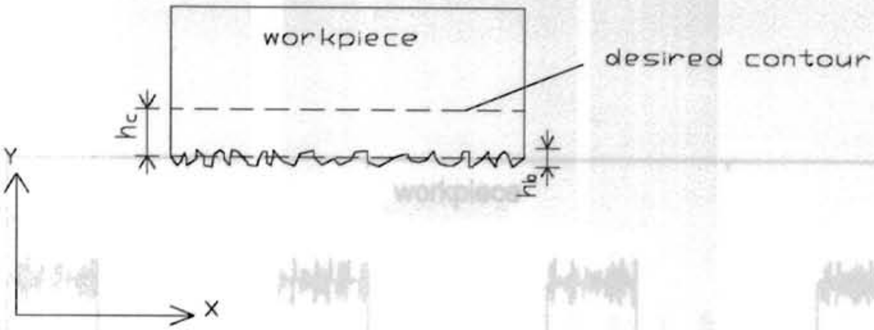

(a)

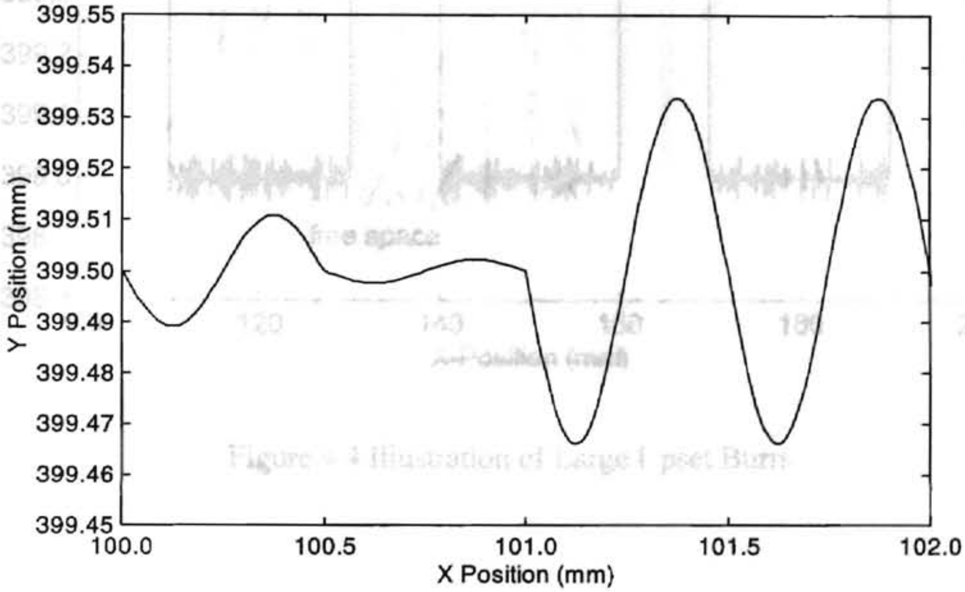

(b)

Figure 4.3 Geometry of Sinusoidal Burrs

For large upset burrs, we begin with a rough surface modeled by random-height sinusoidal burrs with average burr height $h_a = 0.04$ mm and burr frequency $f_b = 2$ burrs/mm. On this surface, we superimpose 3 step-up, step down pulses of height 0.6 mm and width 20 mm, separated by 10 mm, as illustrated in Figure 4.4. This was handled in the simulations by step changes in the nominal desired depths of cut from $h_c = 0.4$ to $h_c = 1.0$ mm, and back.

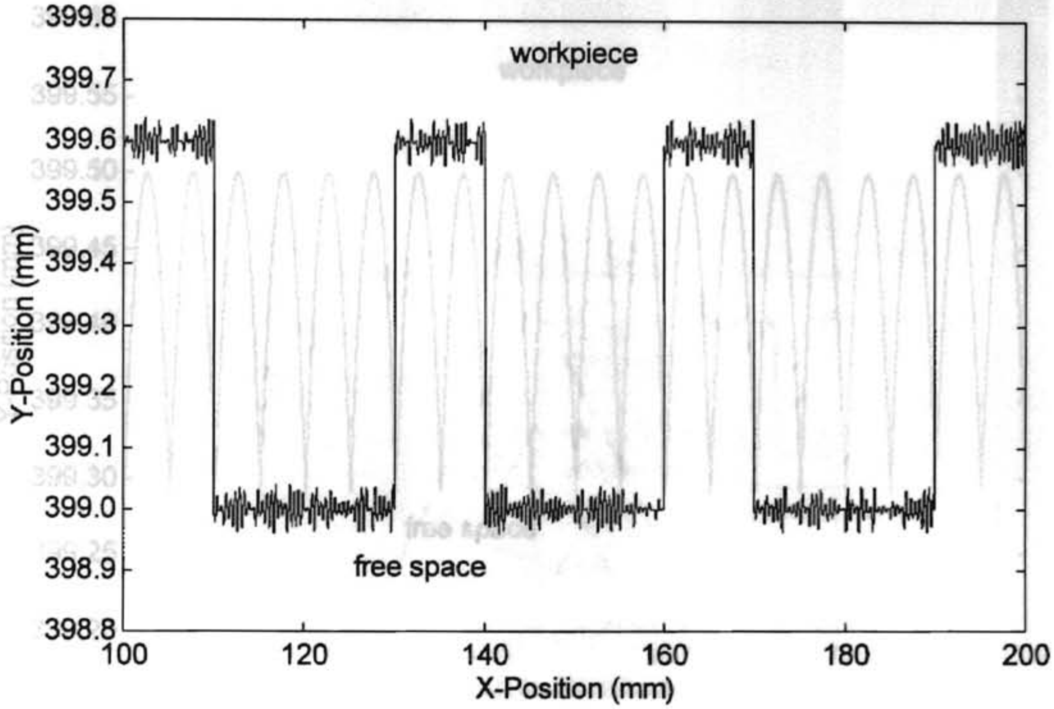

Figure 4.4 Illustration of Large Upset Burrs

Some automobile parts are produced by a ball-shaped end mill tool [3], which can leave a surface with a regular "scallop-shaped" contour. The size and frequency of scallops are dependent on the tool dimension and the number of passes per unit width of surface. In this study, we examine scallop-shaped burrs by assuming the diameter of the ball-shaped mill is 30 mm, with a 5 mm span of tool passes. This can produce a 0.21 mm scallop height h_b and a frequency f_b 200 scallops per meter, illustrated in Figure 4.5.

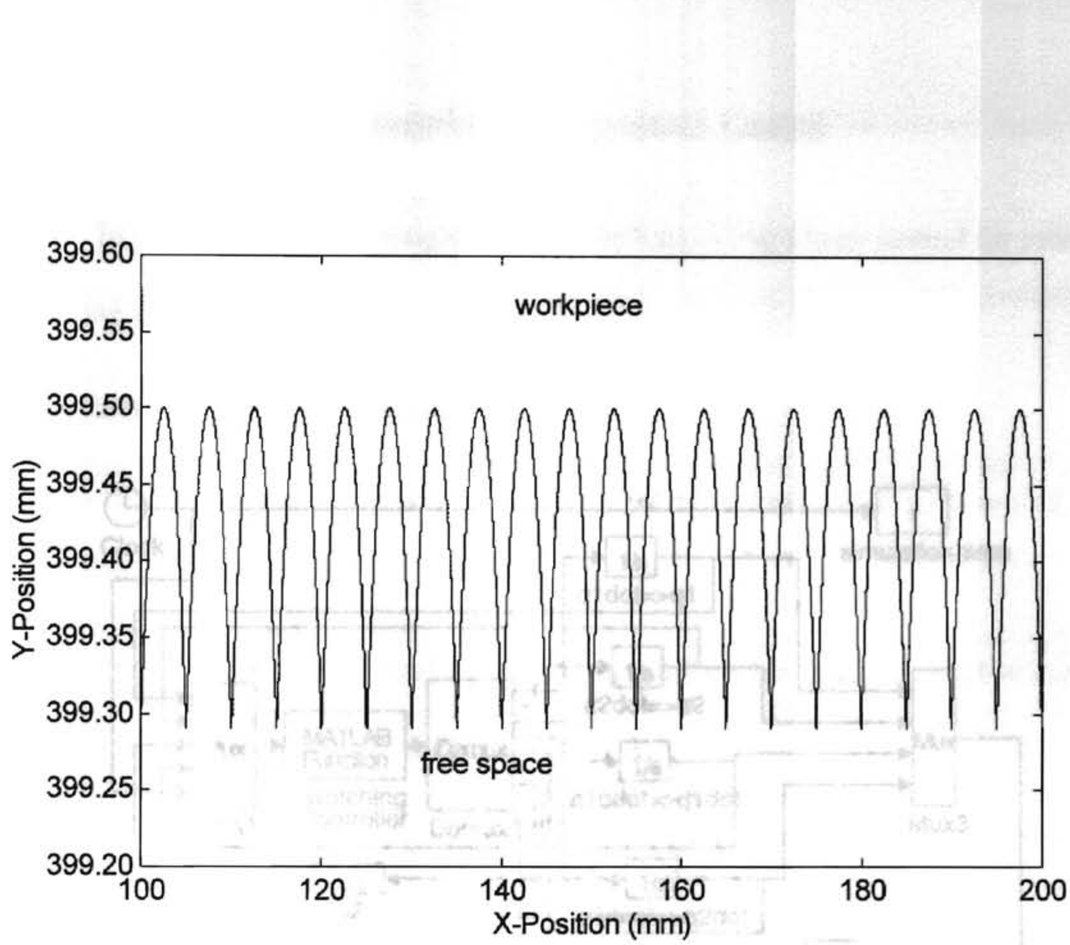

Figure 4.5 Illustration of Scallop Burrs

Several artificial surfaces have been developed to investigate robotic deburring and grinding here. In next section, we use computer simulation to employ different controllers in grinding these artificial surfaces. In our simulations, we will investigate three issues: (i) dynamic behavior of contact between the end effector and the workpiece, (ii) achievable performance with and without motor torque limits, and (iii) ability to accommodate large upset burrs. All source code is written in MATLAB 4.2c [29], and simulations are completed by SIMULINK 1.3c [30] using the automatic step size, Runge-Kutta 45 algorithm. Figure 4.6 presents a block diagram of the SIMULINK code.

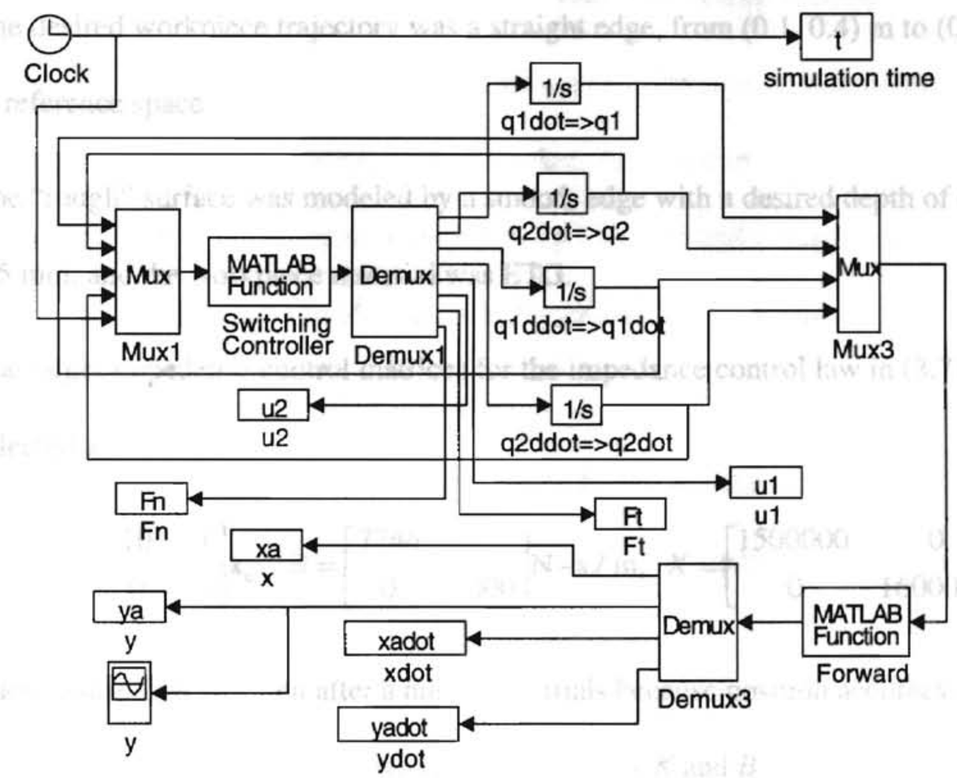

Figure 4.6 SIMULINK Block Diagram

Simulations for Impedance Control

In this section, we investigate five simulations of impedance control for robotic deburring and grinding:

Simulation 1: Smooth Straight Edge

- The desired workpiece trajectory was a straight edge, from (0.1, 0.4) m to (0.2, 0.4) m in reference space.
- The "rough" surface was modeled by a smooth edge with a desired depth of cut h_c = 0.5 mm, and the workpiece material was ETG.
- The target impedance control matrices for the impedance control law in (3.7) were selected as:

$$M_d = \begin{bmatrix} 10 & 0 \\ 0 & 10 \end{bmatrix} \text{kg}, \; B = \begin{bmatrix} 7746 & 0 \\ 0 & 8000 \end{bmatrix} \text{N - s / m}, \; K = \begin{bmatrix} 1500000 & 0 \\ 0 & 1600000 \end{bmatrix} \text{N / m}$$

These values were chosen after a number of trials because position accuracy could be improved by increasing parameter values in matrices K and B.

- Results showing position errors, external forces, and motor torques are given in Figures 4.7-4.9. The external forces applied to the end effector are positive, such that the torques applied to the workpiece are negative.

Simulation 2: Random-Height Sinusoidal Burrs

- The same simulation conditions as in Simulation 1 were used, except the smooth edge was replaced by a rough surface described by sinusoidal burrs with average burr height

h_a = 0.05 mm and burr frequency f_b = 2 burrs/mm. The nominal desired depth of cut h_c is 0.5 mm and the workpiece material was ETG.

- Results showing position errors, external forces, and motor torques are given in Figures 4.10-4.12.

Simulation 3: Random-Height Sinusoidal Burrs with Desired Force Compensation

- In this simulation, we used the same simulation conditions as in Simulation 2, except we employed an alternate impedance controller, described by (3.10), by including desired contact forces at the desired trajectory. The desired contact forces were obtained from Eq. (2.21) for desired velocity and desired depth of cut.

- Results showing position errors, depth of cut and remaining depth of cut, external forces, and motor torques are given in Figures 4.13-4.16. Remaining depth of cut is defined by the end point position of the end effector after grinding minus desired position.

Simulation 4: Large Upset Burrs

- The same simulation conditions as in Simulation 1 were used, except the rough surface was modeled as large upset burrs, as in Figure 4.4. The material was ETG.

- Results showing position errors, depth of cut and remaining depth of cut, external forces, and motor torques are given in Figures 4.17-4.20.

Simulation 5: Large Upset Burrs with Desired Force Compensation

- In this simulation, we used the same simulation conditions as in Simulation 4, except we employed the alternate impedance controller, described by (3.10), by including desired contact forces at the desired trajectory.
- Results showing position errors, depth of cut and remaining depth of cut, external forces, and motor torques are given in Figures 4.21-4.24.

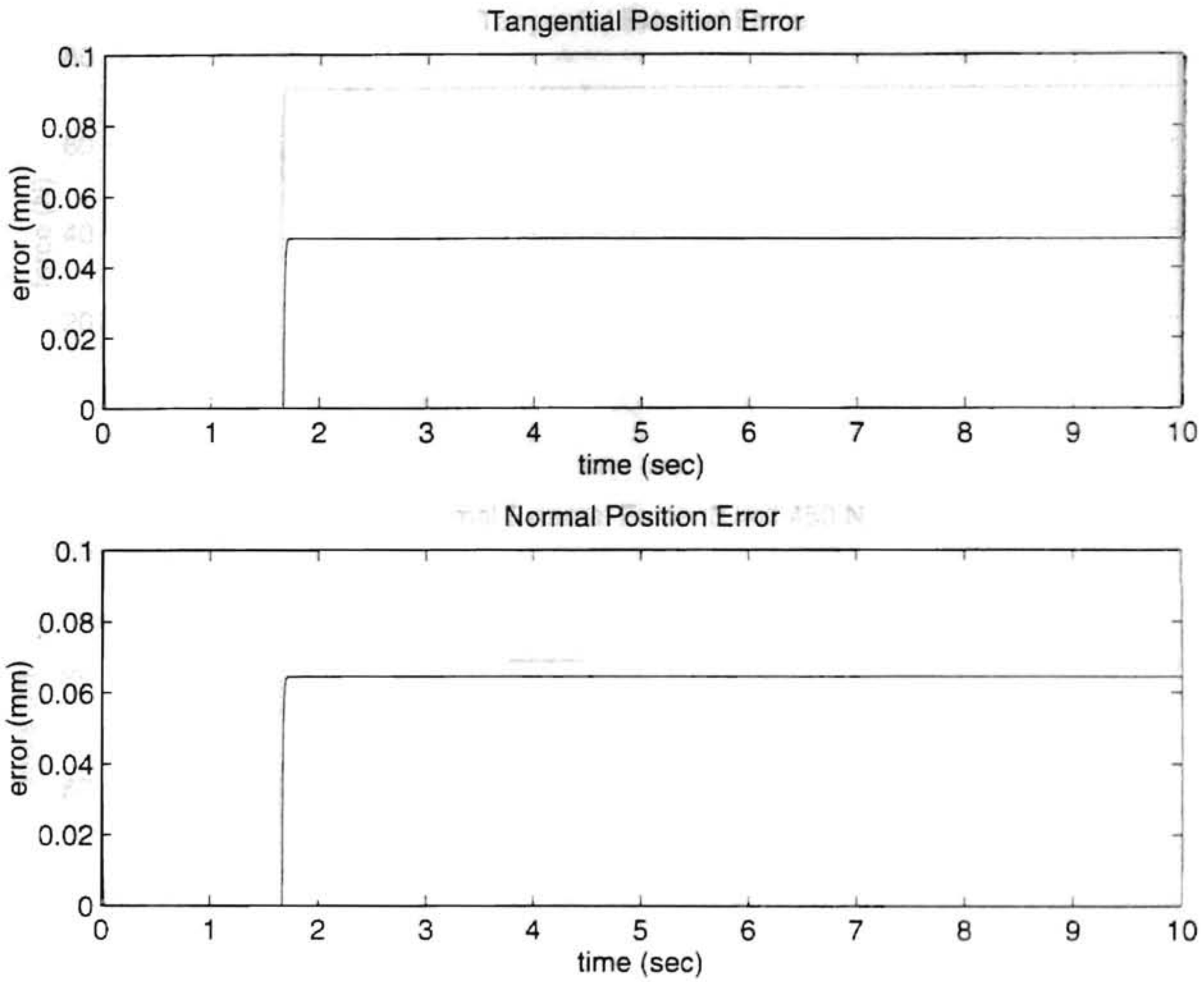

Figure 4.7 Results of Simulation 1 with Impedance Control: Position Errors

Smooth Straight Edge

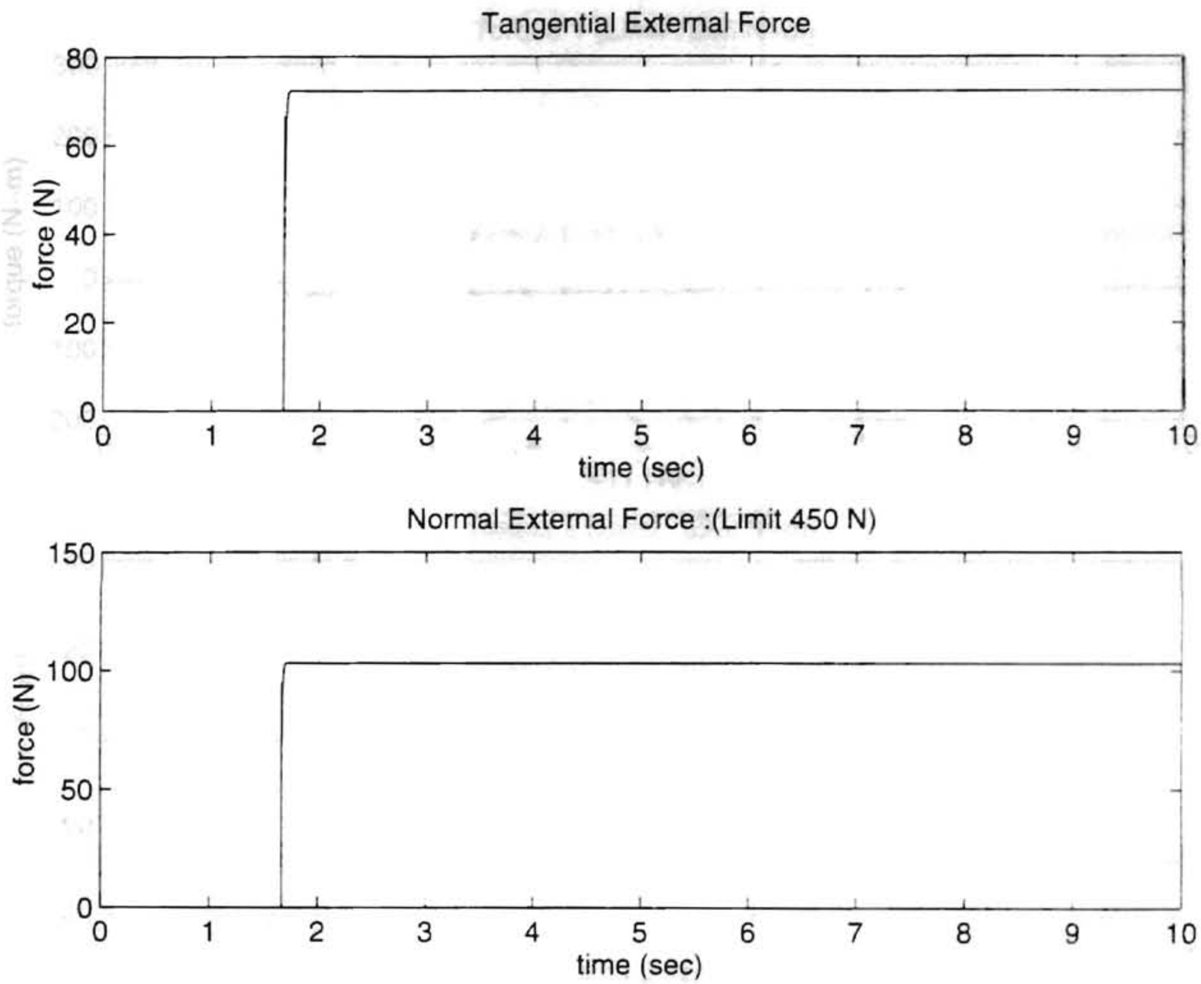

Figure 4.8 Results of Simulation 1 with Impedance Control: External Forces

Smooth Straight Edge

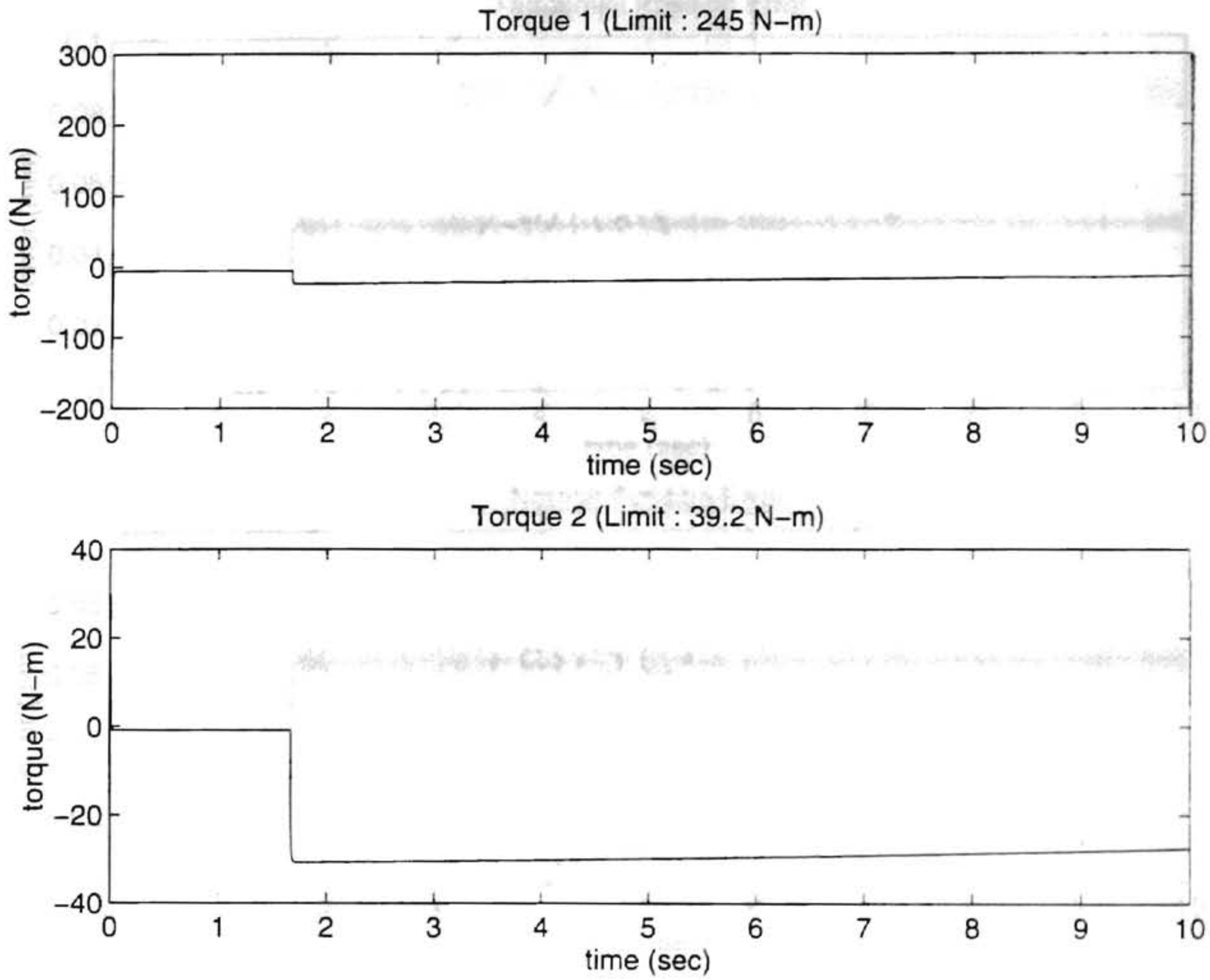

Figure 4.9 Results of Simulation 1 with Impedance Control: Motor Torques

Smooth Straight Edge

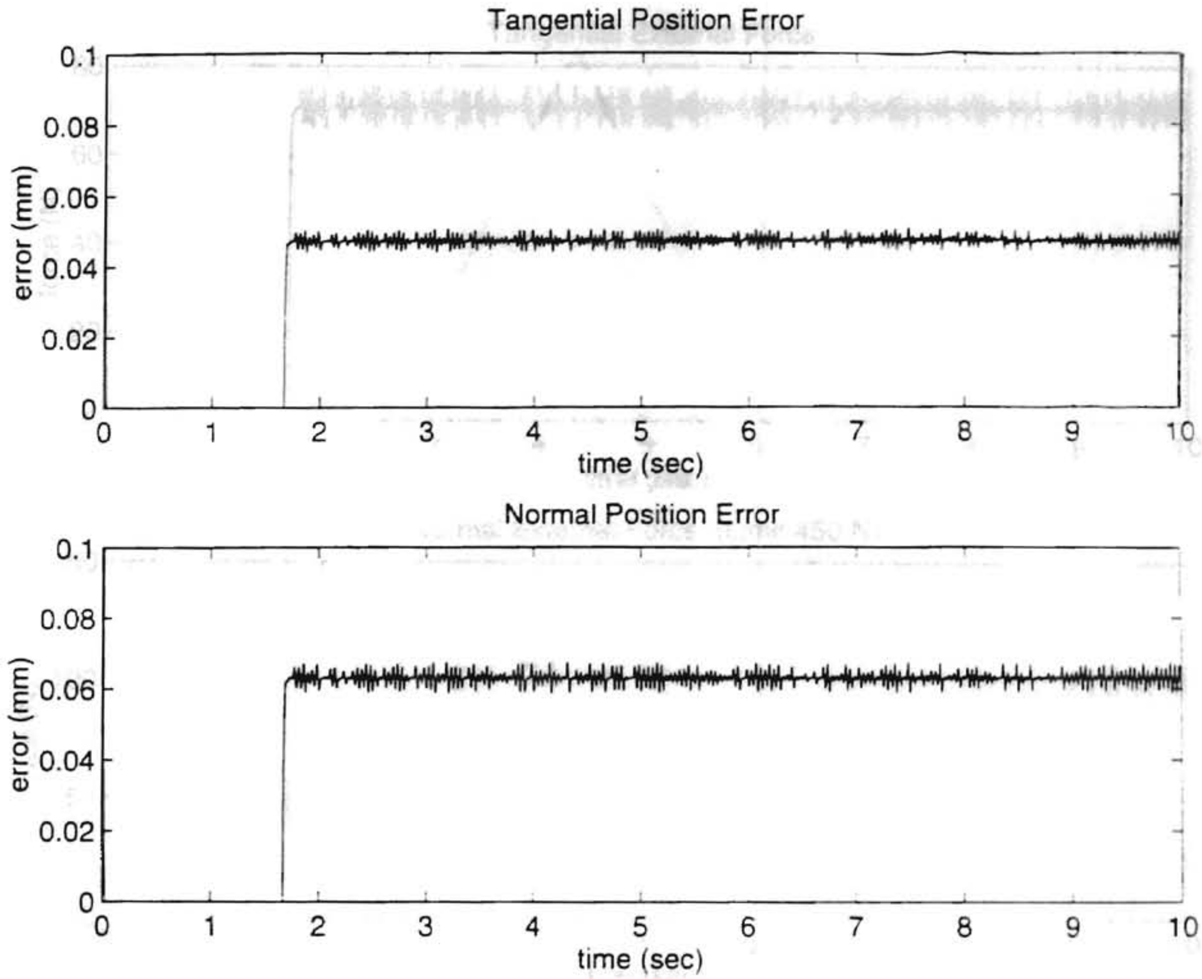

Figure 4.10 Results of Simulation 2 with Impedance Control: Position Errors

Random-Height Sinusoidal Burrs

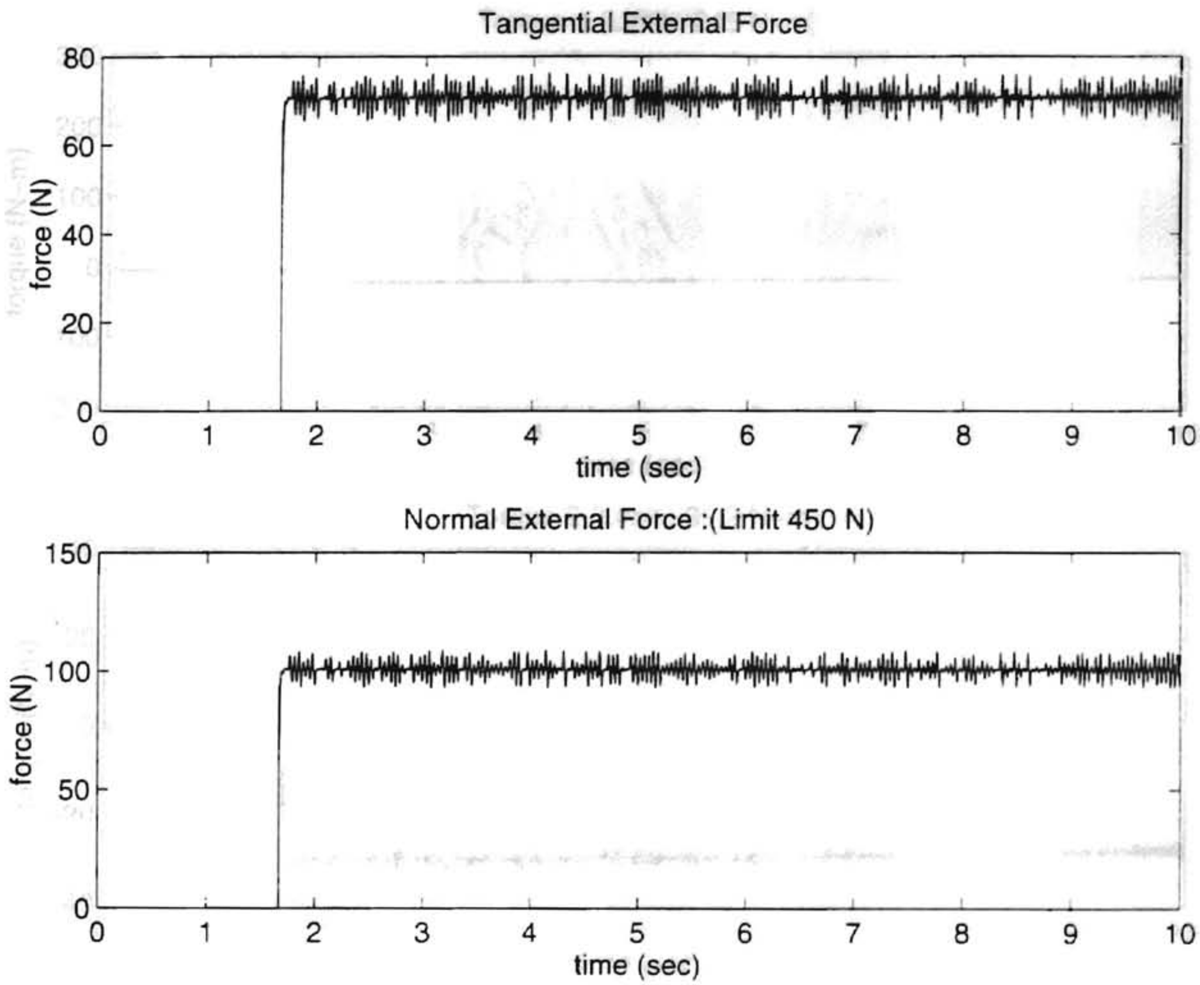

Figure 4.11 Results of Simulation 2 with Impedance Control: External Forces

Random-Height Sinusoidal Burrs

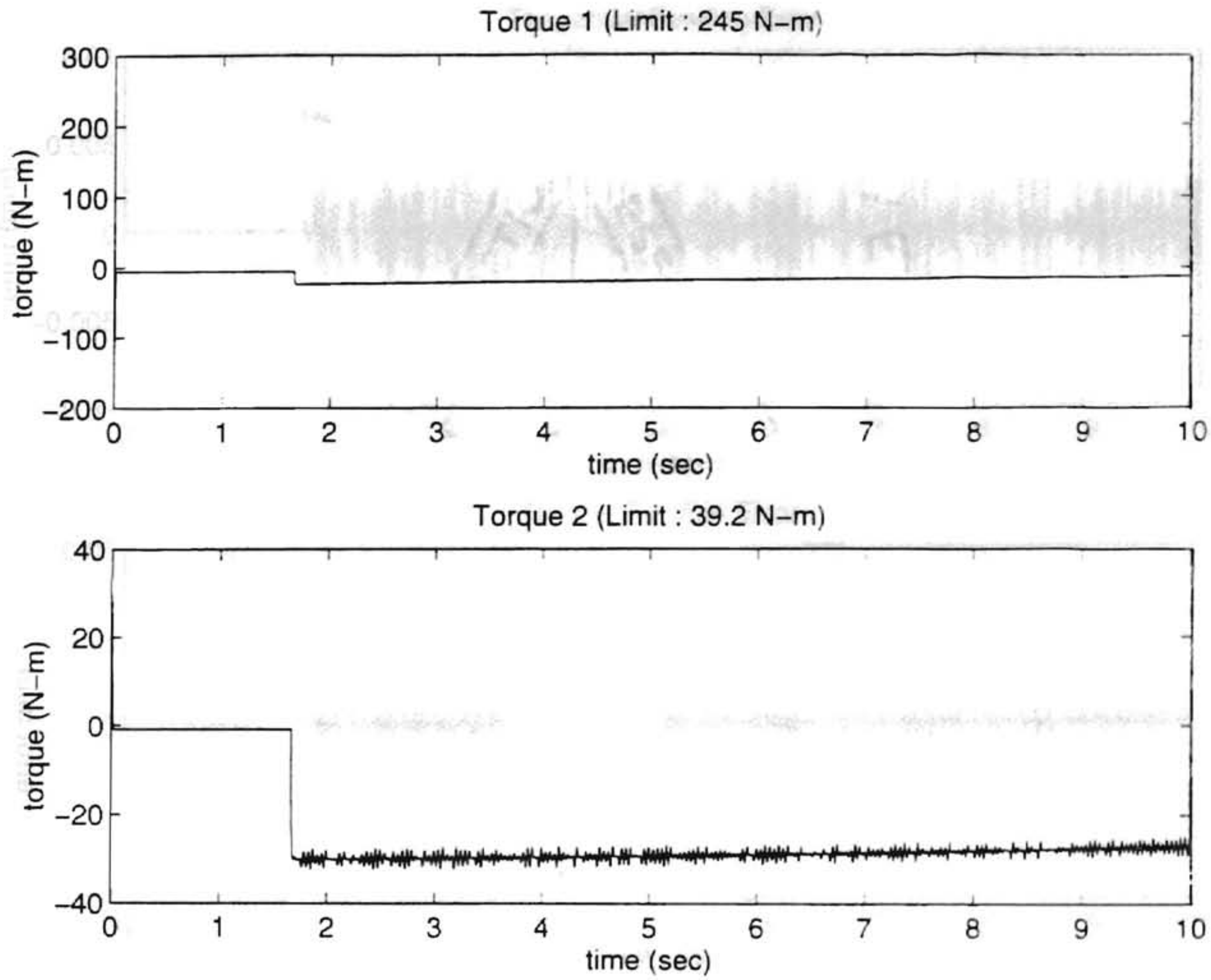

Figure 4.12 Results of Simulation 2 with Impedance Control: Motor Torques

Random-Height Sinusoidal Burrs

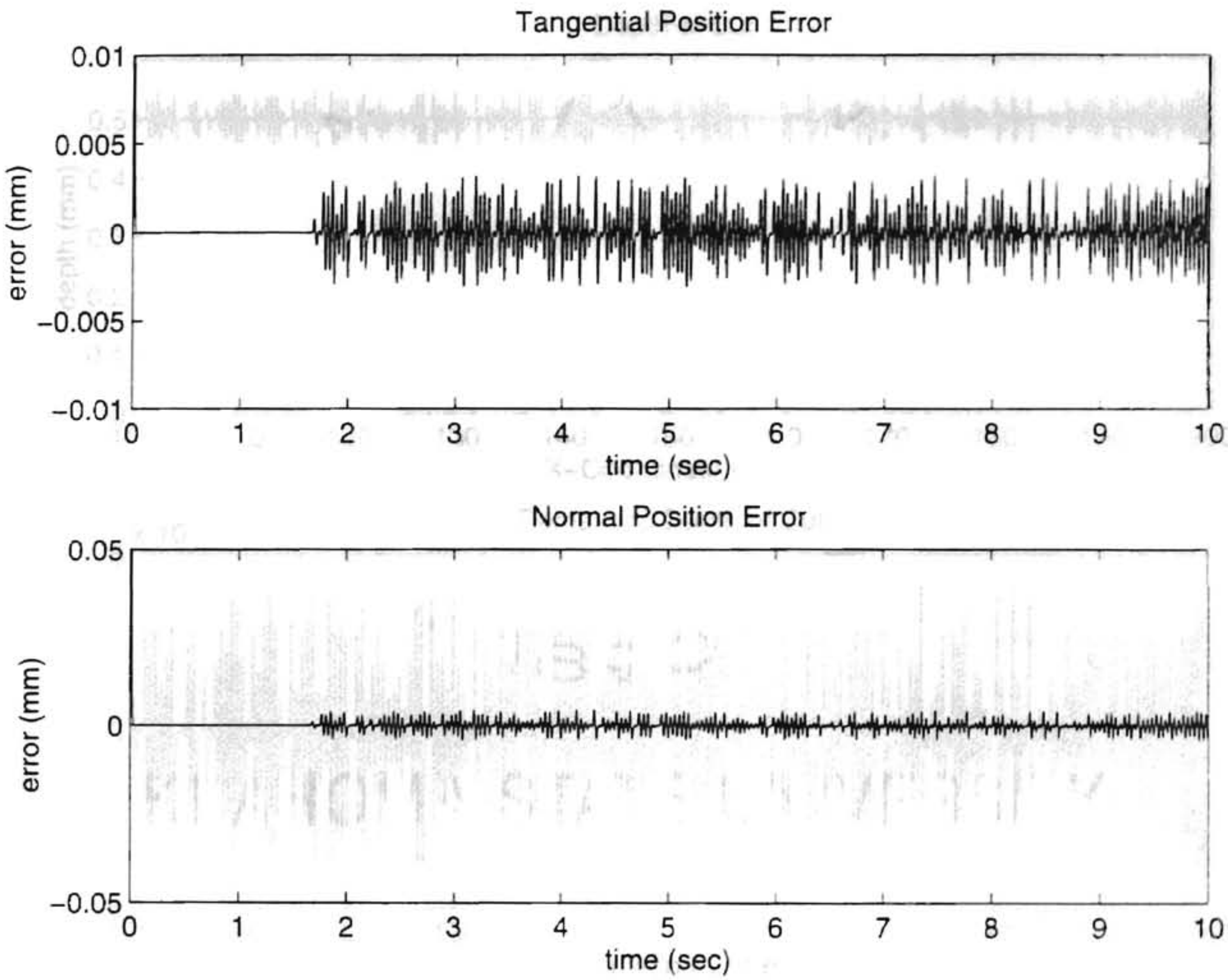

Figure 4.13 Results of Simulation 3 with Impedance Control: Position Errors

Random-Height Sinusoidal Burrs with Desired Force Compensation

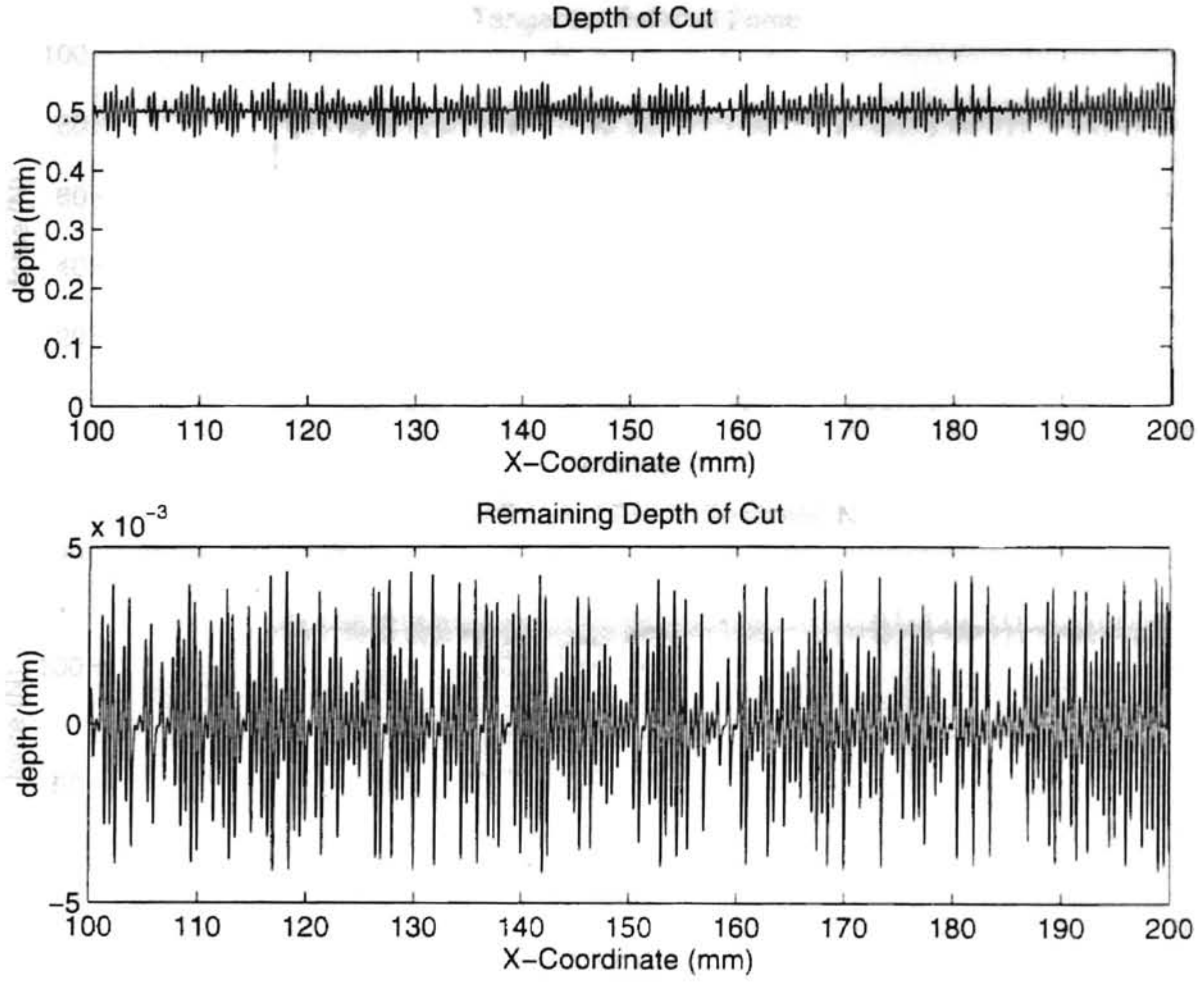

Figure 4.14 Results of Simulation 3 with Impedance Control: Depth of Cut and Remaining Depth of Cut

Random-Height Sinusoidal Burrs with Desired Force Compensation

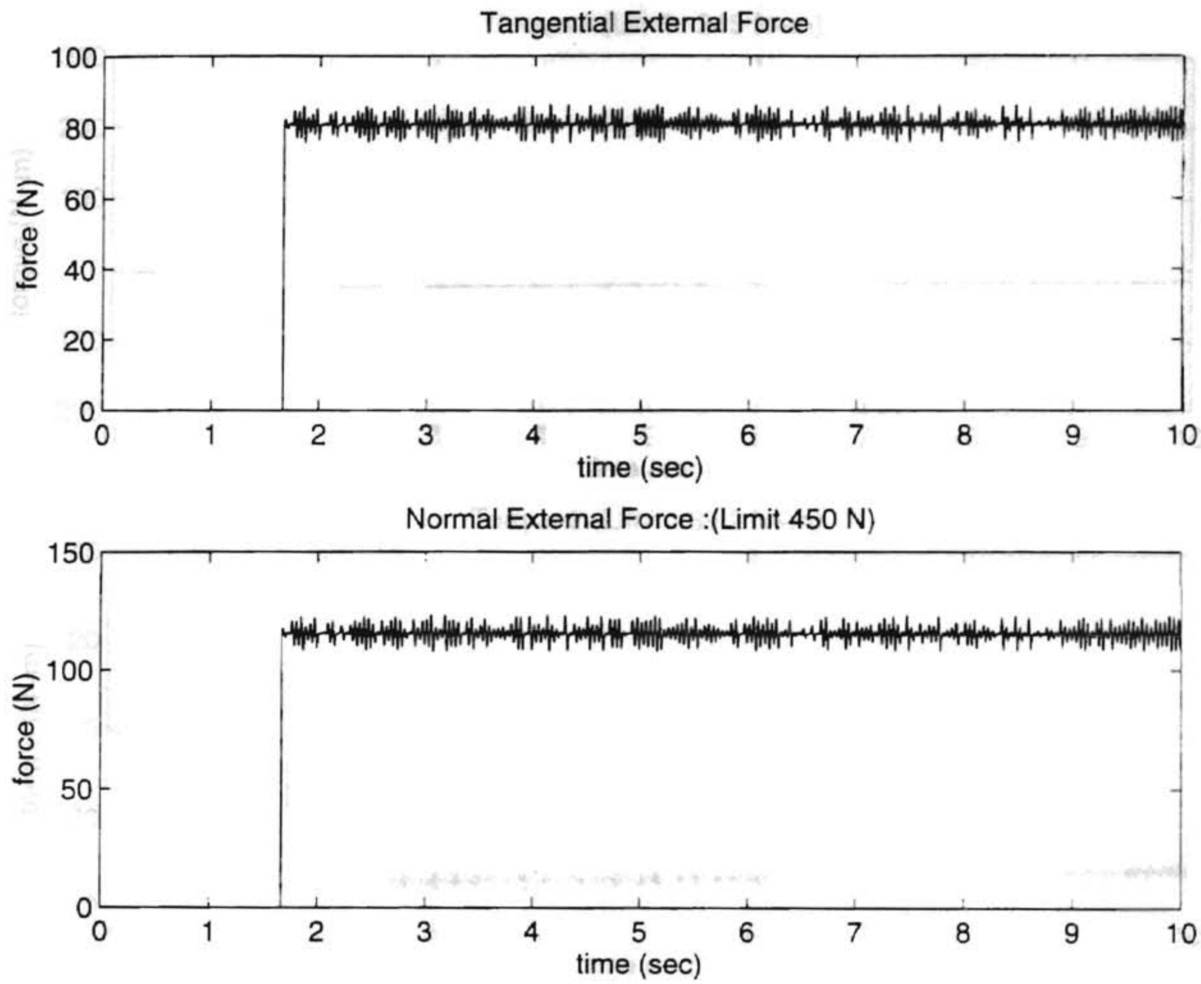

Figure 4.15 Results of Simulation 3 with Impedance Control: External Forces

Random-Height Sinusoidal Burrs with Desired Force Compensation

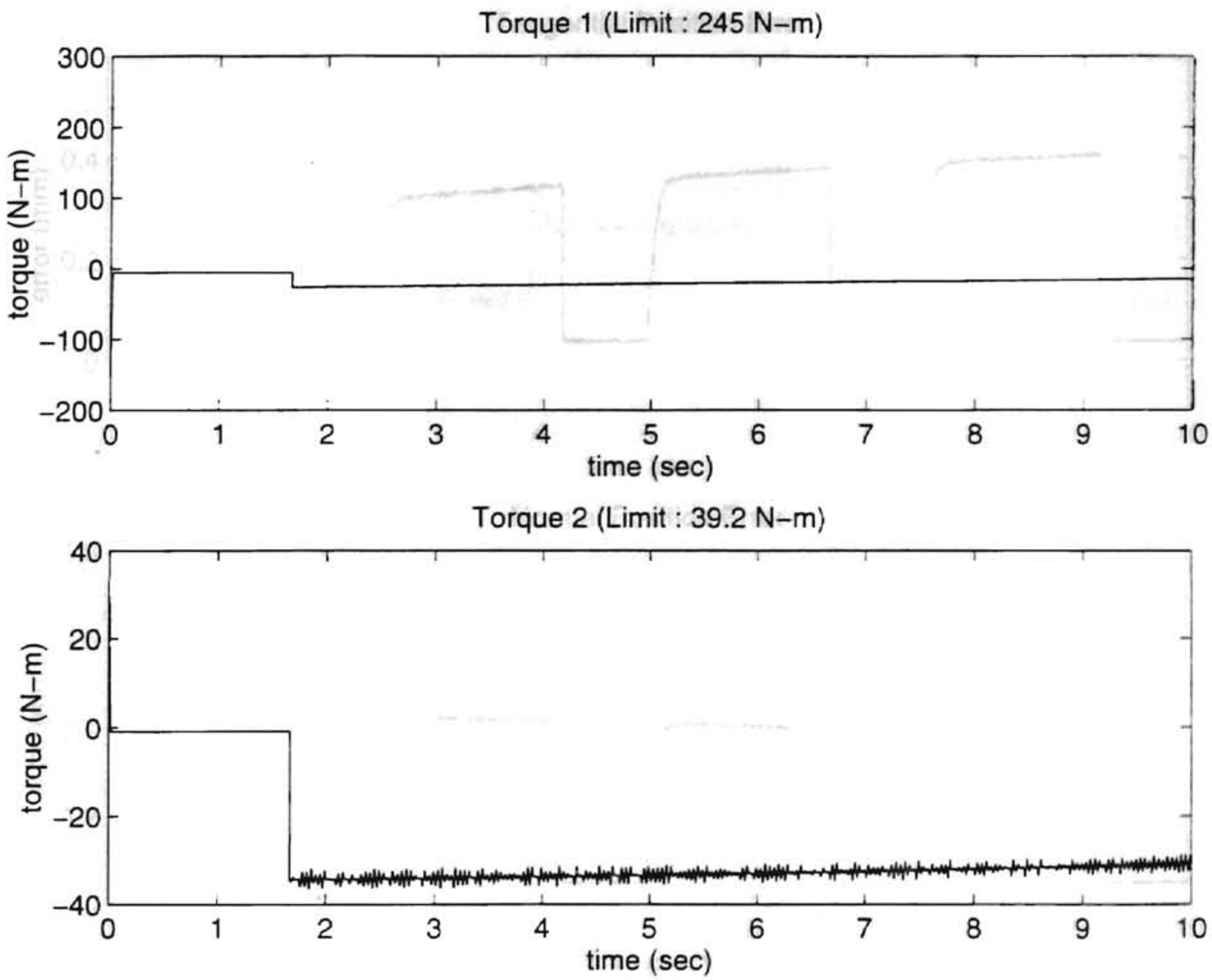

Figure 4.16 Results of Simulation 3 with Impedance Control: Motor Torques

Random-Height Sinusoidal Burrs with Desired Force Compensation

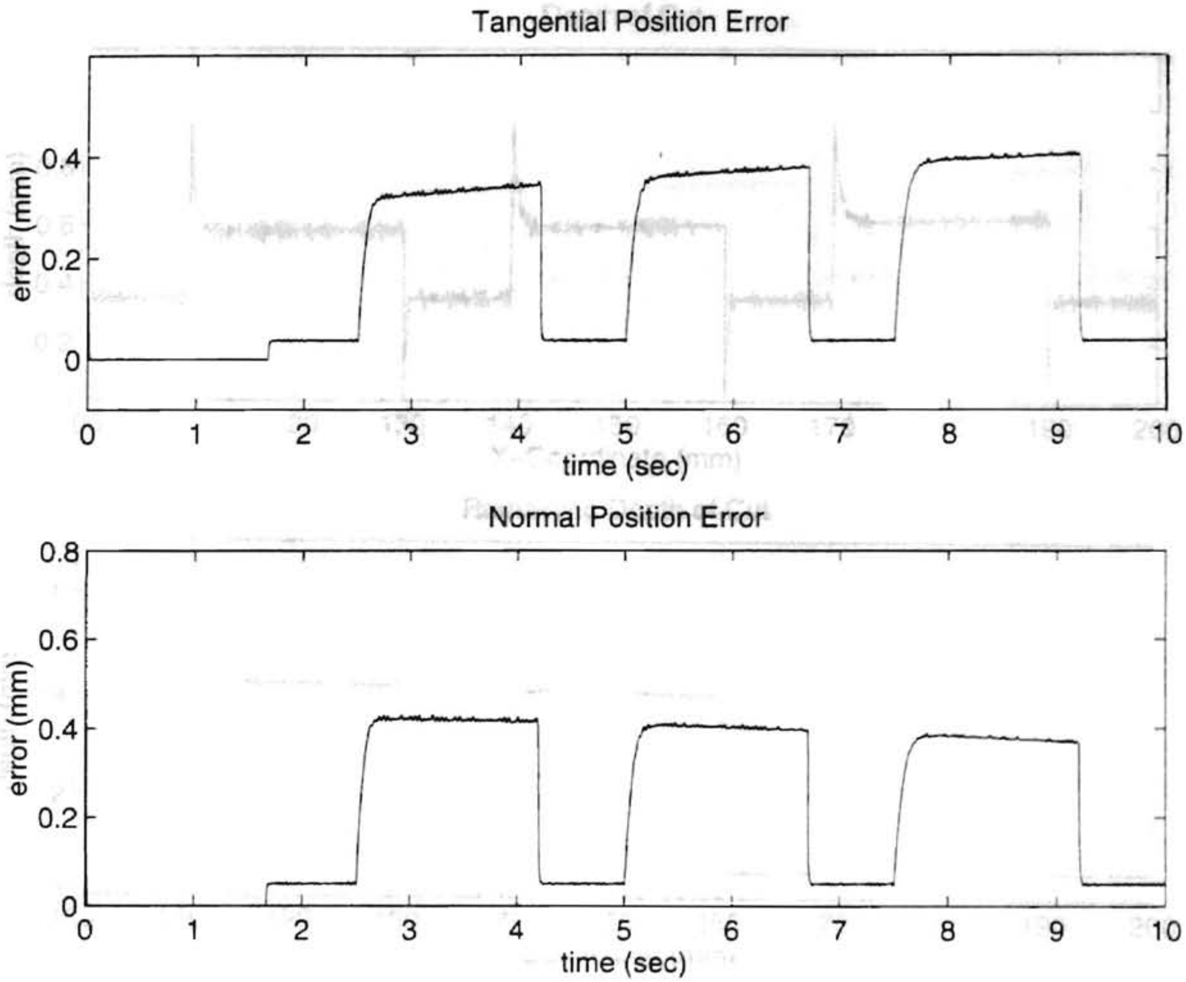

Figure 4.17 Results of Simulation 4 with Impedance Control: Position Errors

Large Upset Burrs

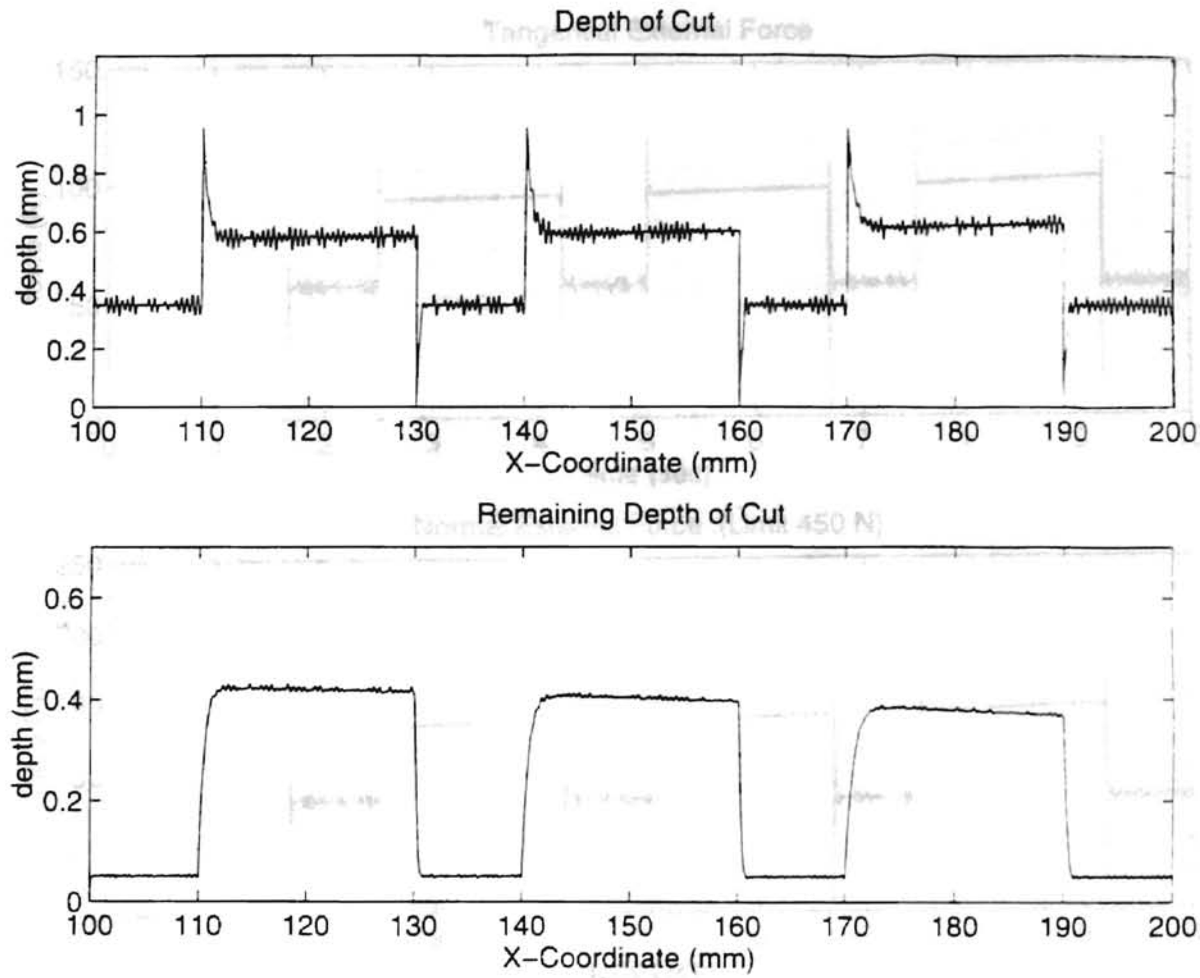

Figure 4.18 Results of Simulation 4 with Impedance Control: Depth of Cut and

Remaining Depth of Cut

Large Upset Burrs

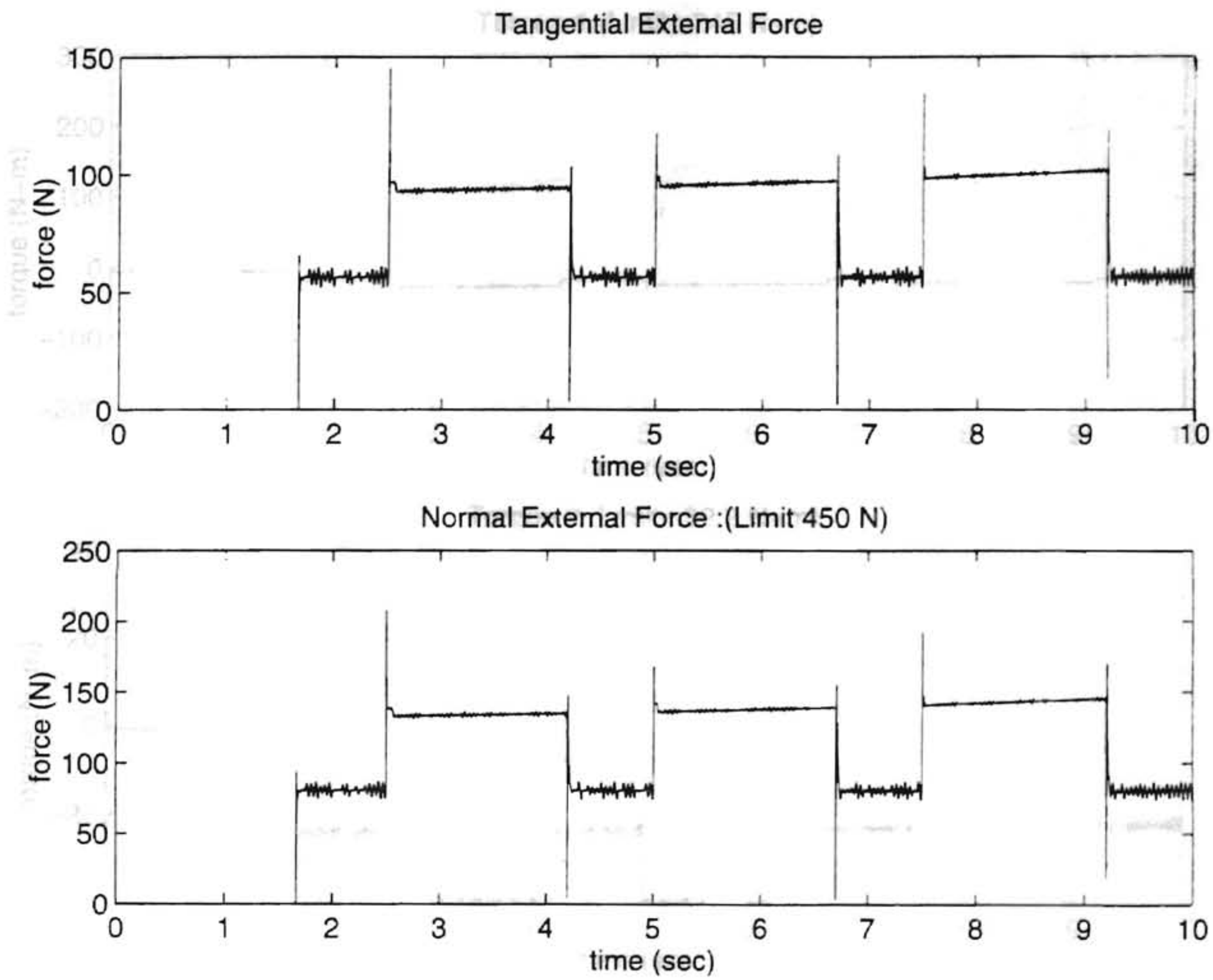

Figure 4.19 Results of Simulation 4 with Impedance Control: External Forces

Large Upset Burrs

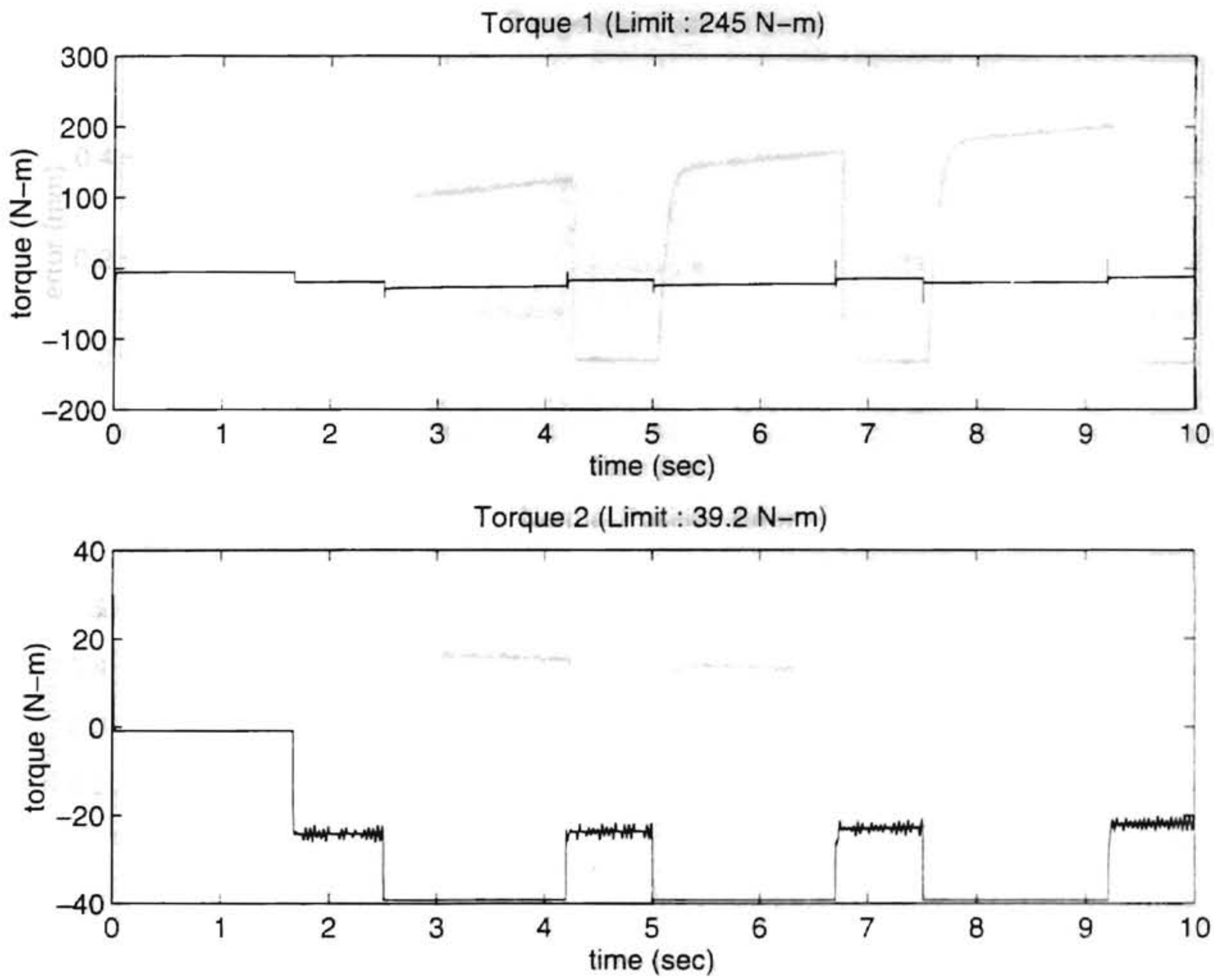

Figure 4.20 Results of Simulation 4 with Impedance Control: Motor Torques

Large Upset Burrs

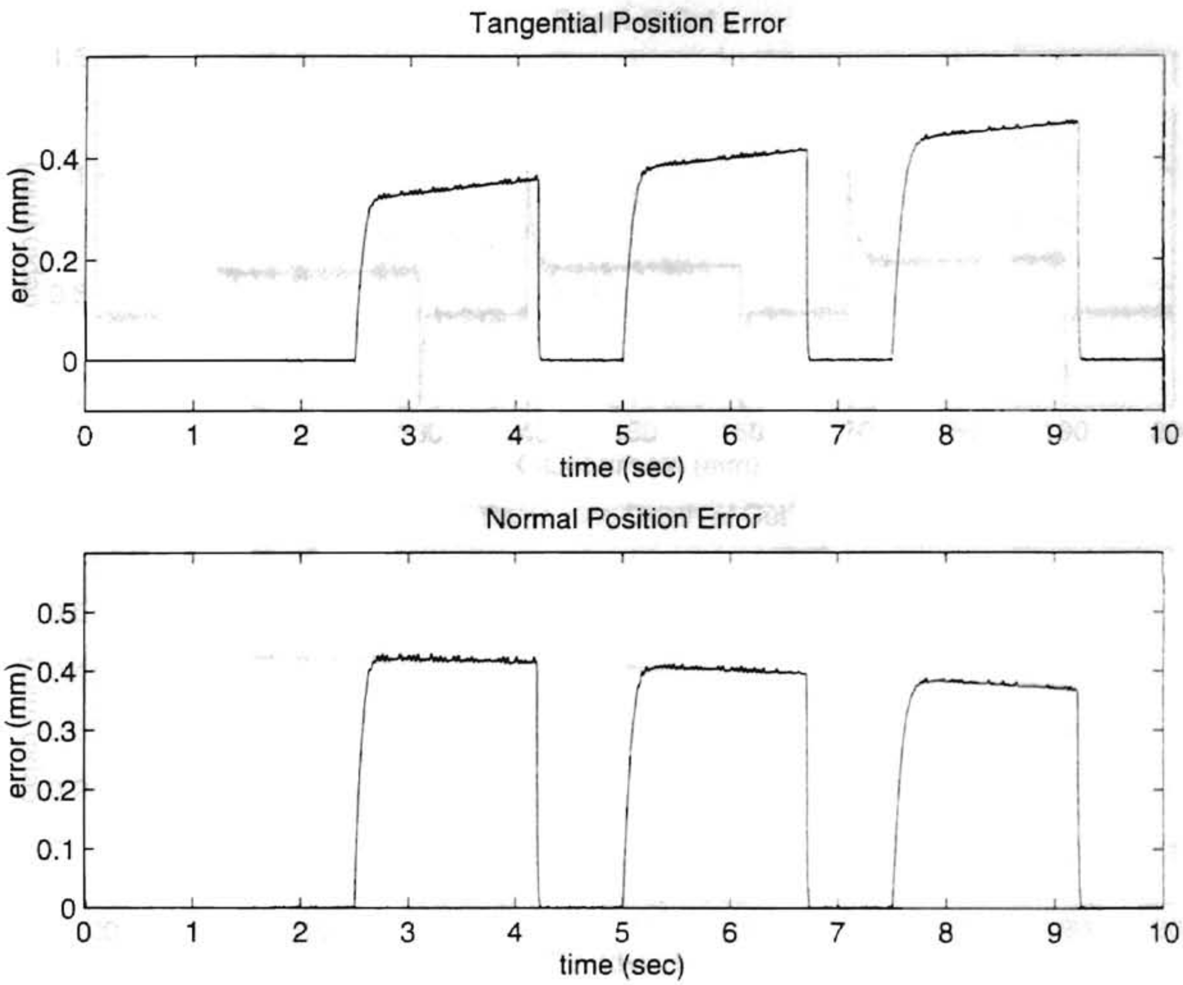

Figure 4.21 Results of Simulation 5 with Impedance Control: Position Errors

Large Upset Burrs with Desired Force Compensation

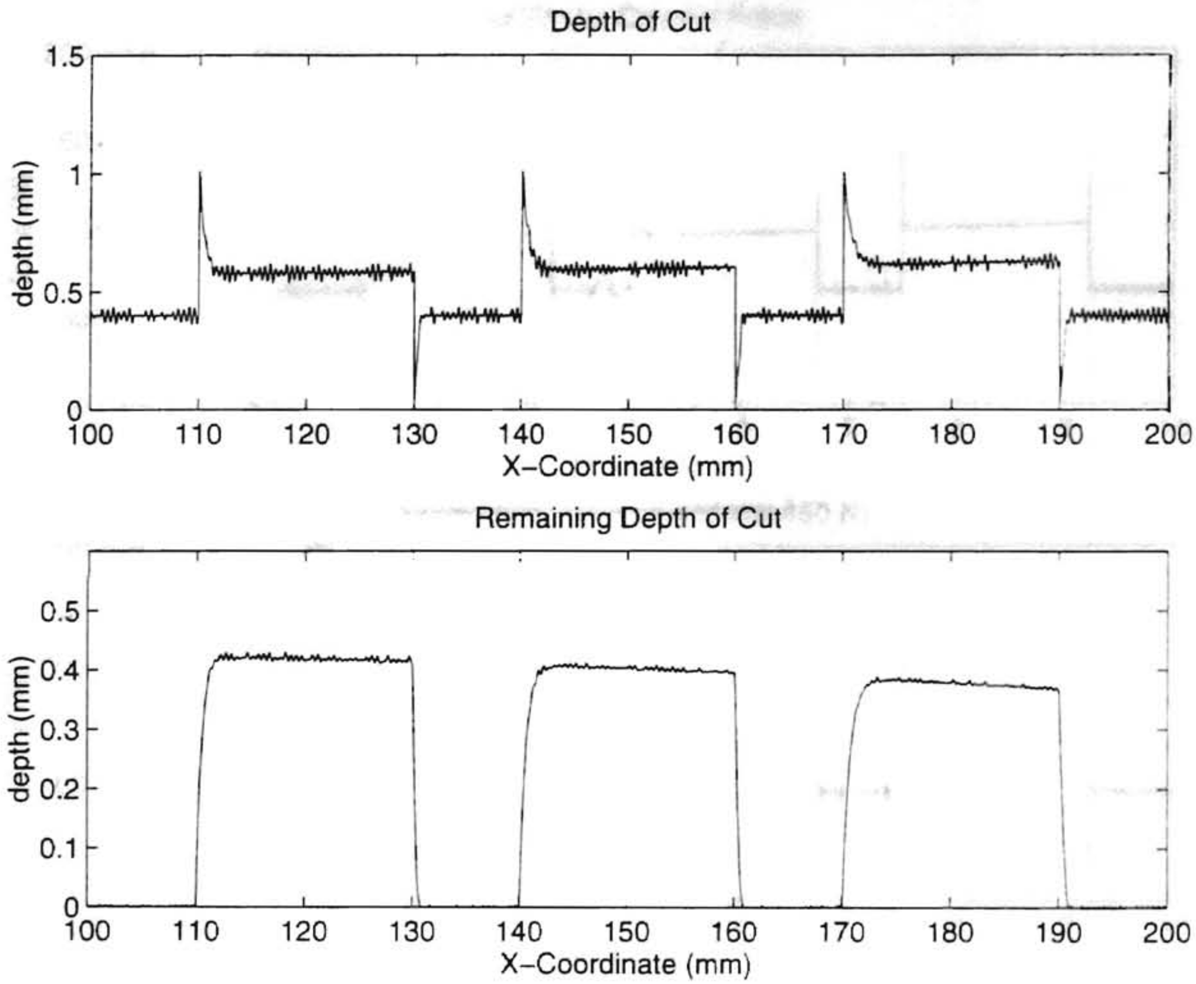

Figure 4.22 Results of Simulation 5 with Impedance Control: Depth of Cut and

Remaining Depth of Cut

Large Upset Burrs with Desired Force Compensation

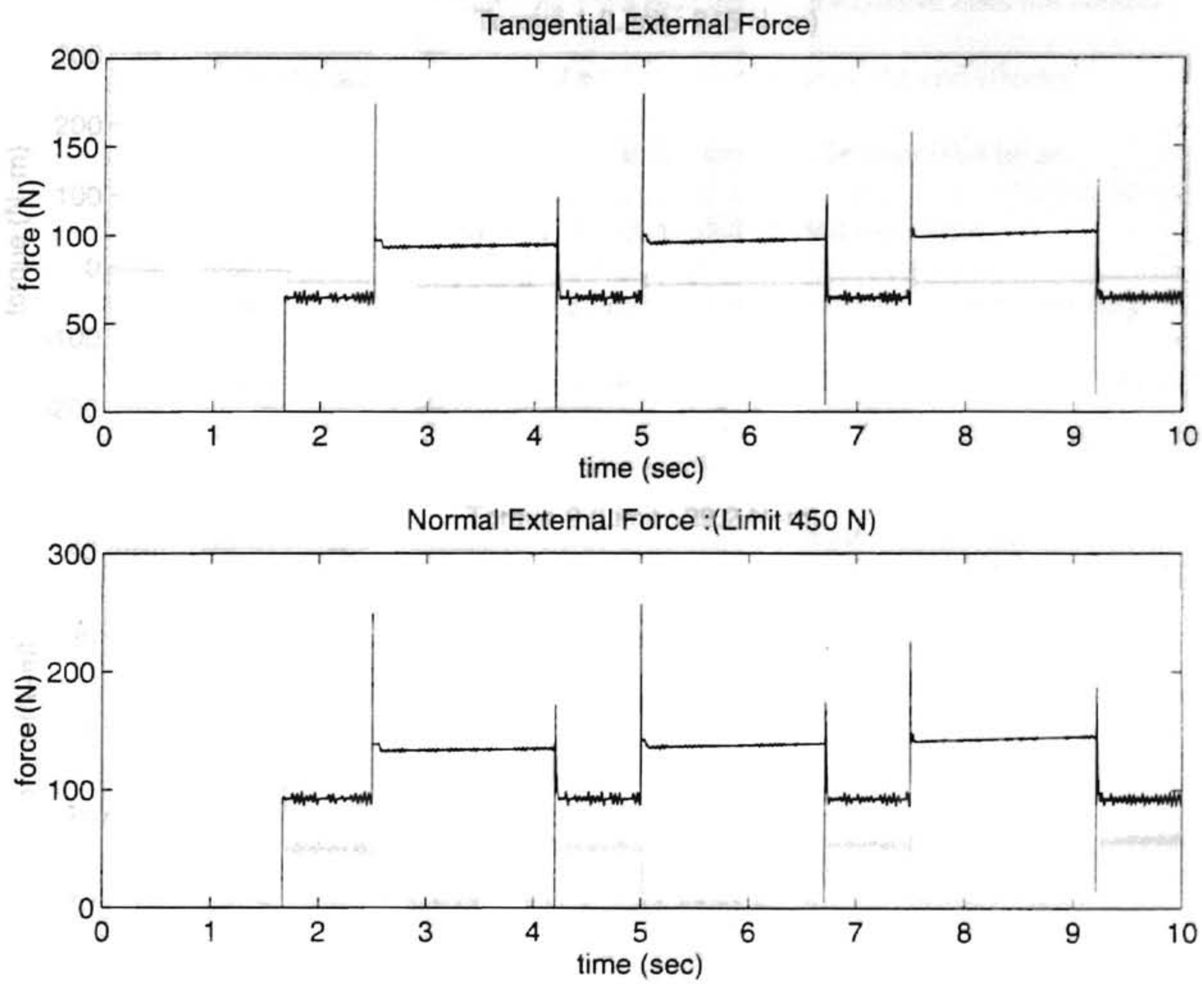

Figure 4.23 Results of Simulation 5 with Impedance Control: External Forces

Large Upset Burrs with Desired Force Compensation

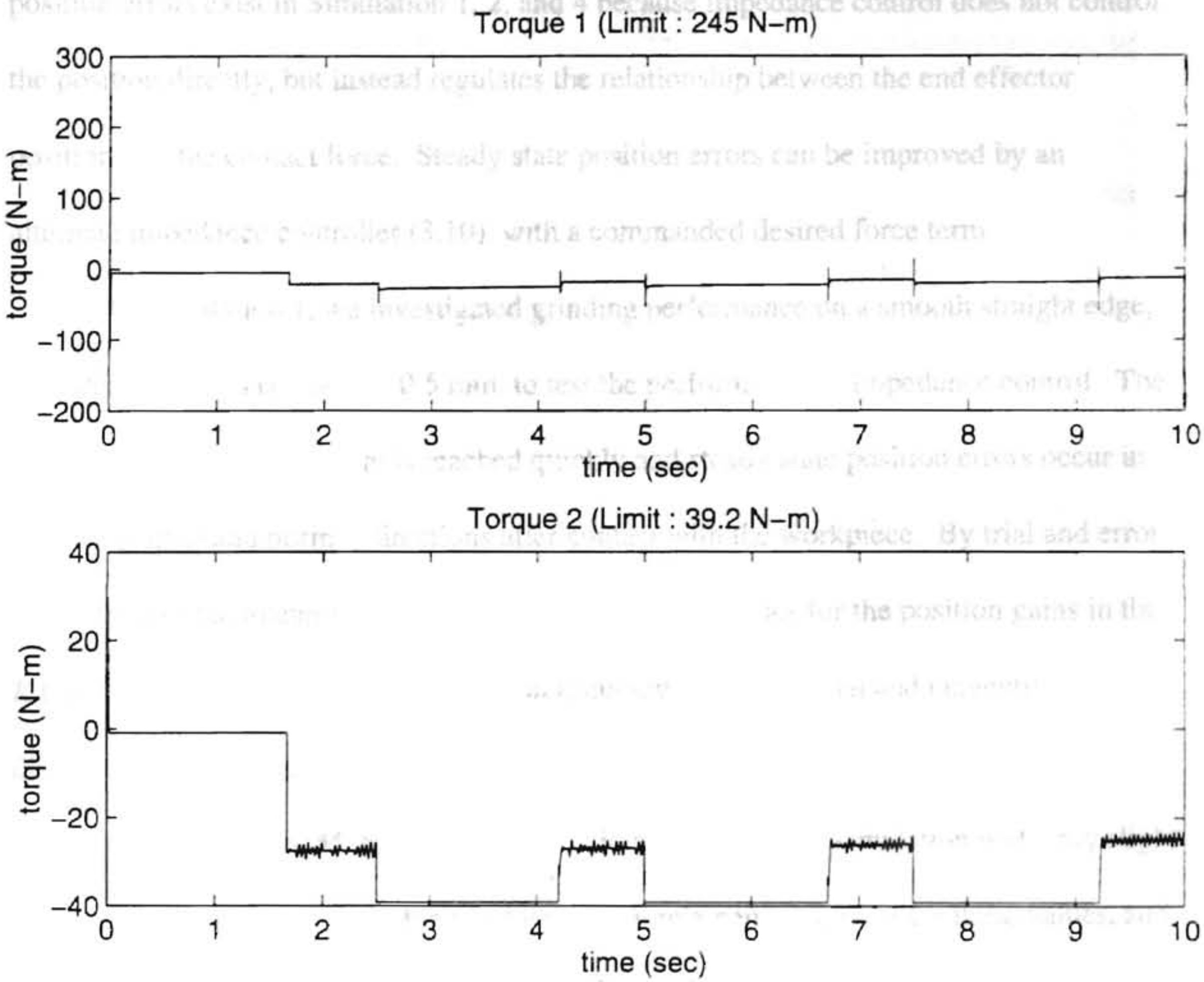

Figure 4.24 Results of Simulation 5 with Impedance Control: Motor Torques

Large Upset Burrs with Desired Force Compensation

Discussion and Analysis for Impedance Control

The results of Simulations 1-5 indicate that impedance control is able to achieve stable performance if the impedance parameter matrices are positive definite. Steady state can be reached quickly if impedance parameters are selected properly. Large steady state position errors exist in Simulation 1, 2, and 4 because impedance control does not control the position directly, but instead regulates the relationship between the end effector position and the contact force. Steady state position errors can be improved by an alternate impedance controller (3.10), with a commanded desired force term.

In Simulation 1, we investigated grinding performance on a smooth straight edge, with desired depth of cut $h_c = 0.5$ mm, to test the performance of impedance control. The results show that steady state is reached quickly and steady state position errors occur in both tangential and normal directions after contact with the workpiece. By trial and error, a set of target parameter matrices were selected. High values for the position gains in the K matrix were chosen to increase position accuracy in both normal and tangential directions. Position accuracy could be improved by increasing parameter values in matrices K and B, with M_d fixed, but this requires more time for simulation with only slight increases in the performance. Practical limits in implementation exist for these values, and attaining zero steady state error is not possible with finite values.

In Simulation 2, we investigated impedance control with random-height sinusoidal burrs on a straight edge. The results are similar to these in Simulation 1, except small irregular variations occur, caused by the contact force variations from random-height sinusoidal burrs. Our simulation results show that approximately 86 % of unwanted materials are removed by grinding, which is different from Hong's results [3] that show the end effector barely contacting the workpiece. We believe Hong's work is in error. In Simulation 3, an alternate impedance control (3.10) is employed to deburr the same surface as in Simulation 2. Simulation results, Figure 4.13-4.16, show that in contrast to results from Simulation 2, position errors remain close to zero, and external contact forces in steady state remain close to the commanded forces, namely those required to remove materials to reach the desired edge trajectory. These results indicate that if surface geometry is known and the needed grinding force F_d is modeled well, desired forces may be commanded to increase the performance of impedance control. However, in real operations, burrs are highly irregular, and it is difficult to model the desired grinding forces precisely.

In Simulations 4 and 5, we simulate impedance control in deburring an edge with large upset burrs illustrated in Figure 4.4. Simulation results show that the maximum depth of cut that can be reached by this robot for the ETG workpiece material is about 0.6 mm because the torque of motor 2 saturates. This torque limit also causes large position errors for large upset burrs. To improve position accuracy, either a larger torque motor or multiple passes of cut should be employed. An alternate impedance control can improve the performance of robotic deburring and grinding only when the motor torques do not saturate.

Compared to Hong's results [3], our results show significant improvement in steady state position error in the normal direction. Hong's results show large steady state errors in the normal direction that are approximately equal to the deviation of the average rough edge position from the desired normal position. This is probably caused by programming mistakes. Our simulation results show that 86 % or more of desired depth of cut can be reached by an impedance controller.

Based on these results, we conclude that an impedance controller provides a well-behaved controller for both free space and the constrained environment. It may be suitable for "rough" deburring and grinding operations or edge following tasks. If the surface geometry is known and desired grinding force F_d is modeled well, desired forces may be commanded to increase the performance of impedance control.

Simulations for Hybrid Impedance Control

The hybrid impedance control law of (3.17), (3.20), and (3.4), with position control in unconstrained space and in the tangential direction after contact, and force control in the normal direction after contact, is investigated in this section. The following simulation were employed:

Simulation 6: Smooth Straight Edge

- The desired workpiece trajectory was a straight edge starting from (0.1, 0.4) m to (0.2, 0.4) m in reference space.
- The "rough" surface was modeled by a smooth straight edge with a desired depth of cut h_c = 0.5 mm and the workpiece material was ETG.

- After some initial trials, impedance parameters for constrained space were chosen for Eq. (3.20) as $m_t = 5$kg, $b_t = 200$ N-s/m, $k_t = 30000$ N/m, $m_n = 100$ kg, $b_n = 50000$ N-s/m. For unconstrained space, the impedance matrices for Eq. (3.17) were selected as

$$M_d = \begin{bmatrix} 5 & 0 \\ 0 & 5 \end{bmatrix} \text{kg}, \;\; B = \begin{bmatrix} 2000 & 0 \\ 0 & 2000 \end{bmatrix} \text{N - s / m}, \;\; K = \begin{bmatrix} 30000 & 0 \\ 0 & 30000 \end{bmatrix} \text{N / m}$$

- Simulation results showing position errors, depth of cut and remaining depth of cut, external forces, position history, and motor torques are given in Figures 4.25-4.29.

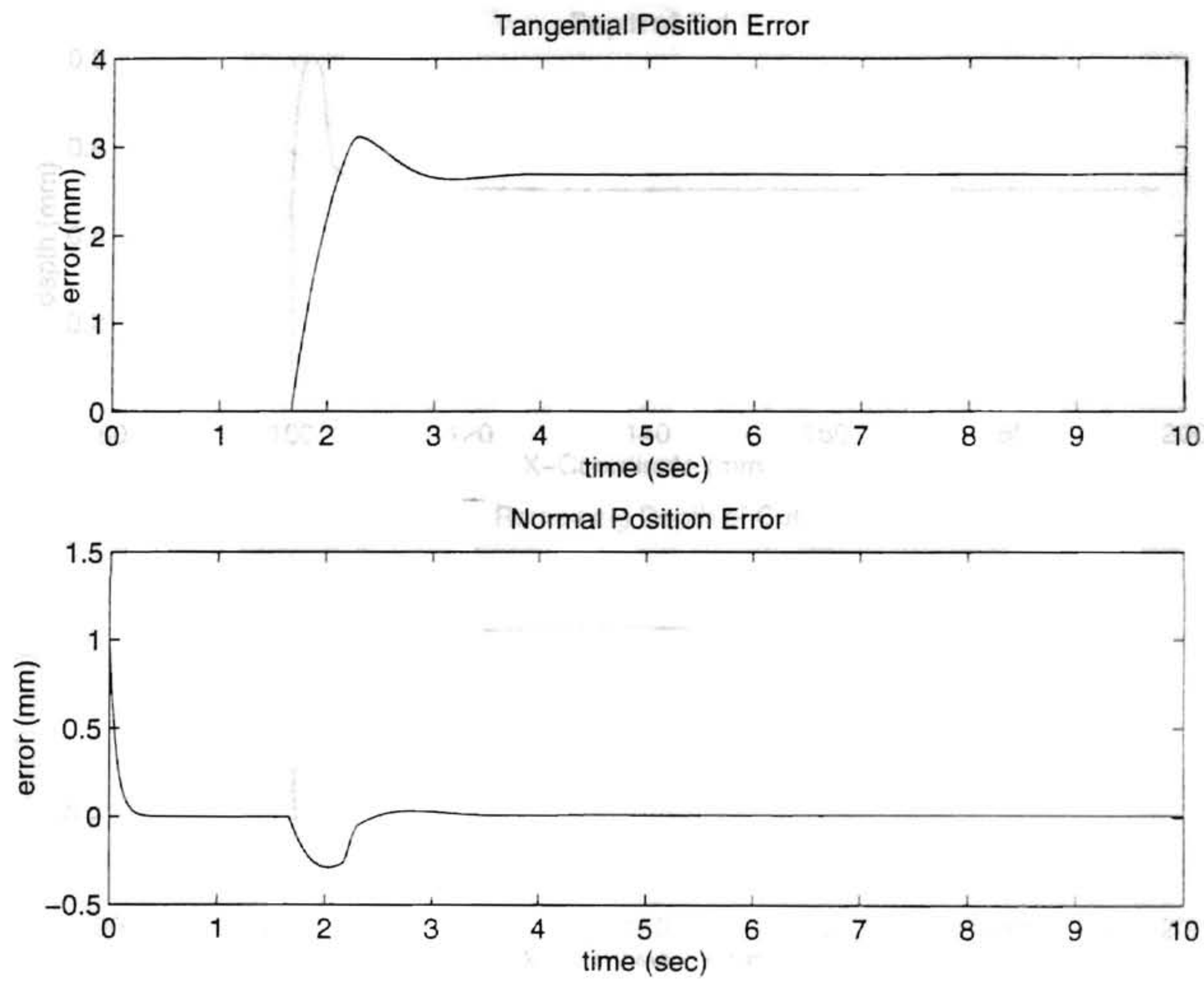

Figure 4.25 Results of Simulation 6 with Hybrid Impedance Control: Position Errors

Smooth Straight Edge

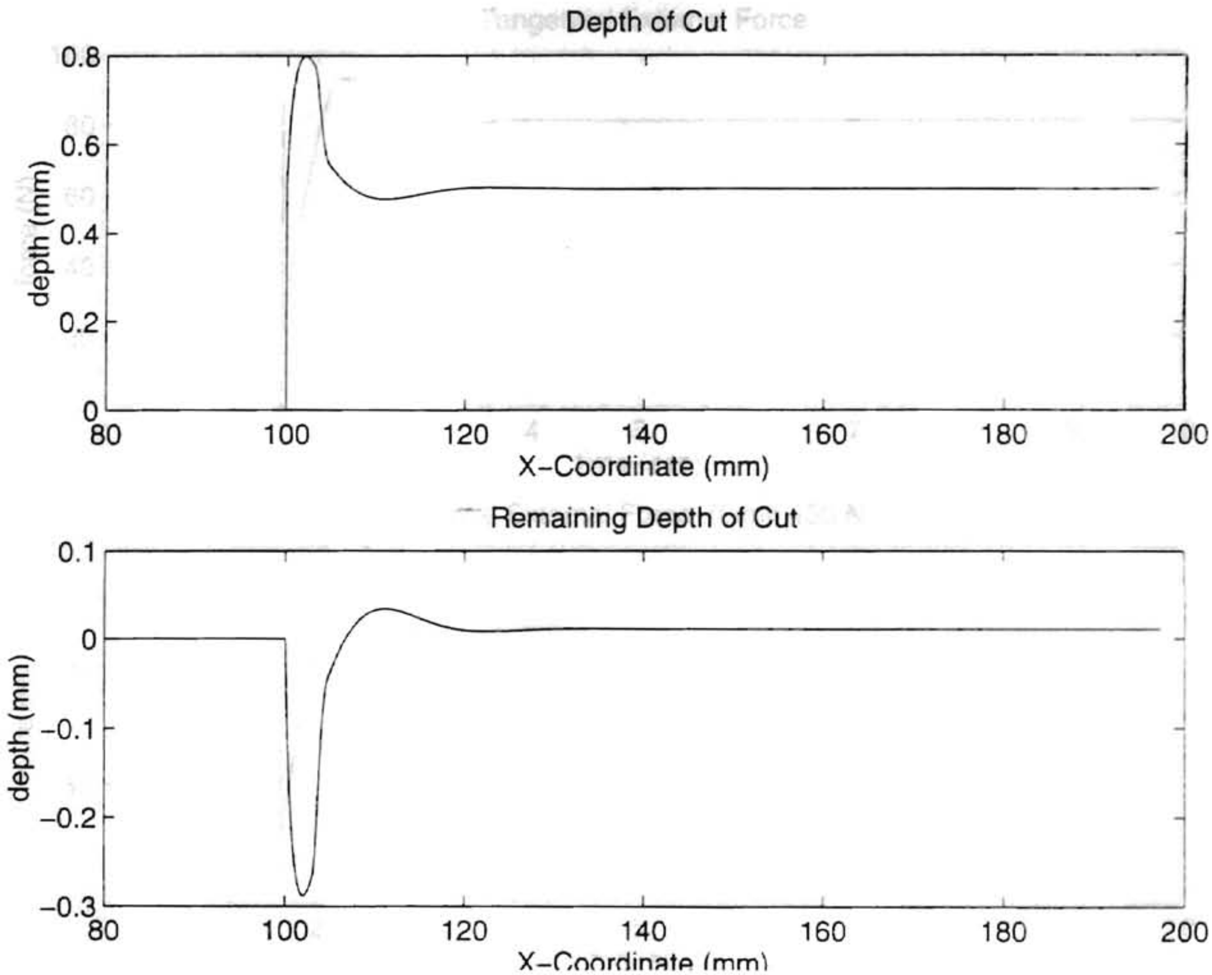

Figure 4.26 Results of Simulation 6 with Hybrid Impedance Control:

Depth of Cut and Remaining Depth of Cut

Smooth Straight Edge

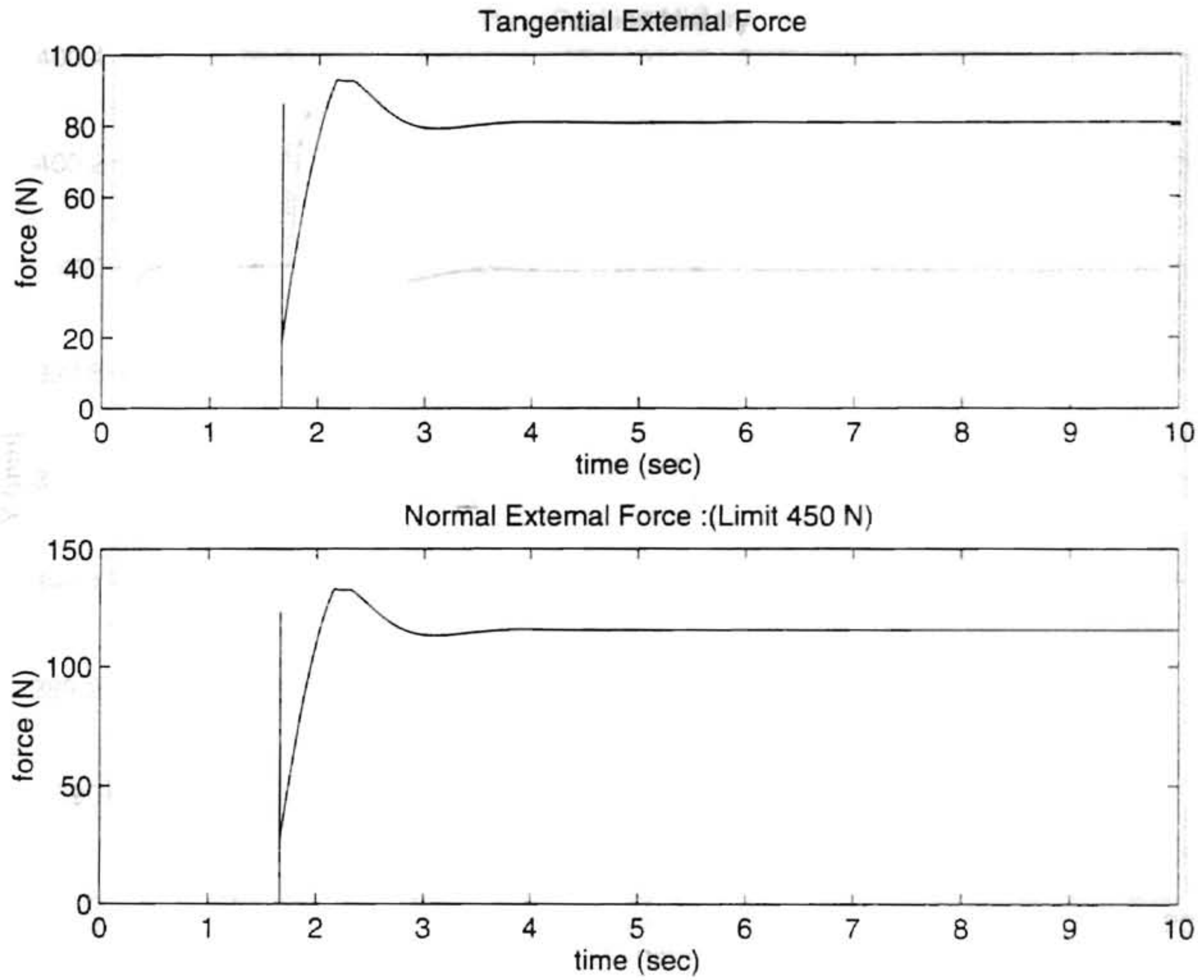

Figure 4.27 Results of Simulation 6 with Hybrid Impedance Control: External Forces

Smooth Straight Edge

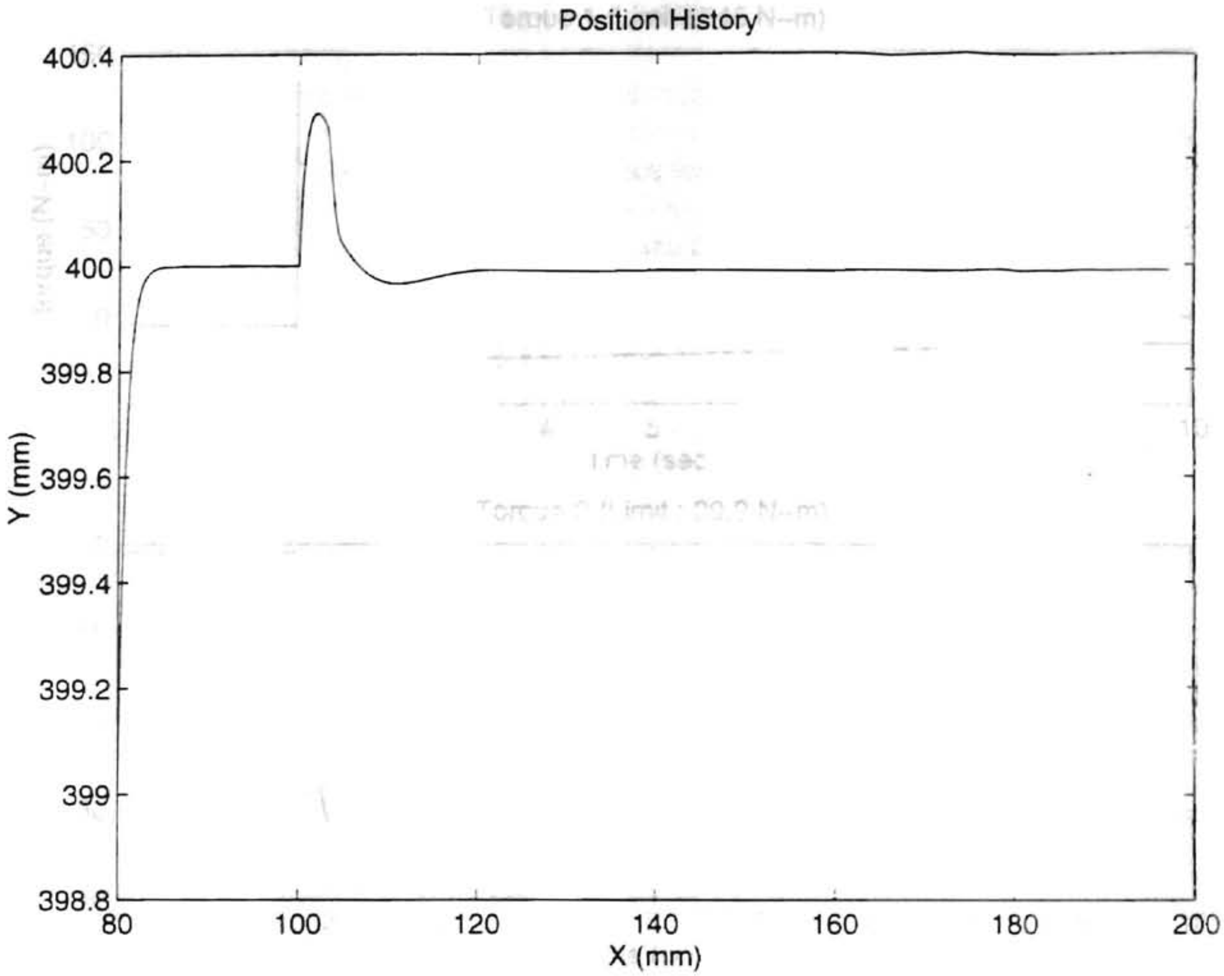

Figure 4.28 Results of Simulation 6 with Hybrid Impedance Control: Position History

Smooth Straight Edge

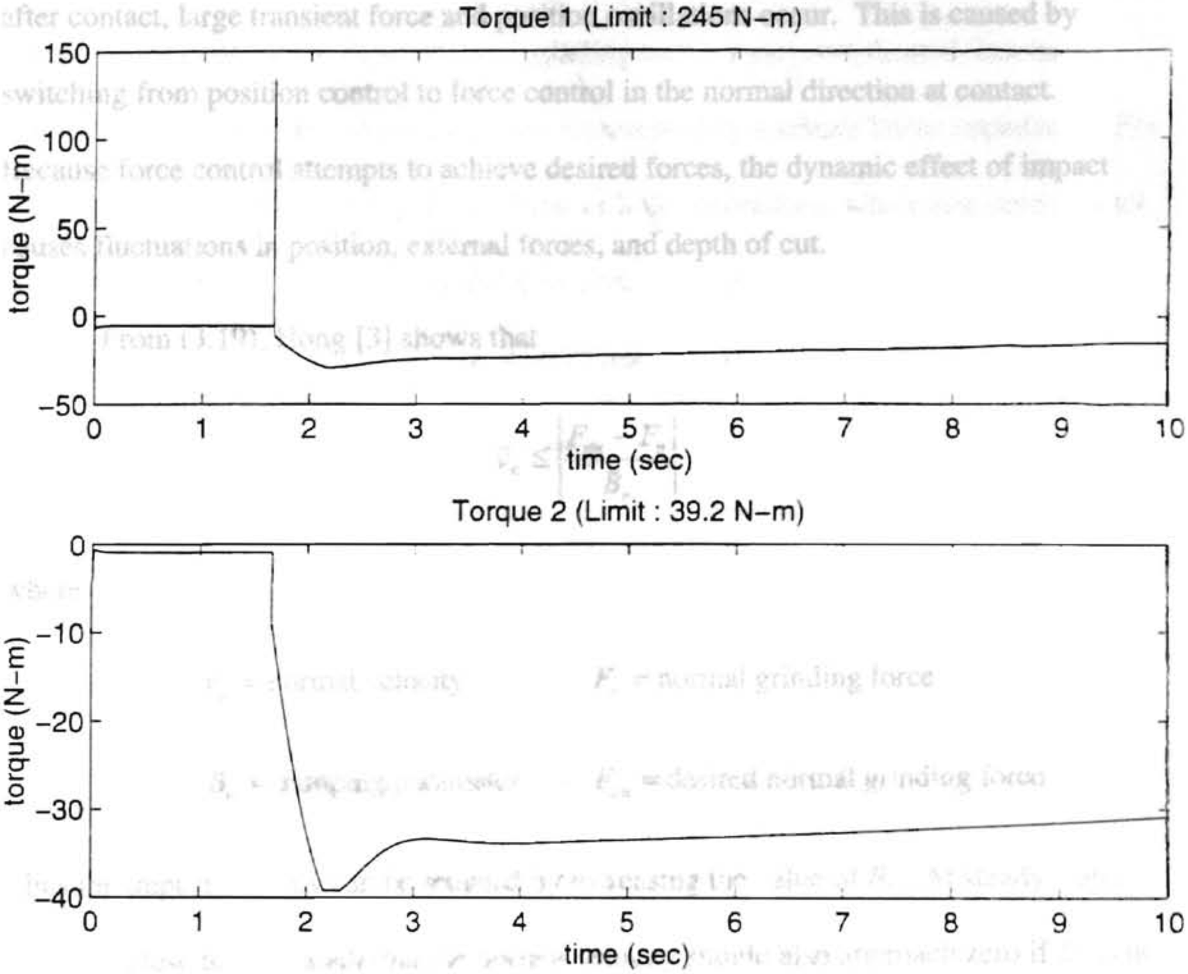

Figure 4.29 Results of Simulation 6 with Hybrid Impedance Control: Motor Torques

Smooth Straight Edge

Discussion and Analysis for Hybrid Impedance Control

After some trial simulations, we were able to obtain results showing small oscillation and steady state position errors, as illustrated in Figures 4.25-4.29. From simulation results, we found that zero steady state could be reached before contact, but after contact, large transient force and position oscillations occur. This is caused by switching from position control to force control in the normal direction at contact. Because force control attempts to achieve desired forces, the dynamic effect of impact causes fluctuations in position, external forces, and depth of cut.

From (3.19), Hong [3] shows that

$$v_n \le \left| \frac{F_{dn} - F_n}{B_n} \right|$$

where

v_n = normal velocity $\qquad$ F_n = normal grinding force

B_n = damping parameter $\qquad$ F_{dn} = desired normal grinding force

Thus the impact velocity can be reduced by increasing the value of B_n. At steady state, F_{dn}-F_n is close to zero, such that the normal velocity should also approach zero if B_n is not small. Increasing the values of m_t, b_t, and k_t improves motion tracking in the tangential direction, which is why large values were selected for the position control in the tangential direction. However, position control in the tangential direction will be degraded by the force control in the normal direction, because the force control adjusts position in the normal direction to control the normal force.

To implement hybrid impedance control in robotic deburring and grinding is difficult, because including desired forces requires a known surface geometry and accurate grinding force modeling. Displacement in the normal direction is adjusted indirectly by force control, such that large position errors may occur with this approach. Moreover the force environment for the deburring and grinding task is more complicated than mere contact or loss of contact, which cannot be represented by a simple linear impedance. For simple tasks such as edge-following or "peg-in-hole" operations, where non-zero contact force exists in the normal direction and zero contact force is assumed in the tangential direction, a hybrid impedance control strategy may be suitable. We conclude, however, that it is unsuitable for deburring and grinding.

Simulations for Switching Control

In this section, we employ simulations using different materials and rough edges to investigate the performance of our proposed new switching control. Results for this control, as described by (3.4), (3.21), and (3.25), are presented for the following simulations:

Simulation 7: Random-Height Sinusoidal Burrs, ETG Workpiece

- The desired workpiece trajectory was a straight edge, from (0.1, 0.4) m to (0.2, 0.4) m in reference space.

- The rough surface is modeled by sinusoidal burrs with average burr height $h_a = 0.05$ mm and burr frequency $f_b = 2$ burrs/mm. The nominal desired depth of cut h_c is 0.5 mm, and the material is ETG.

- After some initial trials to tune the controller, the proportional and derivative gain matrices were chosen for position control (3.21) as:

$$K_p = \begin{bmatrix} 900 & 0 \\ 0 & 900 \end{bmatrix} \frac{1}{s^2}, \qquad K_d = \begin{bmatrix} 60 & 0 \\ 0 & 60 \end{bmatrix} \frac{1}{s}$$

  Similarly, the proportional and integral gain matrices for force control (3.25) were chosen as:

$$K_f = \begin{bmatrix} 0.005 & 0 \\ 0 & 0.005 \end{bmatrix} \frac{1}{s^2} \cdot \frac{m}{N}, \qquad K_{fi} = \begin{bmatrix} 0.00006 & 0 \\ 0 & 0.00006 \end{bmatrix} \frac{1}{s^3} \cdot \frac{m}{N}$$

- Simulation results showing position errors, external forces, and motor torques are given in Figures 4.30-4.32.

<u>Simulation 8: Random-Height Sinusoidal Burrs, DTG Workpiece</u>

- The same simulation conditions as in Simulation 7 were used, except the workpiece material was changed to DTG.

- Simulation results showing position errors, external forces, and motor torques are given in Figures 4.33-4.35.

Simulation 9: Random-Height Sinusoidal Burrs, DTG Workpiece, No Torque Limits

- The same simulation conditions as in Simulation 8 were used, except torque limits on the motors were removed.
- Simulation results showing position errors, depth of cut and remaining depth of cut, external forces, and motor torques are given in Figures 4.36-4.39.

Simulation 10: Large Upset Burrs, ETG Workpiece

- The same simulation conditions as in Simulation 7 were used, except the rough surface was modeled as large upset burrs, as in Figure 4.4.
- Simulation results showing position errors, depth of cut and remaining depth of cut, external forces, and motor torques are given in Figures 4.40-4.43.

Simulation 11: Large Upset Burrs, ETG Workpiece, No Torque Limits

- The same simulation conditions as in Simulation 10 were used, except torque limits on the motors were removed.
- Simulation results showing position errors, depth of cut and remaining depth of cut, external forces, and motor torques are given in Figures 4.44-4.47.

Simulation 12: Large Upset Burrs, DTG Workpiece, No Torque Limits

- The same simulation conditions as in Simulation 11 were used, except the workpiece was changed to DTG material.
- Simulation results showing position errors, depth of cut and remaining depth of cut, external forces, and motor torques are given in Figures 4.48-4.51.

Simulation 13: Scallop Burrs, ETG Workpiece

- The same simulation conditions as in Simulation 7 were used, except the rough surface was modeled by scallop burrs, as illustrated in Figure 4.5.
- Simulation results showing position errors, depth of cut and remaining depth of cut, external forces, and motor torques are given in Figures 4.52-4.55.

Simulation 14: Scallop Burrs, DTG Workpiece, No Torque Limits

- The same simulation conditions as in Simulation 13 were used, except the workpiece was changed to DTG material and torque limits on the motors were removed.
- Simulation results showing position errors, depth of cut and remaining depth of cut, external forces, position history, and motor torques are given in Figures 4.56-4.59.

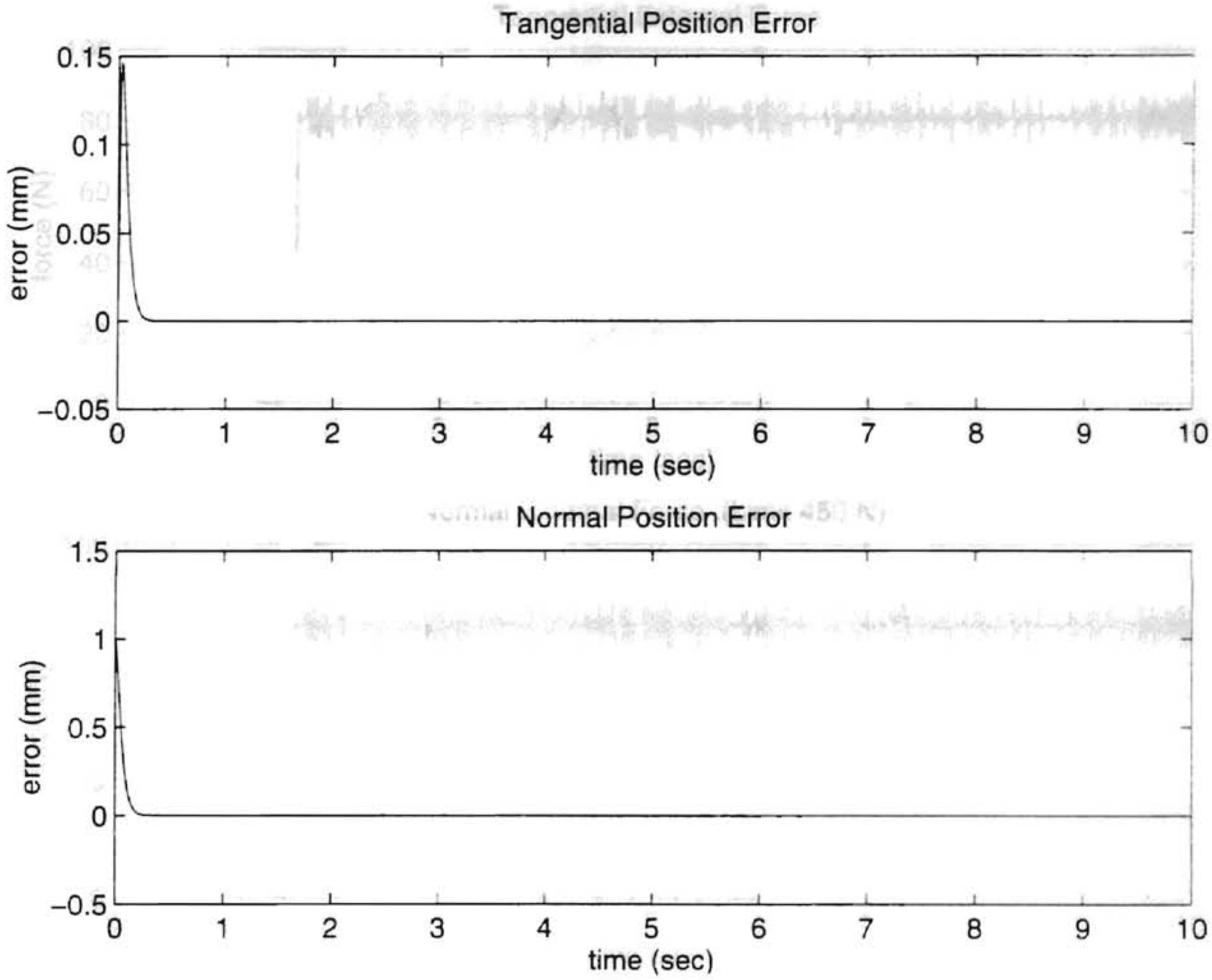

Figure 4.30 Results of Simulation 7 with Switching Control: Position Errors

Random-Height Sinusoidal Burrs, ETG Workpiece

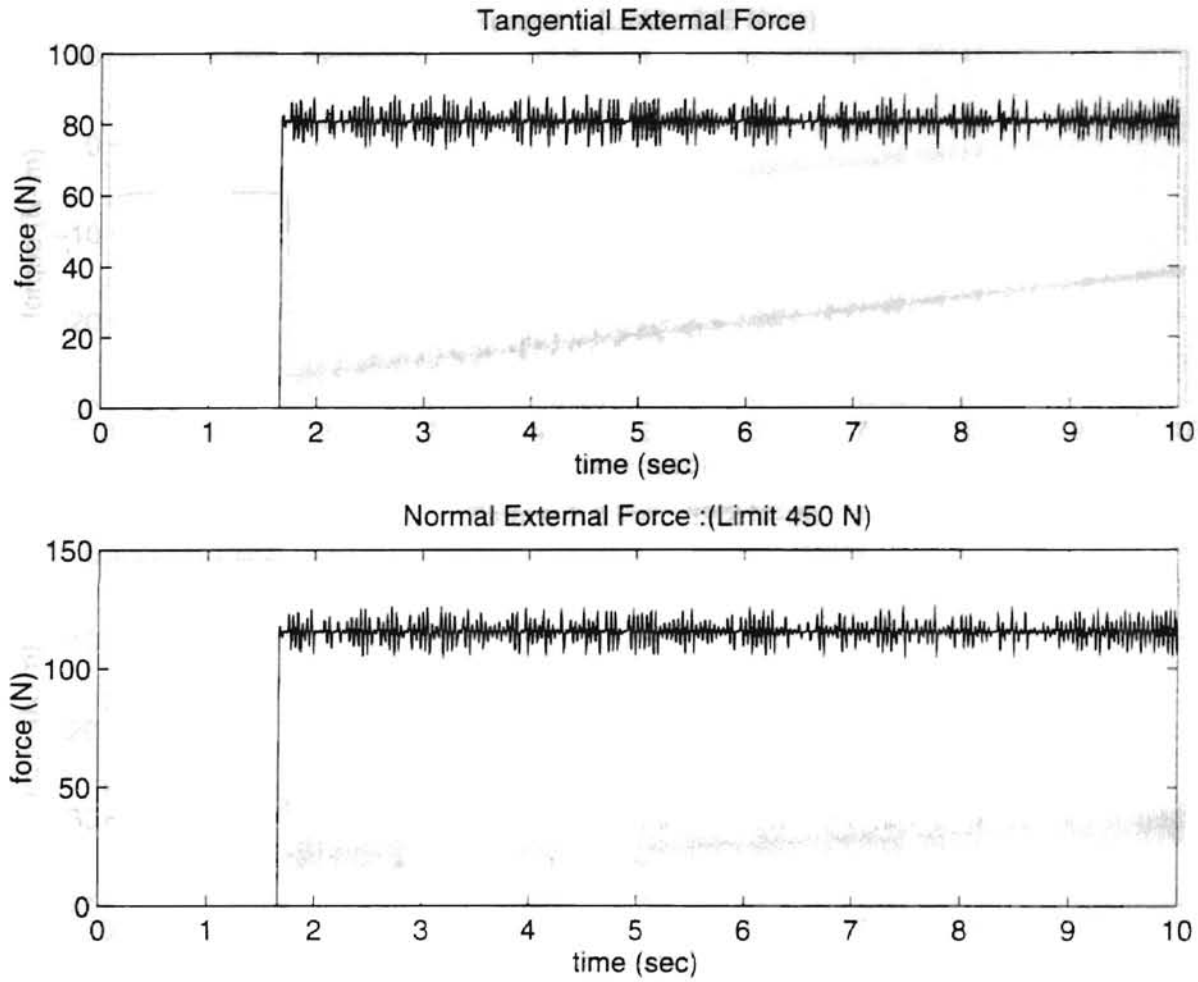

Figure 4.31 Results of Simulation 7 with Switching Control: External Forces

Random-Height Sinusoidal Burrs, ETG Workpiece

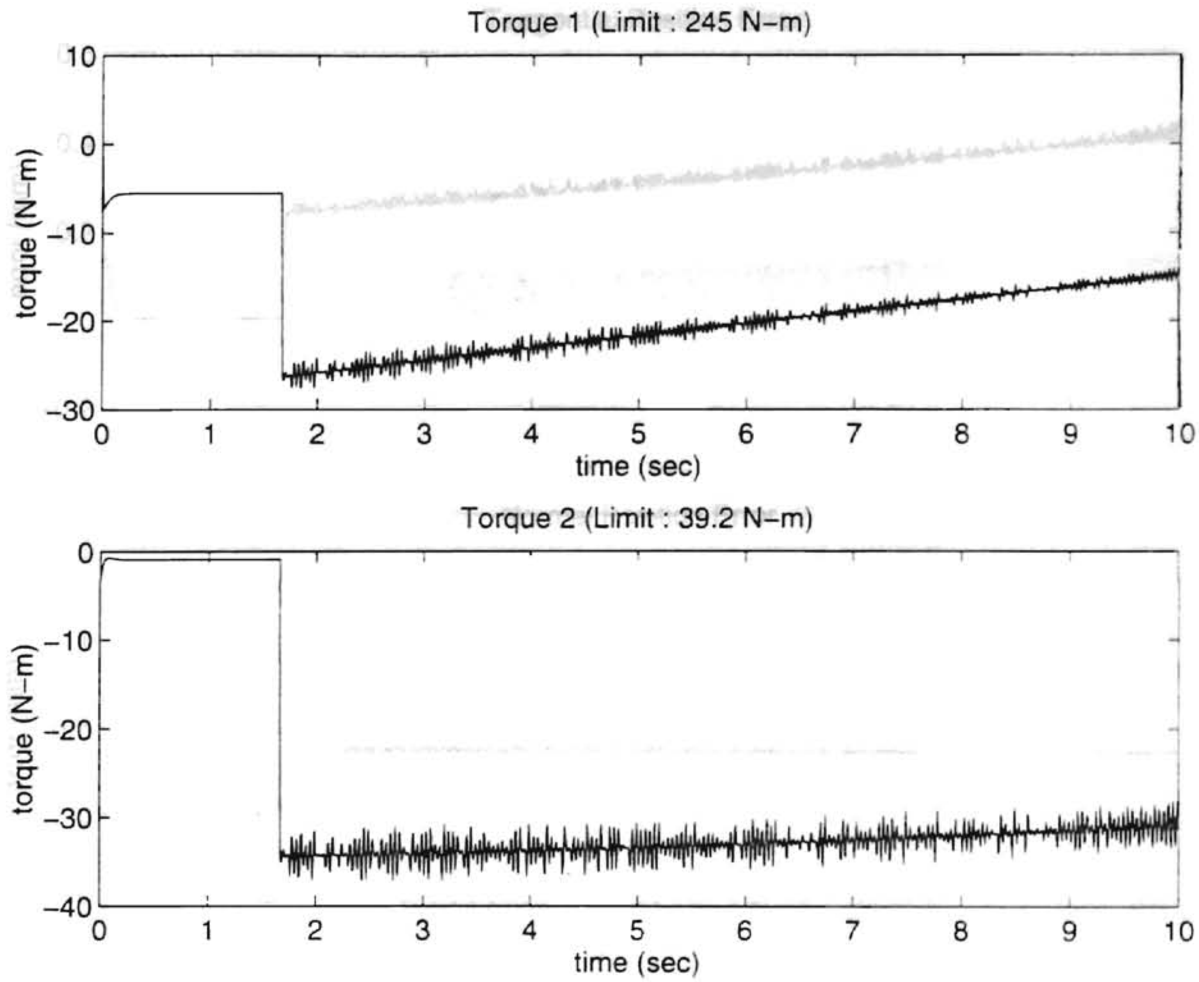

Figure 4.32 Results of Simulation 7 with Switching Control: Motor Torques

Random-Height Sinusoidal Burrs, ETG Workpiece

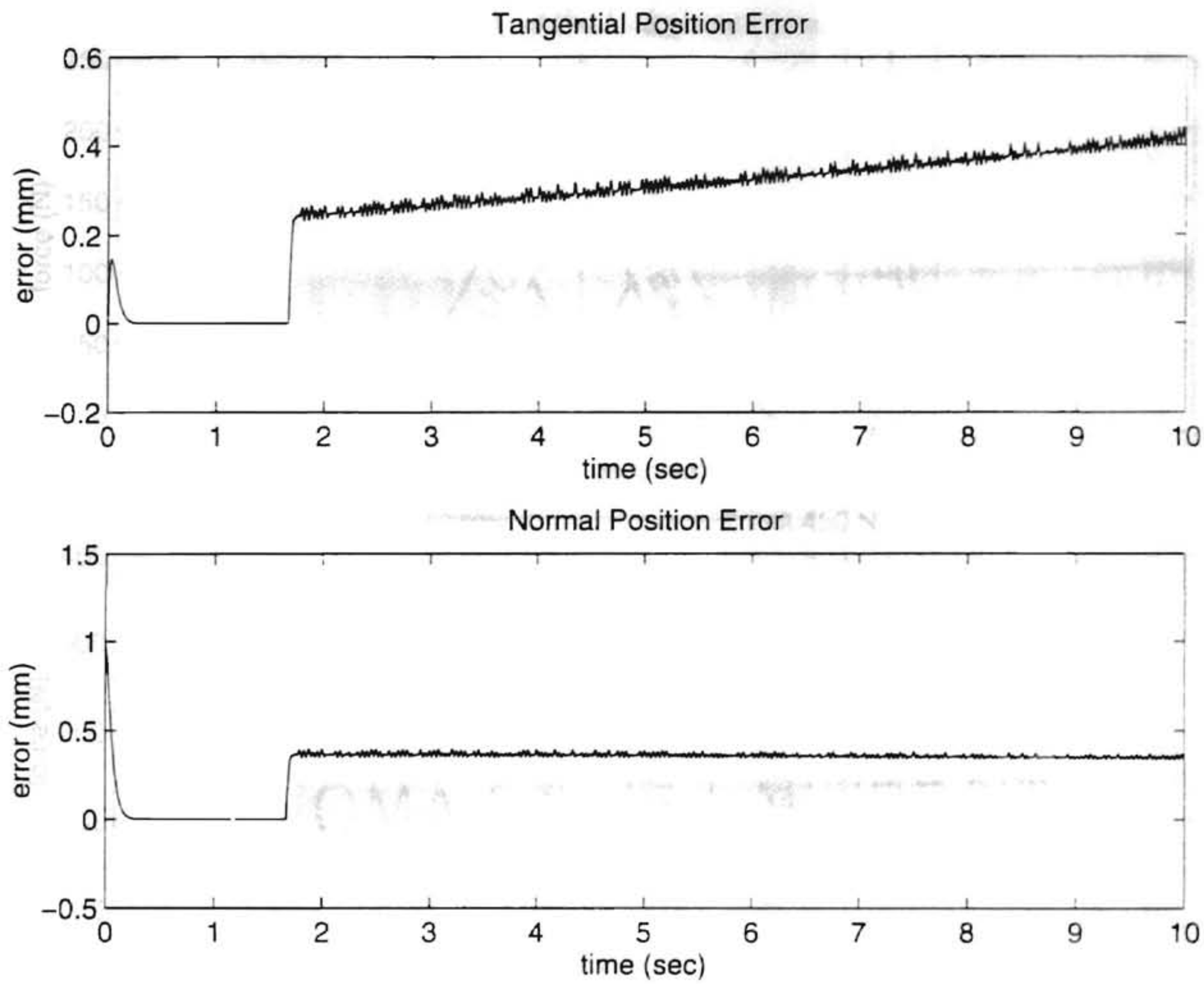

Figure 4.33 Results of Simulation 8 with Switching Control: Position Errors

Random-Height Sinusoidal Burrs, DTG Workpiece

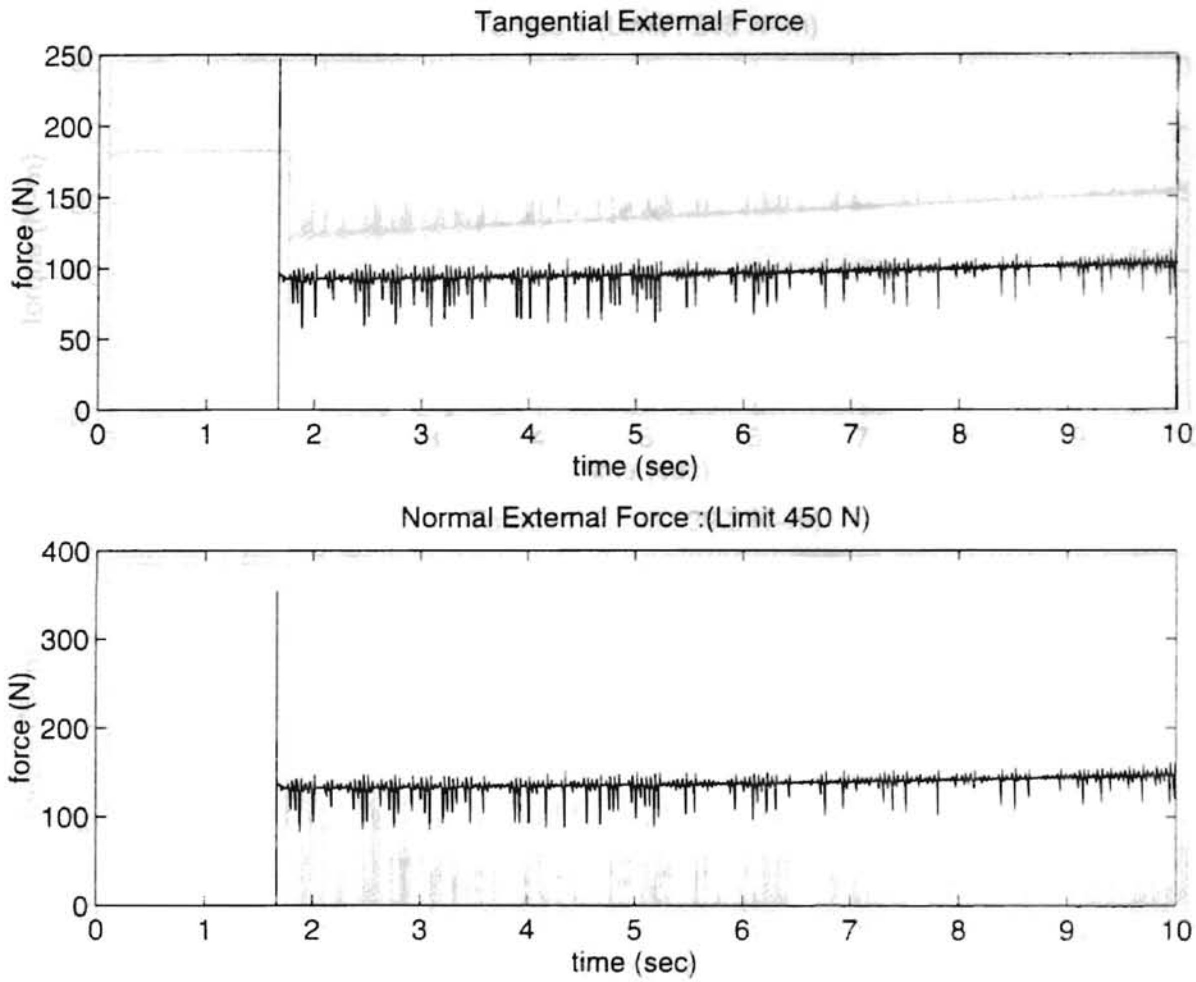

Figure 4.34 Results of Simulation 8 with Switching Control: External Forces

Random-Height Sinusoidal Burrs, DTG Workpiece

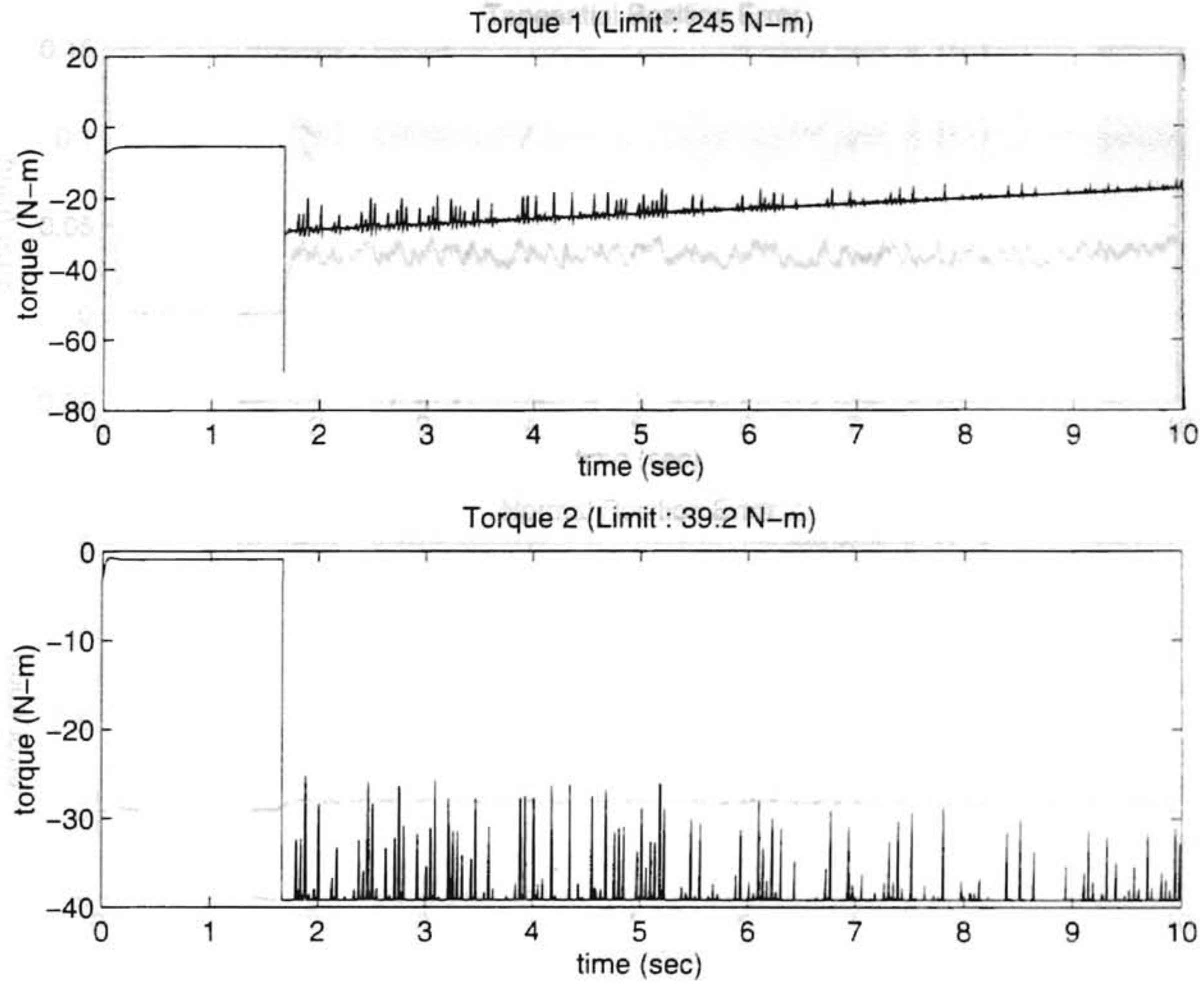

Figure 4.35 Results of Simulation 8 with Switching Control: Motor Torques

Random-Height Sinusoidal Burrs, DTG Workpiece

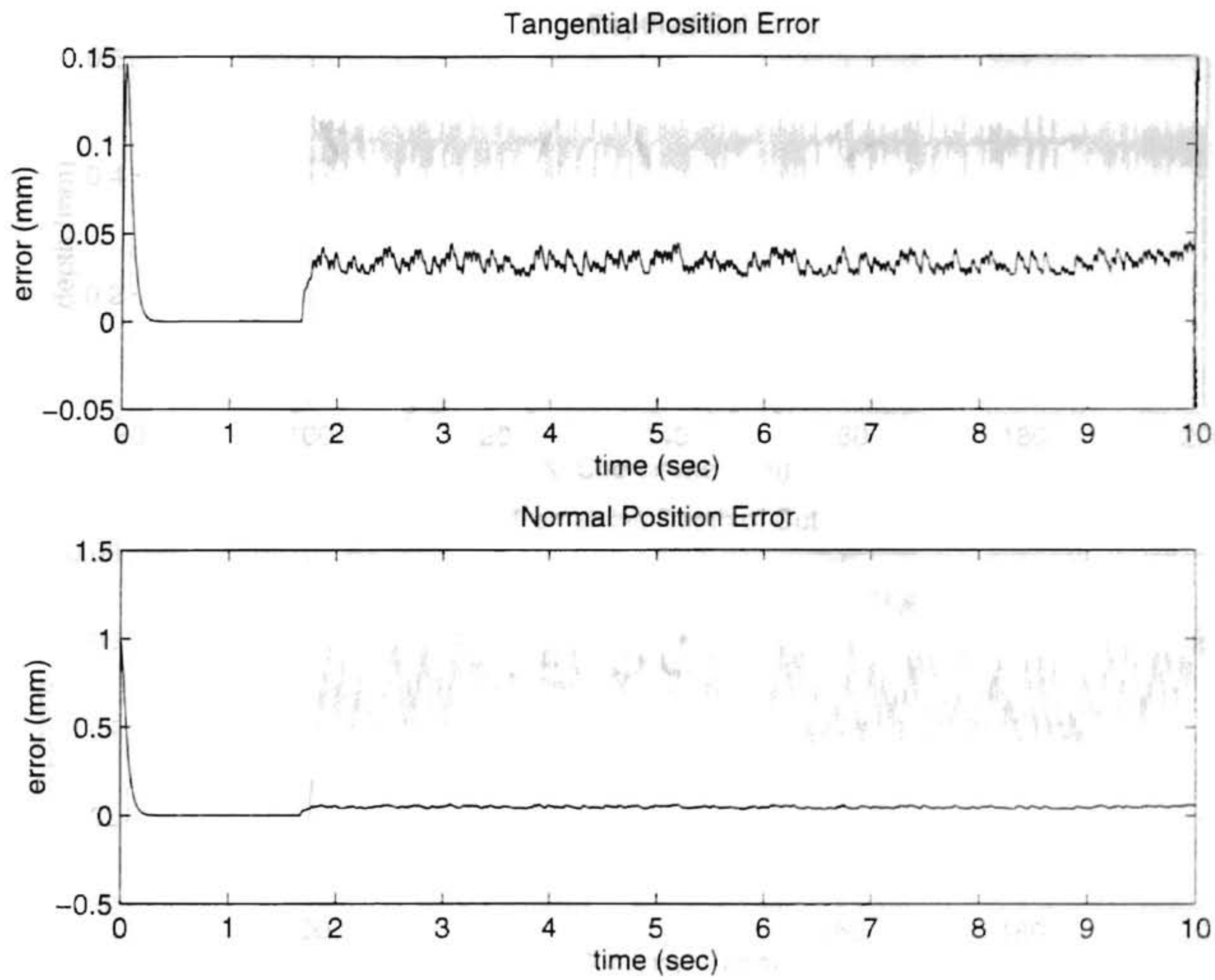

Figure 4.36 Results of Simulation 9 with Switching Control: Position Errors

Random-Height Sinusoidal Burrs, DTG Workpiece, No Torque Limits

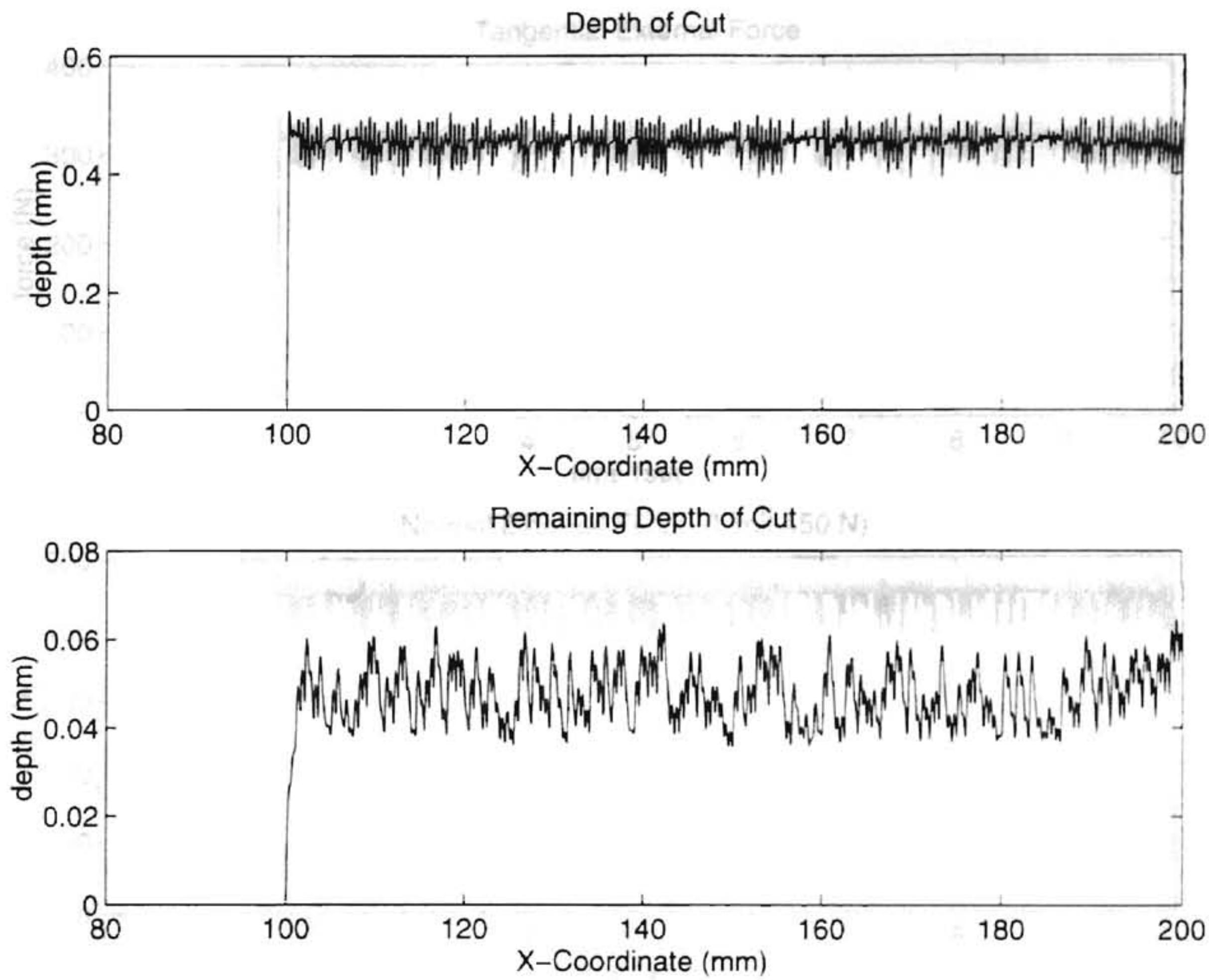

Figure 4.37 Results of Simulation 9 with Switching Control: Depth of Cut and Remaining Depth of Cut

Random-Height Sinusoidal Burrs, DTG Workpiece, No Torque Limits

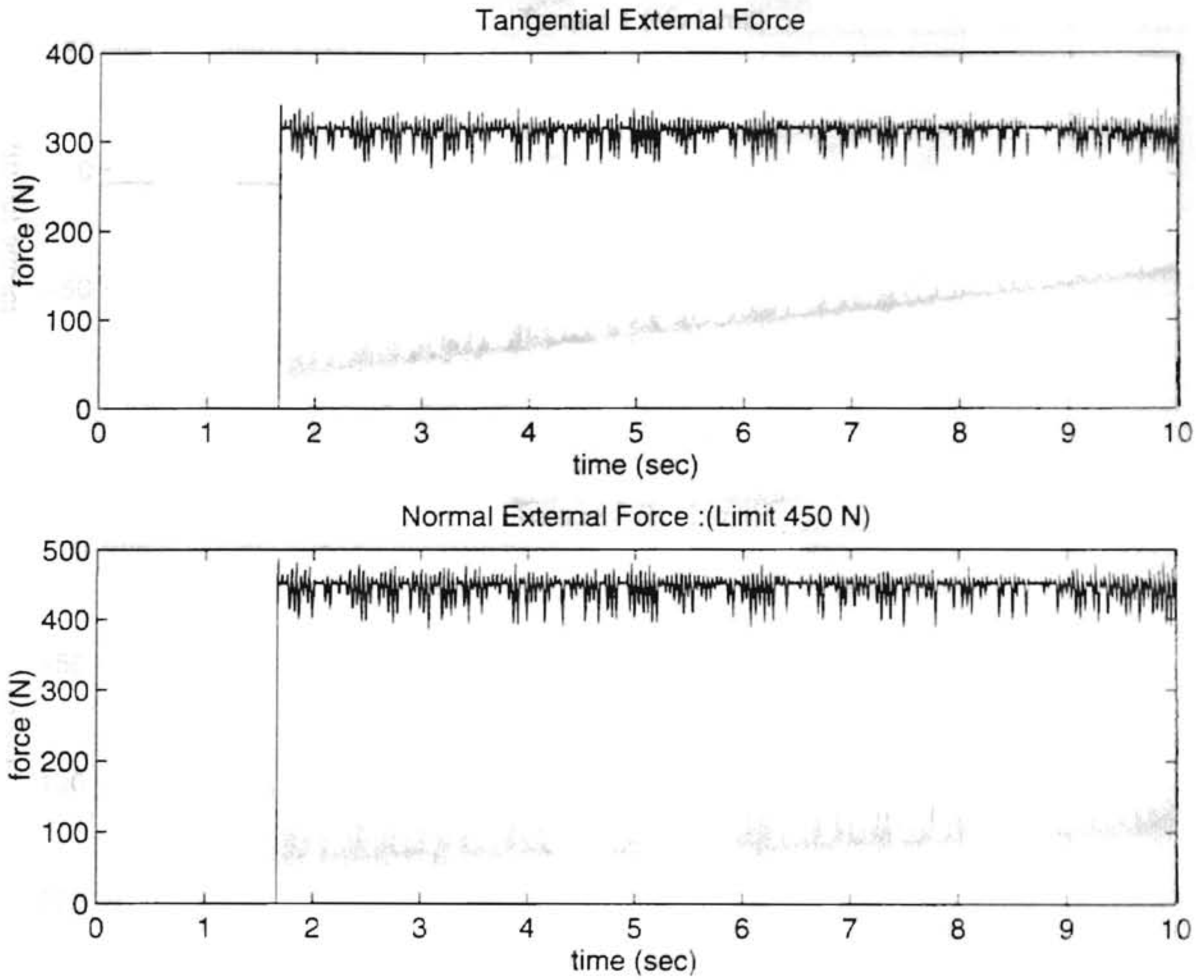

Figure 4.38 Results of Simulation 9 with Switching Control: External Forces

Random-Height Sinusoidal Burrs, DTG Workpiece, No Torque Limits

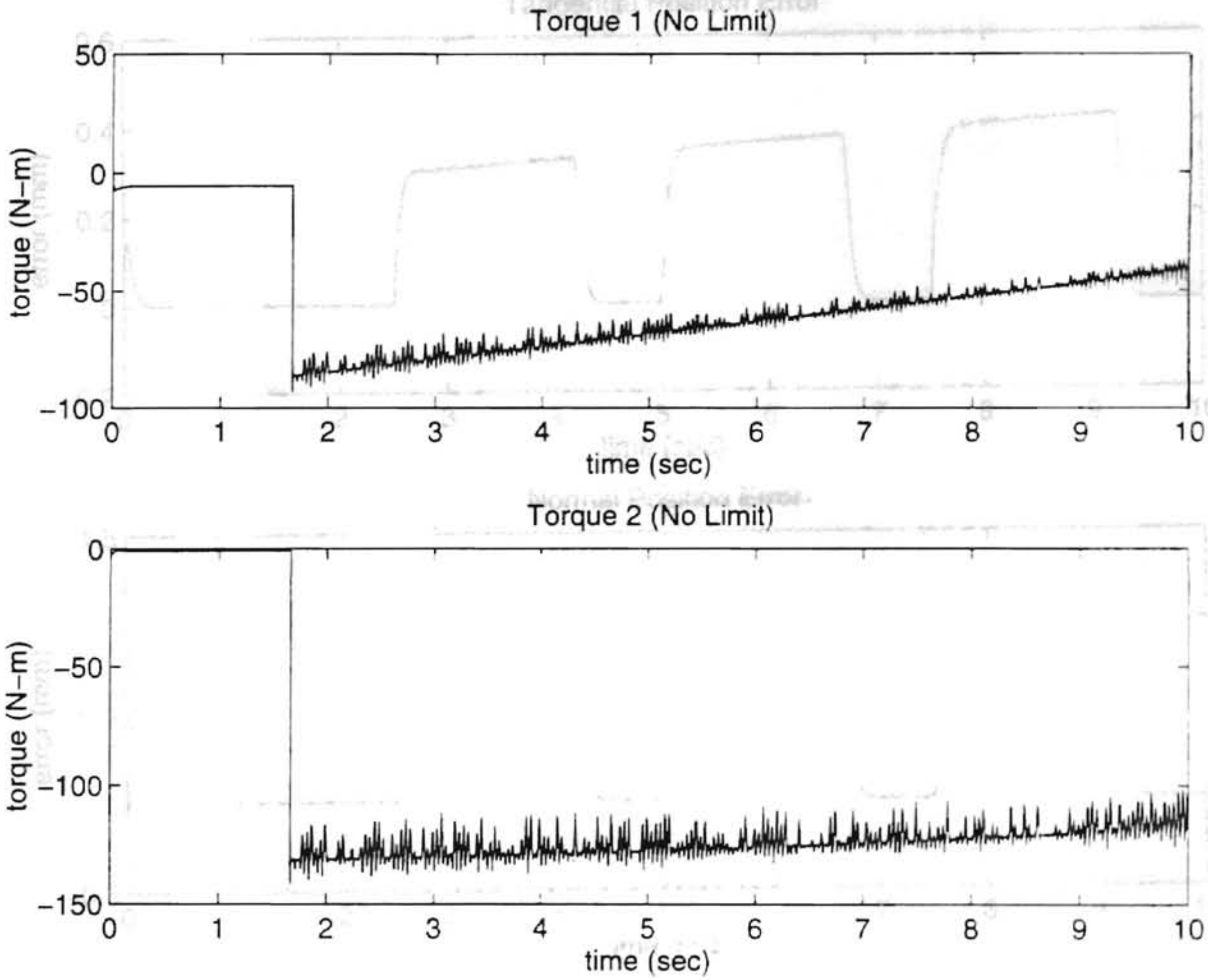

Figure 4.39 Results of Simulation 9 with Switching Control: Motor Torques

Random-Height Sinusoidal Burrs, DTG Workpiece, No Torque Limits

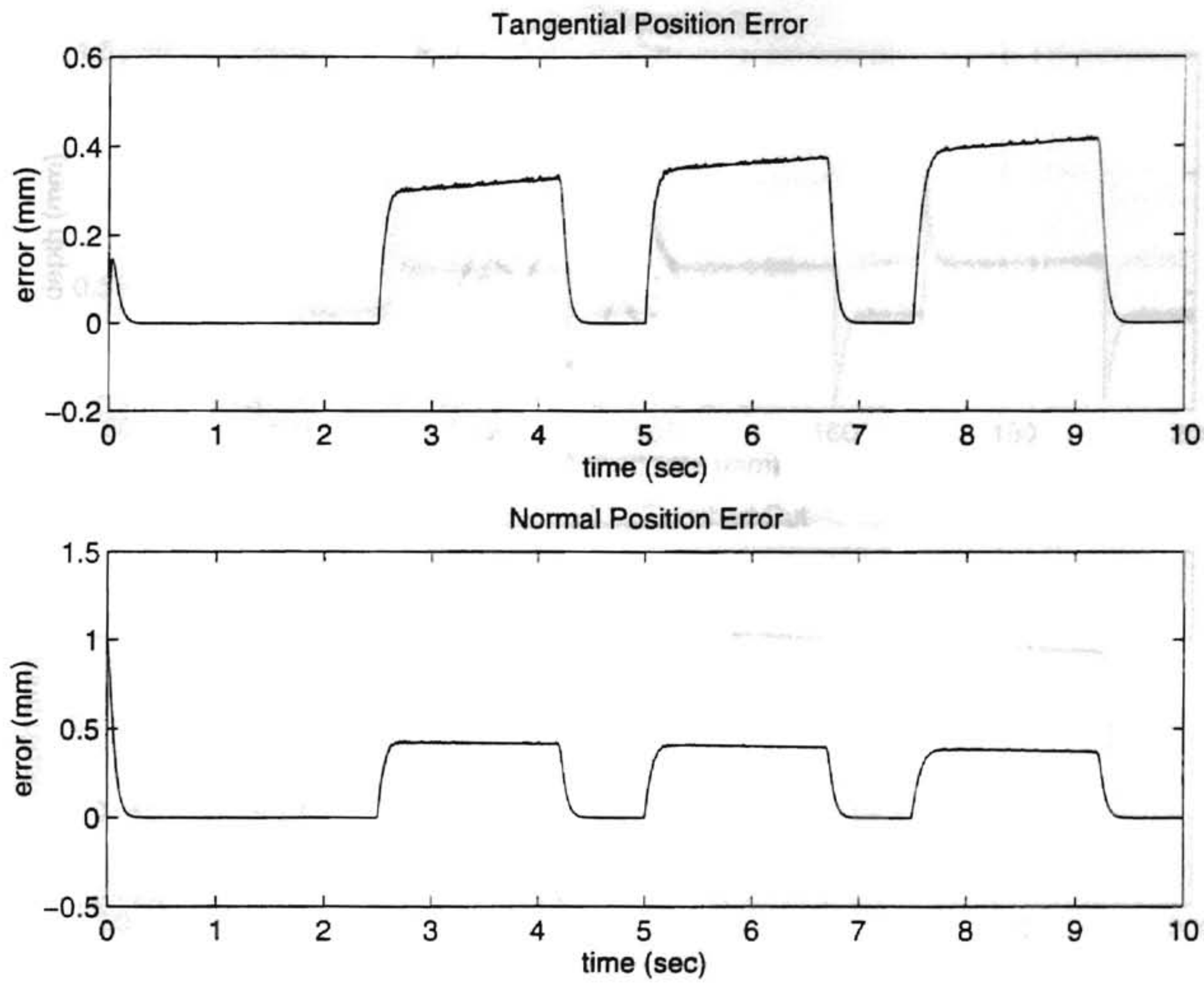

Figure 4.40 Results of Simulation 10 with Switching Control: Position Errors

Large Upset Burrs, ETG Workpiece

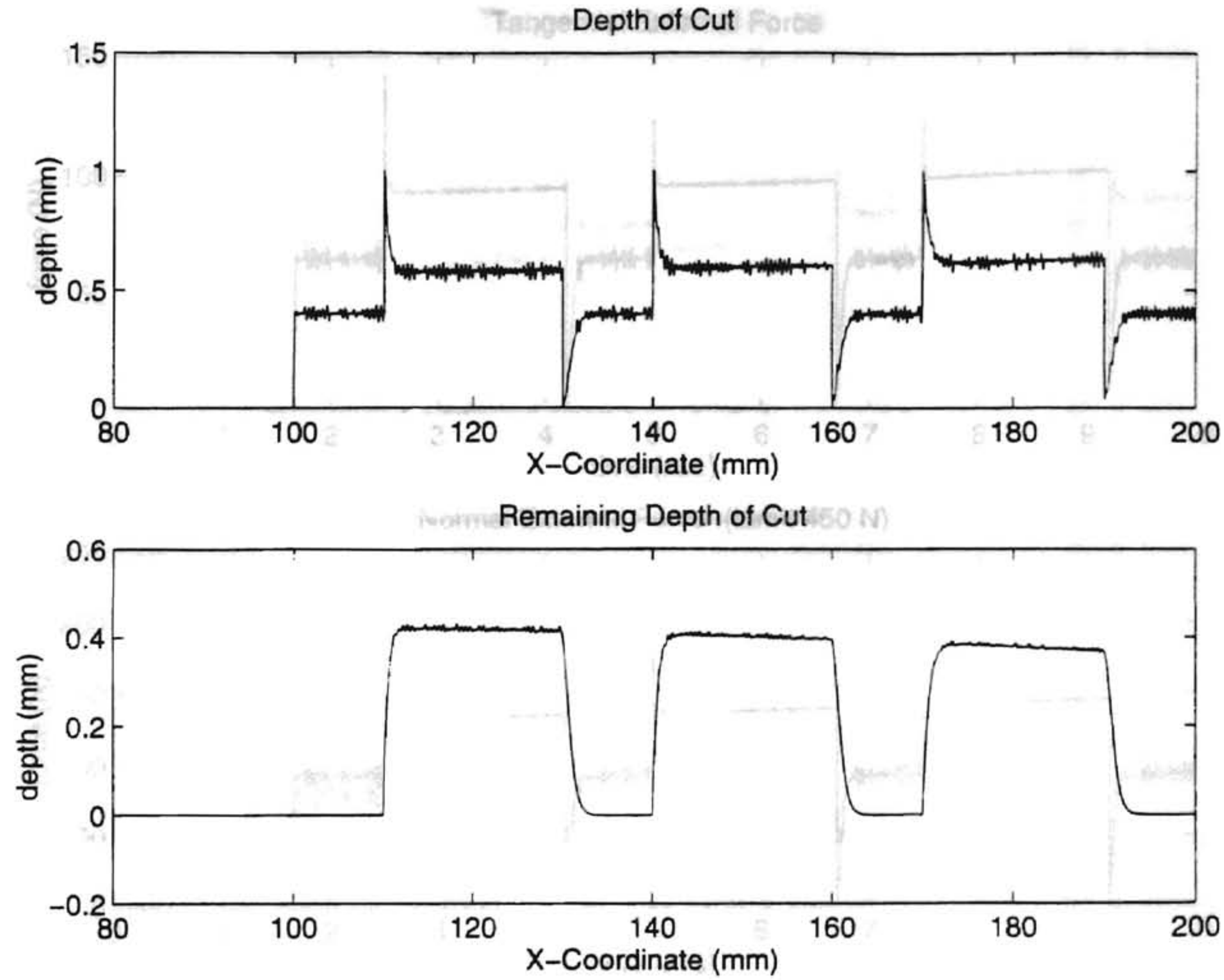

Figure 4.41 Results of Simulation 10 with Switching Control: Depth of Cut and Remaining Depth of Cut

Large Upset Burrs, ETG Workpiece

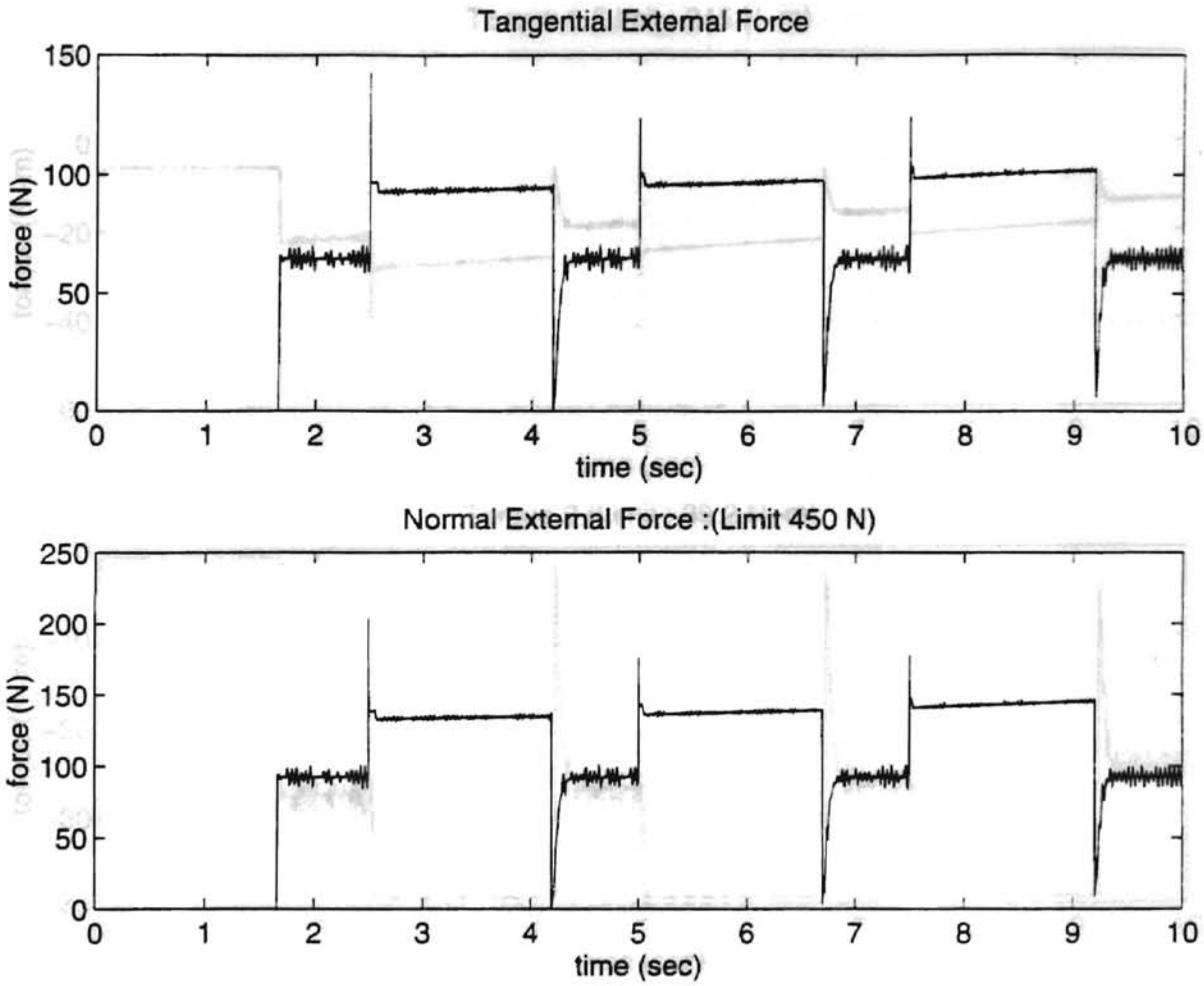

Figure 4.42 Results of Simulation 10 with Switching Control: External Forces

Large Upset Burrs, ETG Workpiece

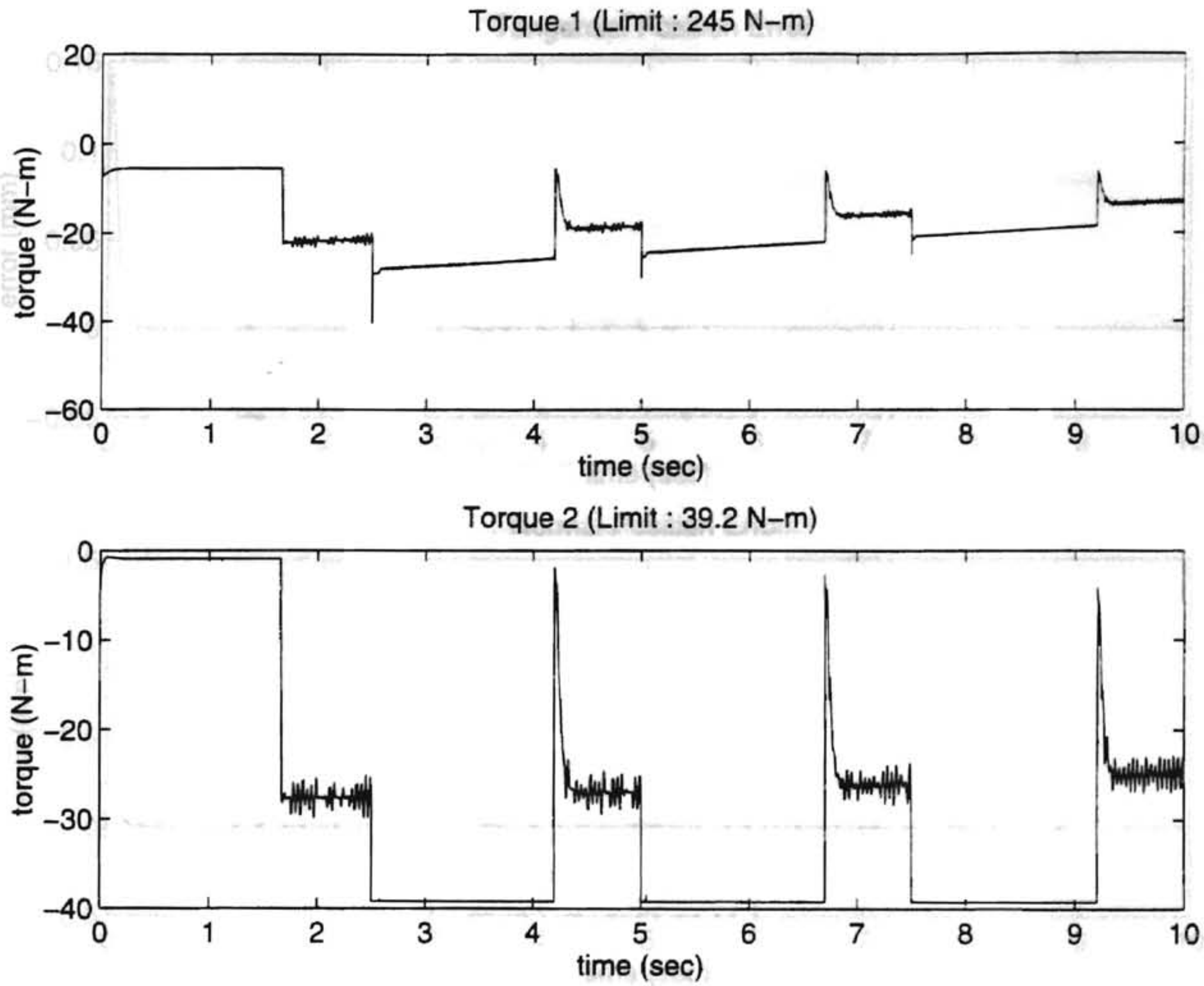

Figure 4.43 Results of Simulation 10 with Switching Control: Motor Torques

Large Upset Burrs, ETG Workpiece

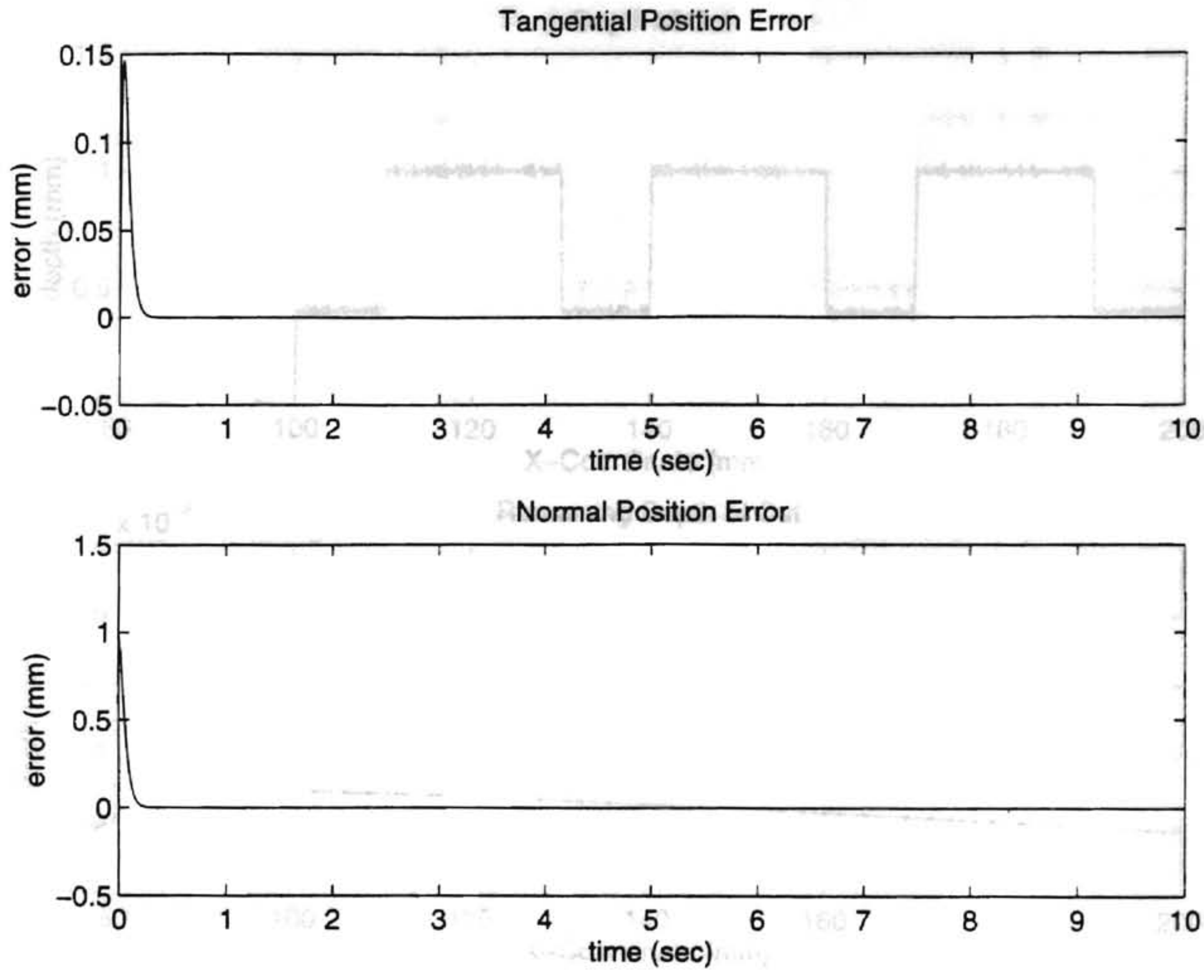

Figure 4.44 Results of Simulation 11 with Switching Control: Position Errors

Large Upset Burrs, ETG Workpiece, No Torque Limits

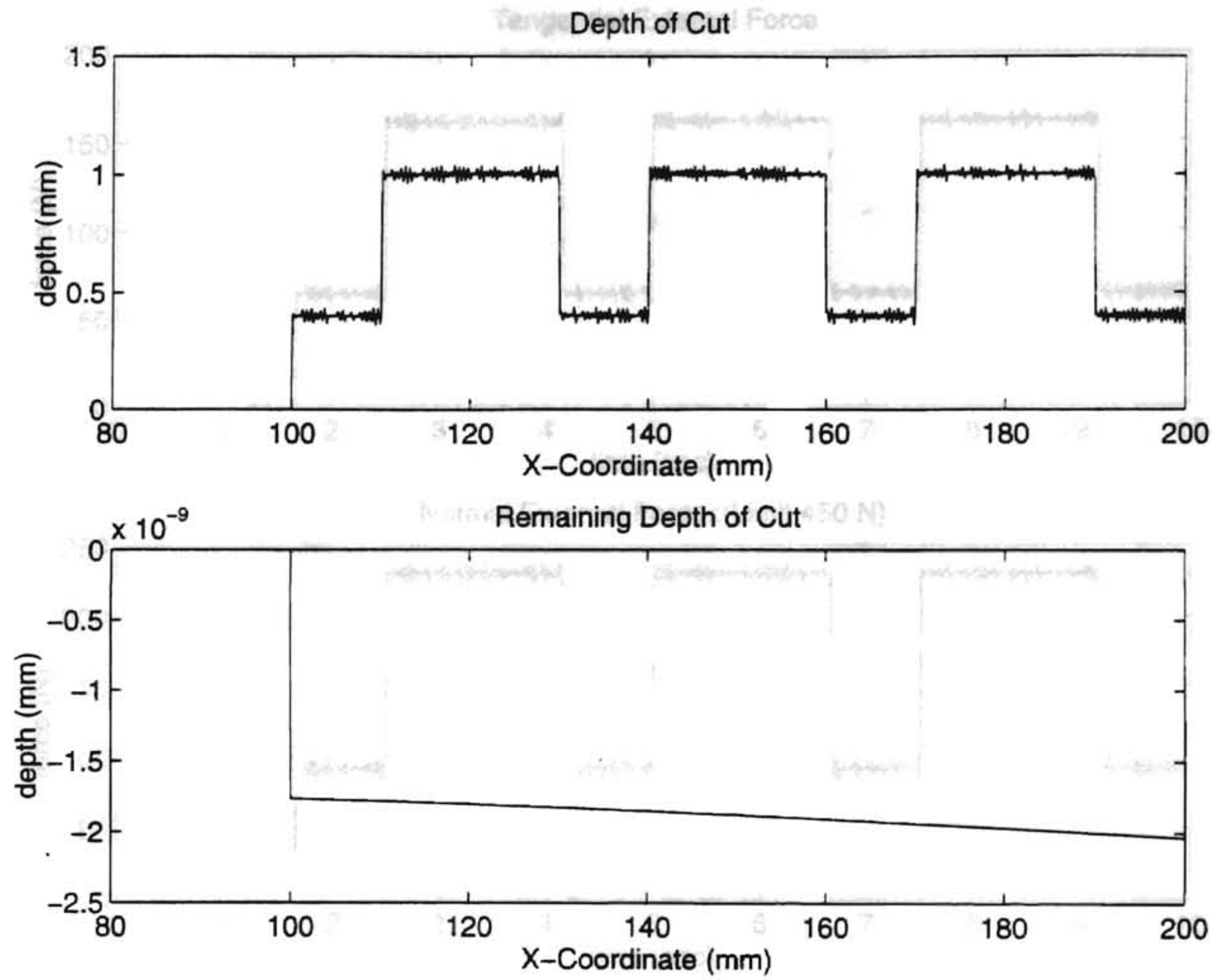

Figure 4.45 Results of Simulation 11 with Switching Control: Depth of Cut and

Remaining Depth of Cut

Large Upset Burrs, ETG Workpiece, No Torque Limits

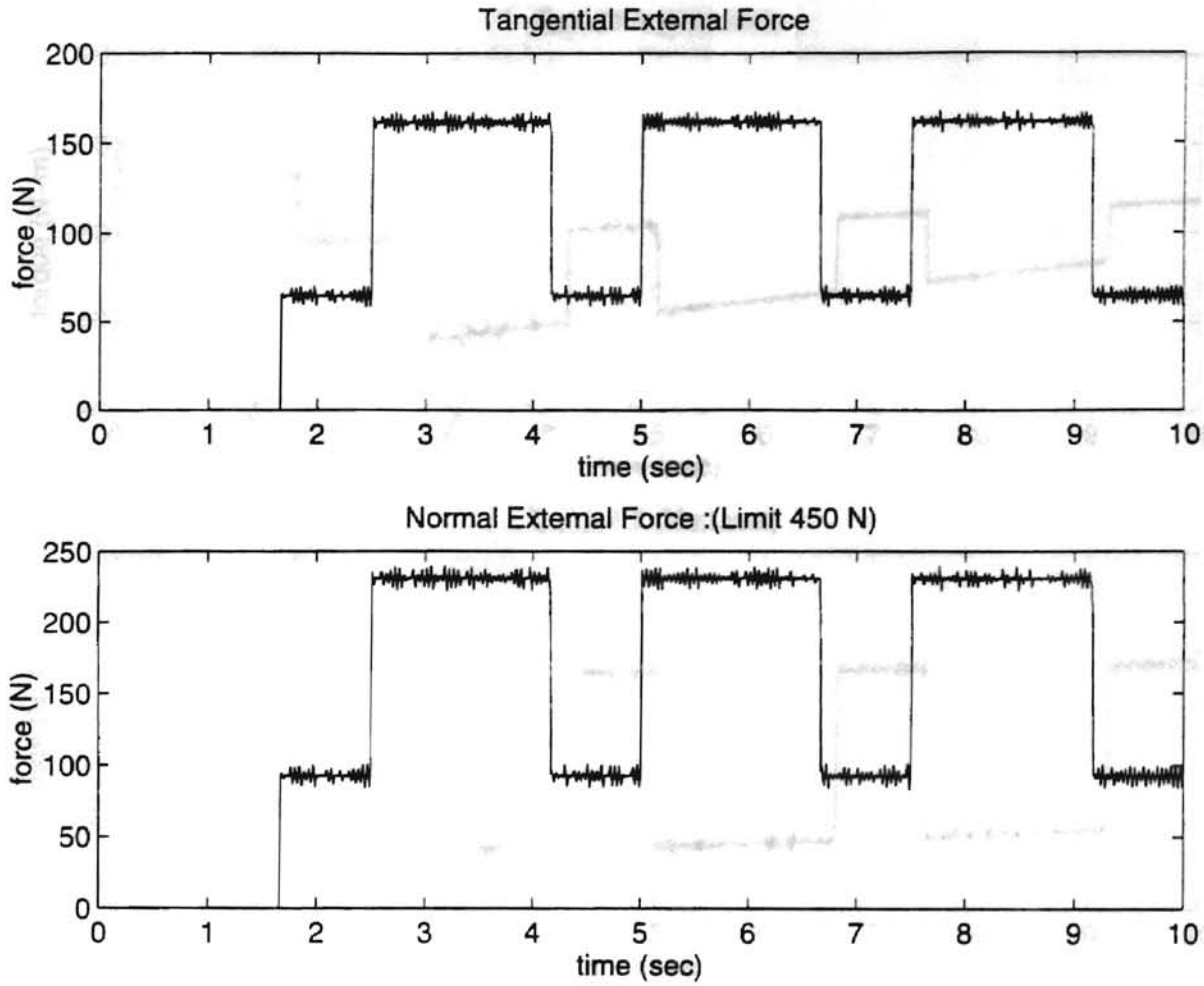

Figure 4.46 Results of Simulation 11 with Switching Control: External Forces

Large Upset Burrs, ETG Workpiece, No Torque Limits

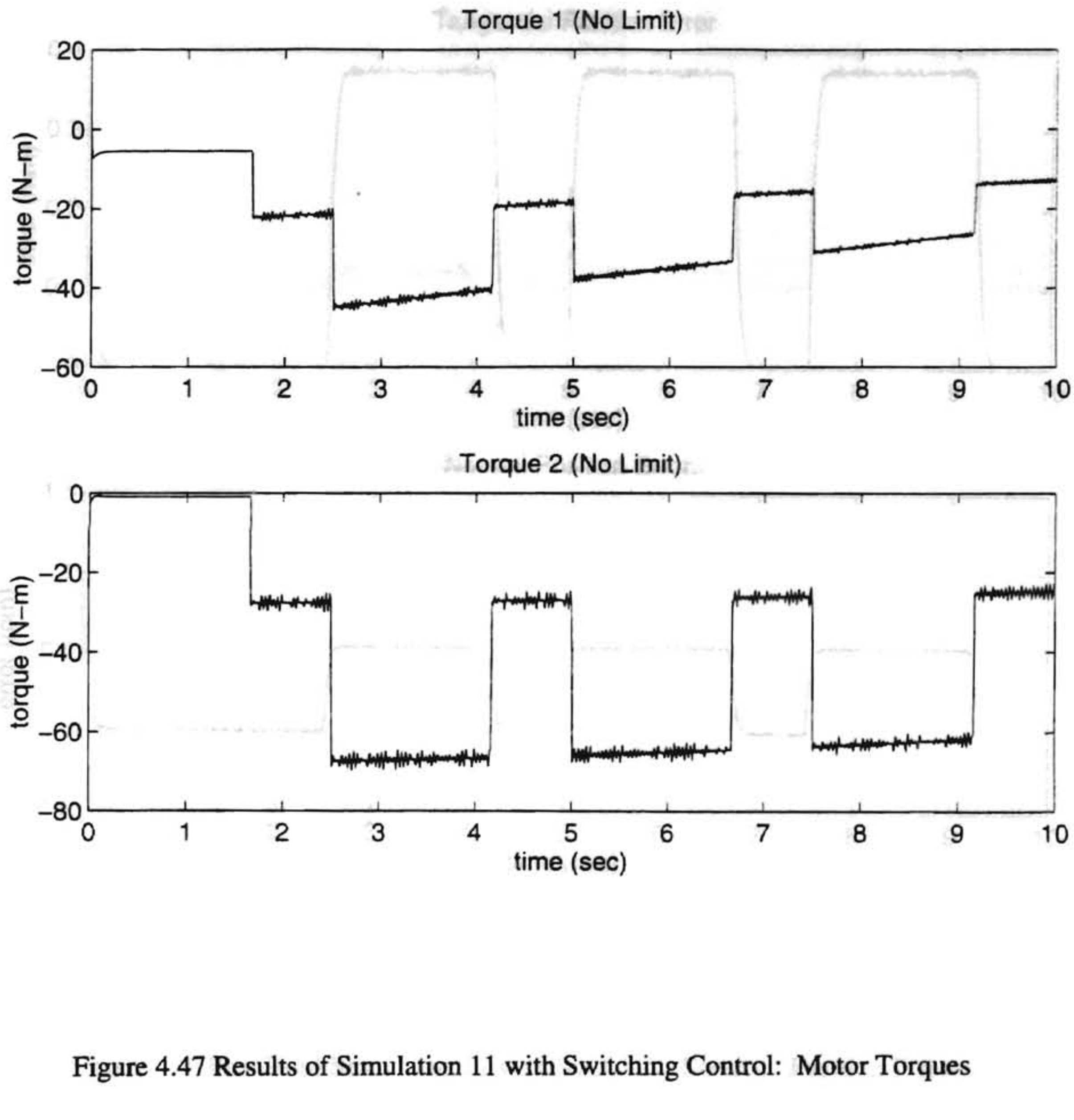

Figure 4.47 Results of Simulation 11 with Switching Control: Motor Torques

Large Upset Burrs, ETG Workpiece, No Torque Limits

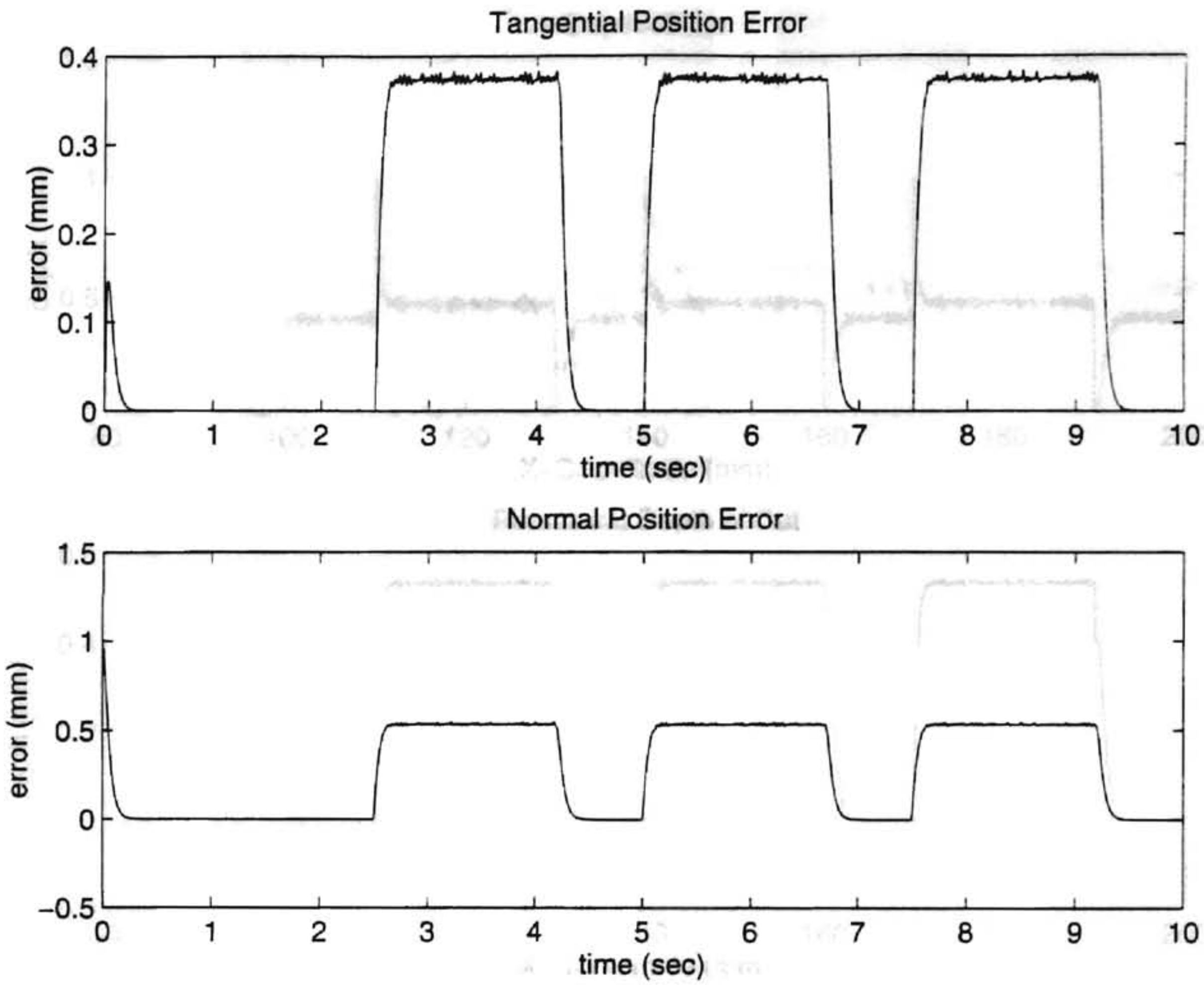

Figure 4.48 Results of Simulation 12 with Switching Control: Position Errors

Large Upset Burrs, DTG Workpiece, No Torque Limits

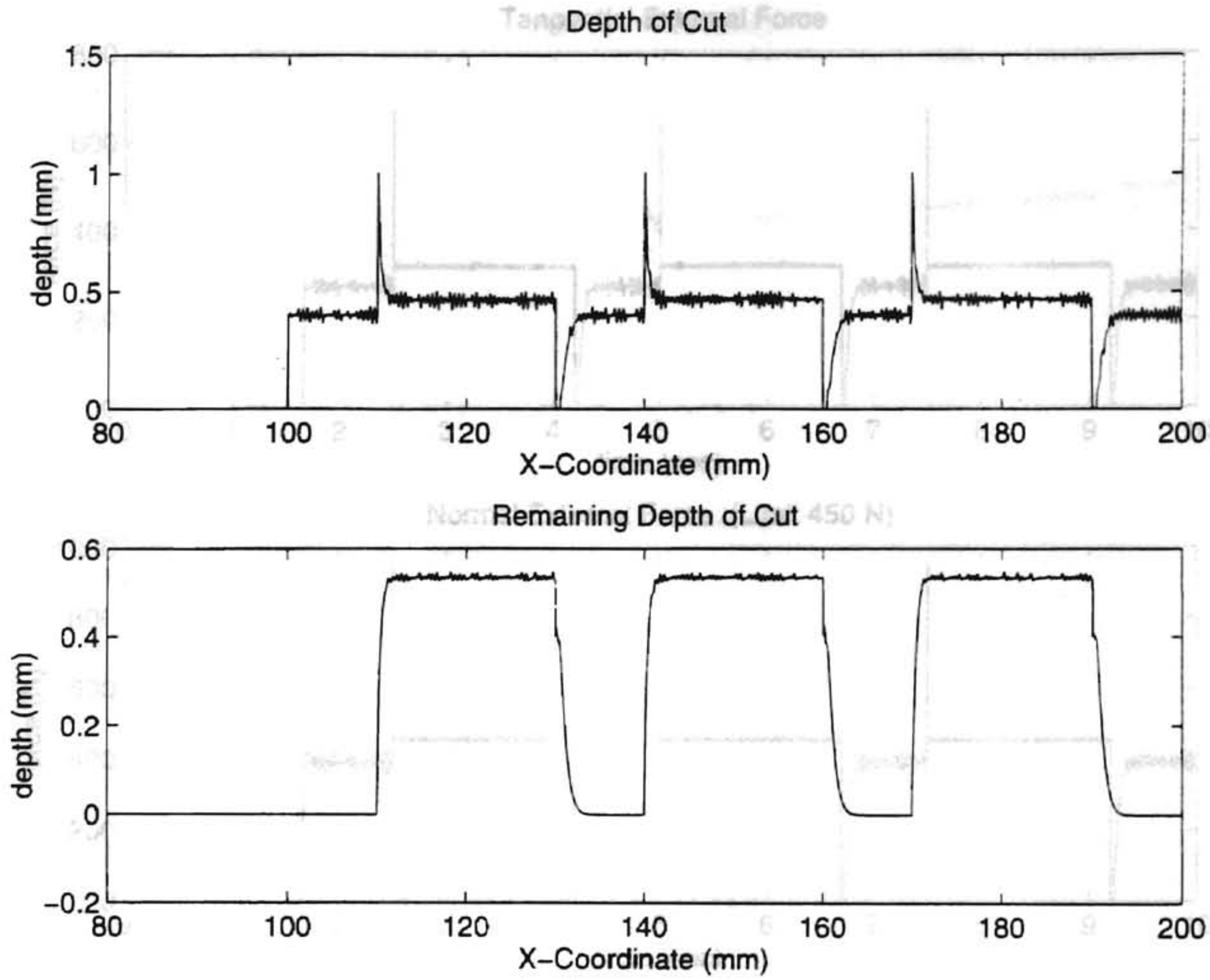

Figure 4.49 Results of Simulation 12 with Switching Control: Depth of Cut and Remaining Depth of Cut

Large Upset Burrs, DTG Workpiece, No Torque Limits

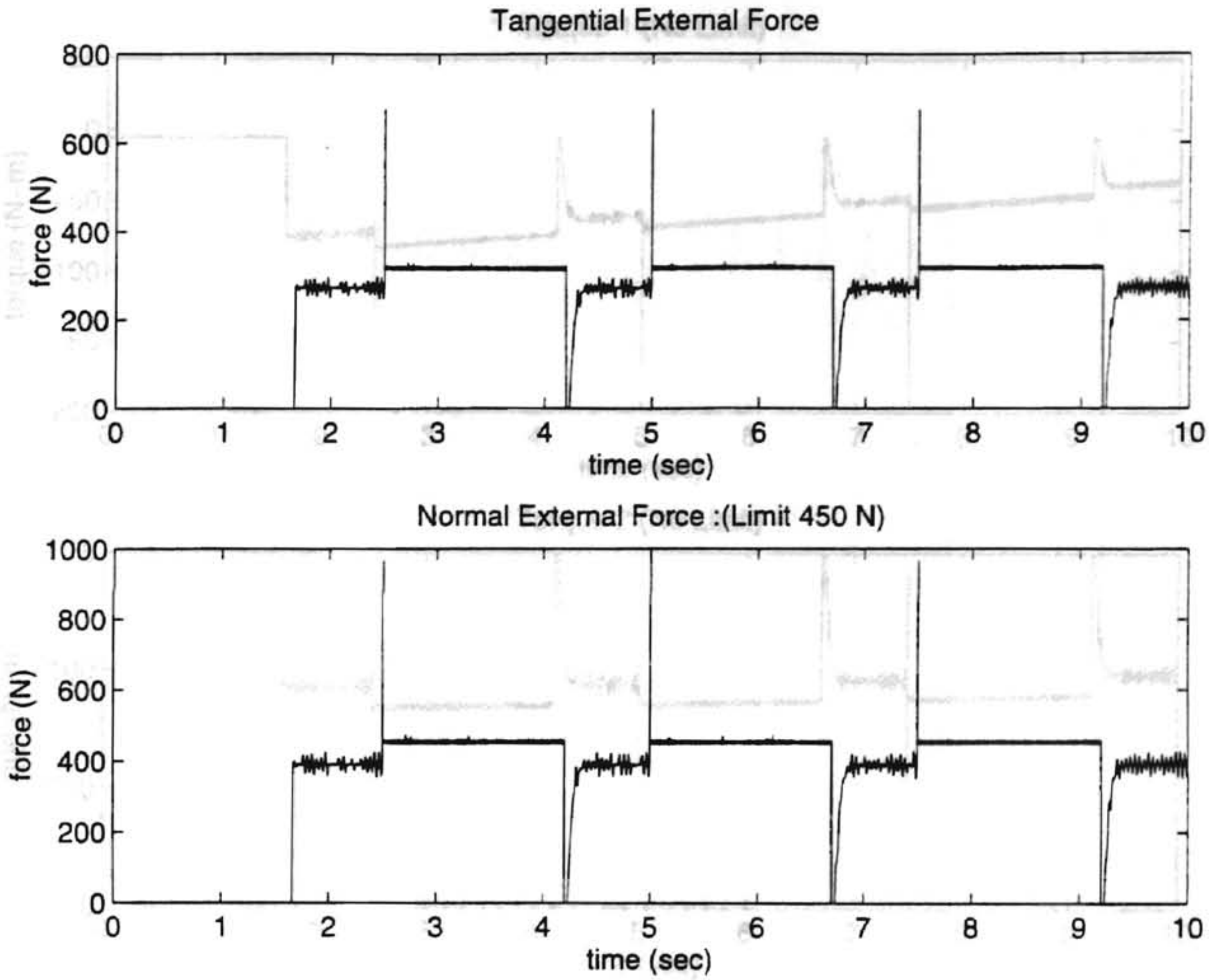

Figure 4.50 Results of Simulation 12 with Switching Control: External Forces

Large Upset Burrs, DTG Workpiece, No Torque Limits

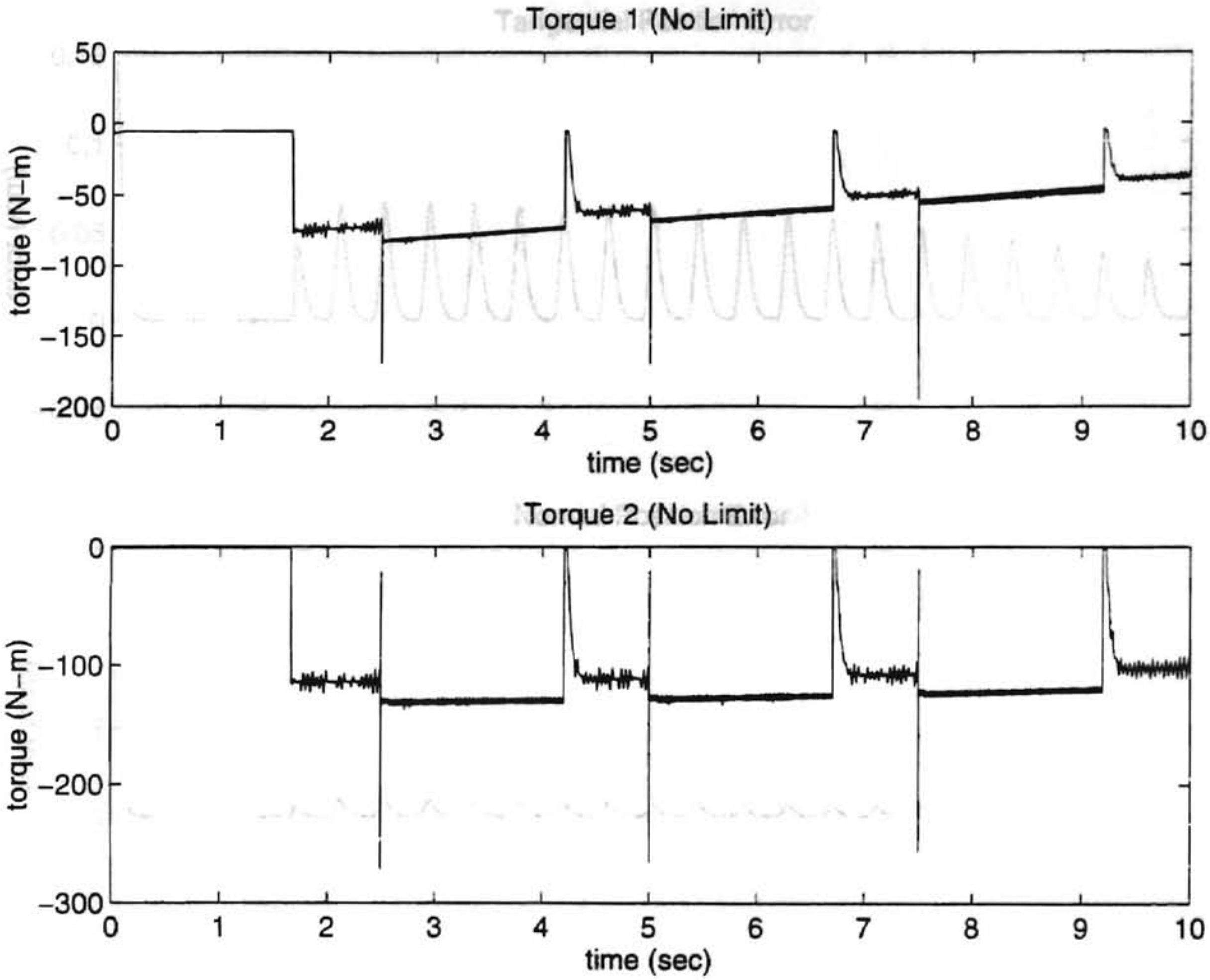

Figure 4.51 Results of Simulation 12 with Switching Control: Motor Torques

Large Upset Burrs, DTG Workpiece, No Torque Limits

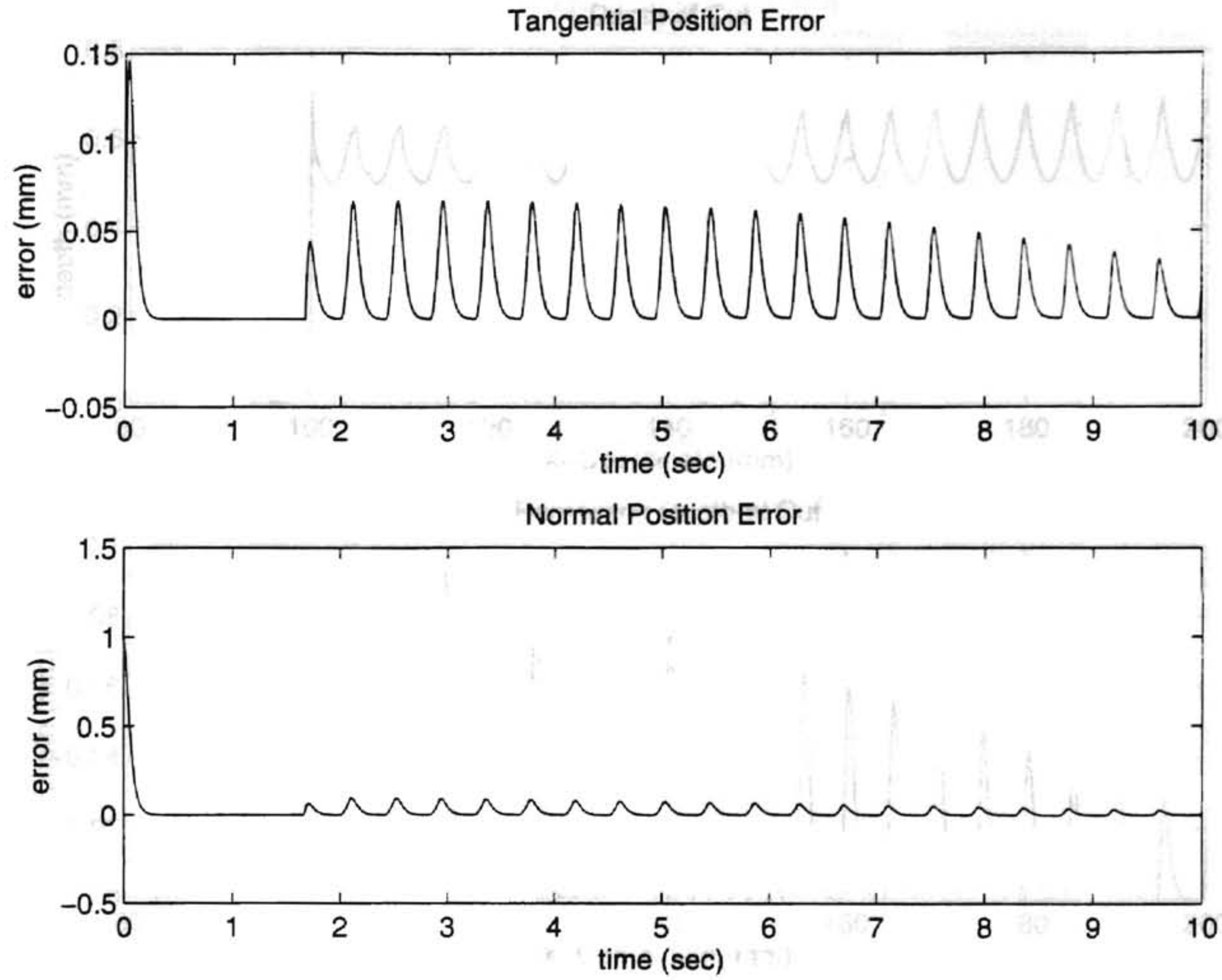

Figure 4.52 Results of Simulation 13 with Switching Control: Position Errors

Scallop Burrs, ETG Workpiece

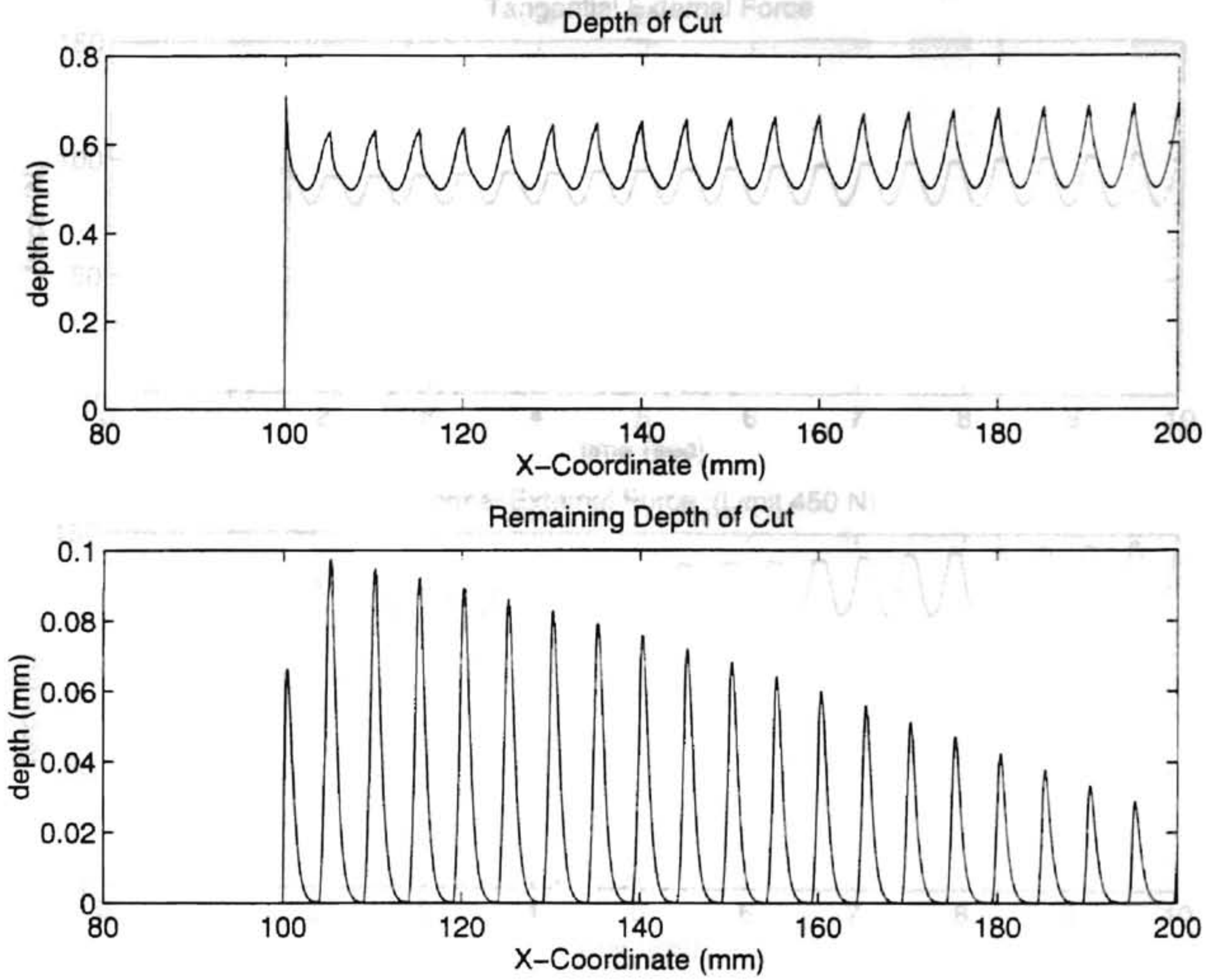

Figure 4.53 Results of Simulation 13 with Switching Control: Depth of Cut and

Remaining Depth of Cut

Scallop Burrs, ETG Workpiece

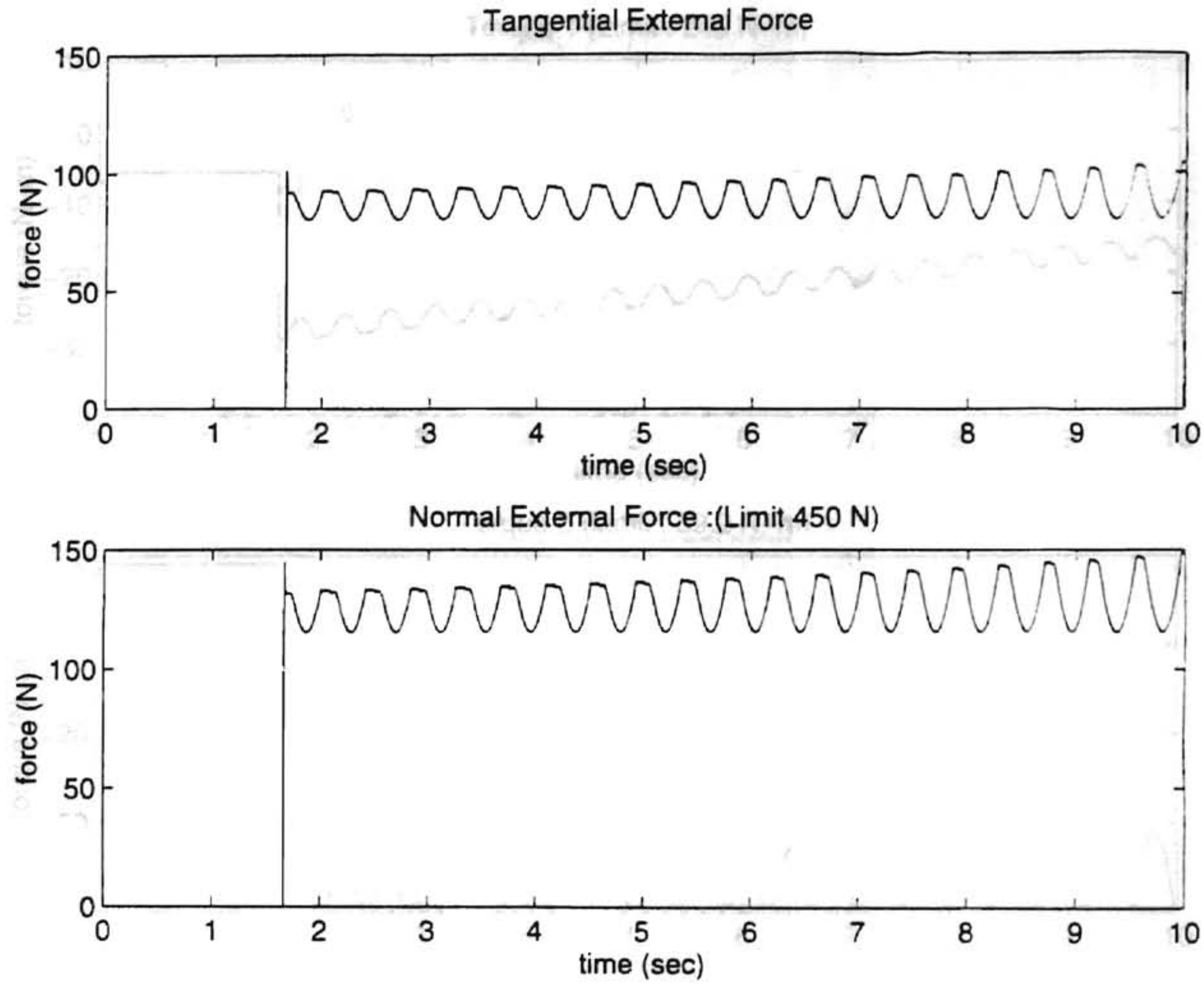

Figure 4.54 Results of Simulation 13 with Switching Control: External Forces

Scallop Burrs, ETG Workpiece

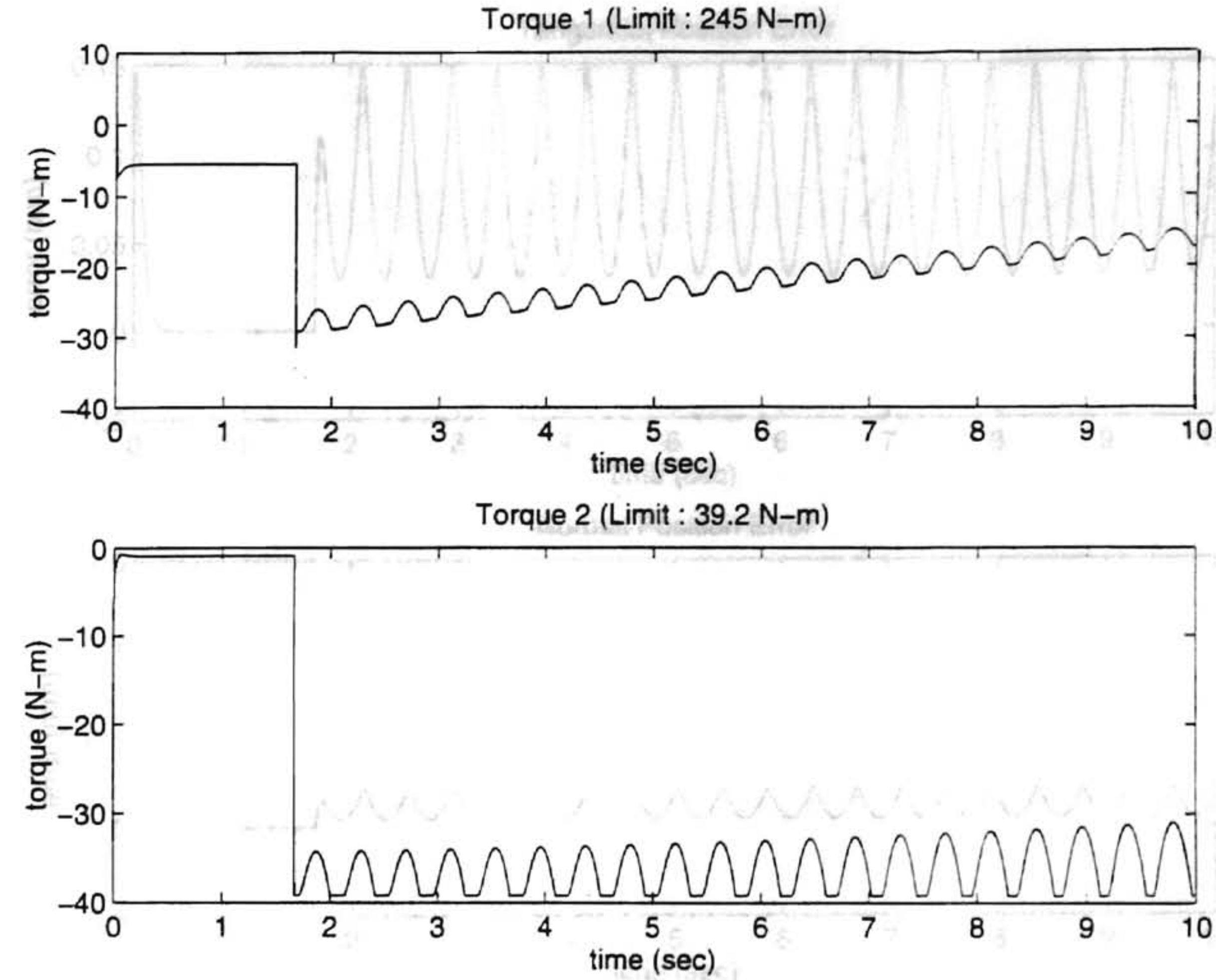

Figure 4.55 Results of Simulation 13 with Switching Control: Motor Torques

Scallop Burrs, ETG Workpiece

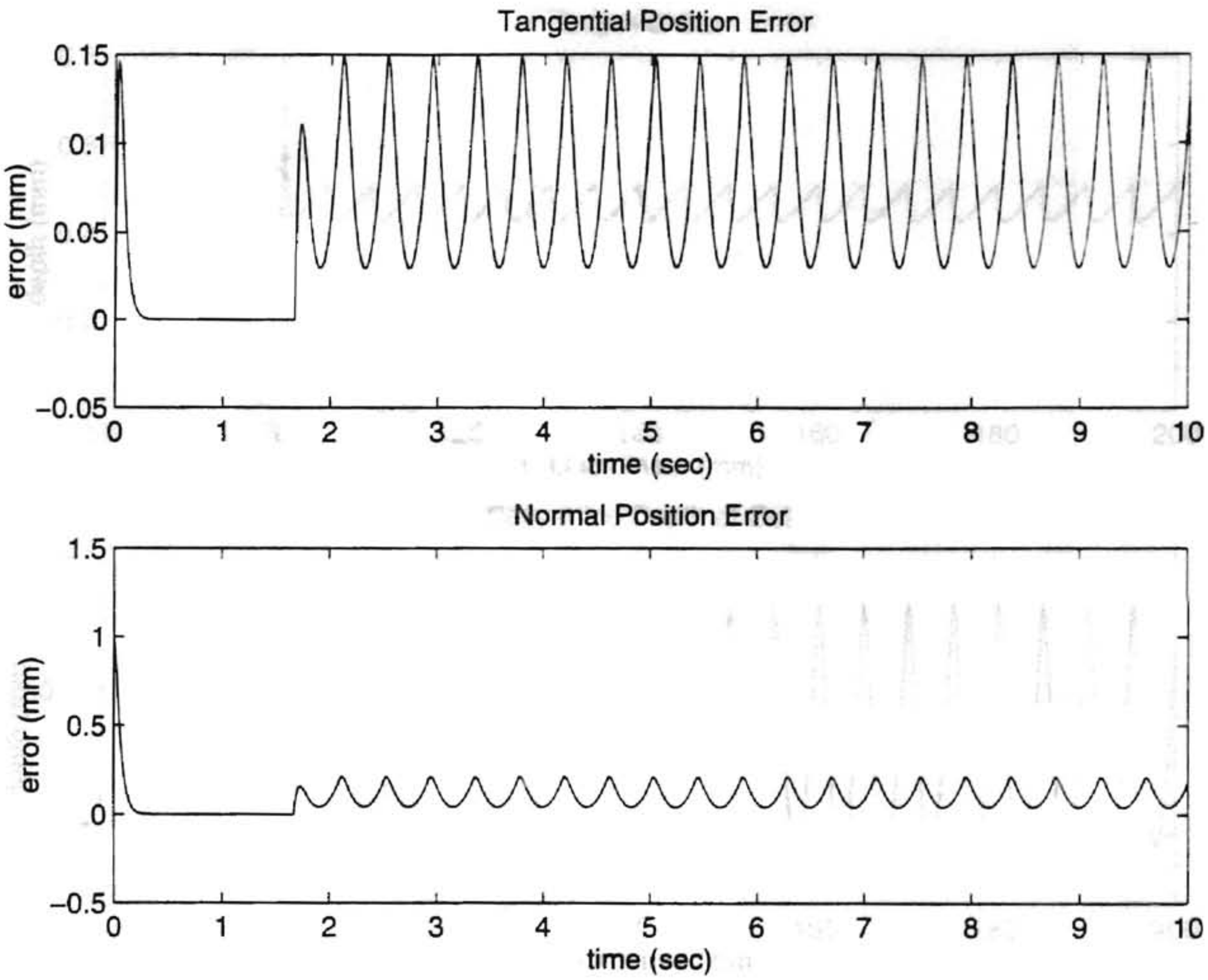

Figure 4.56 Results of Simulation 14 with Switching Control: Position Errors

Scallop Burrs, DTG Workpiece, No Torque Limits

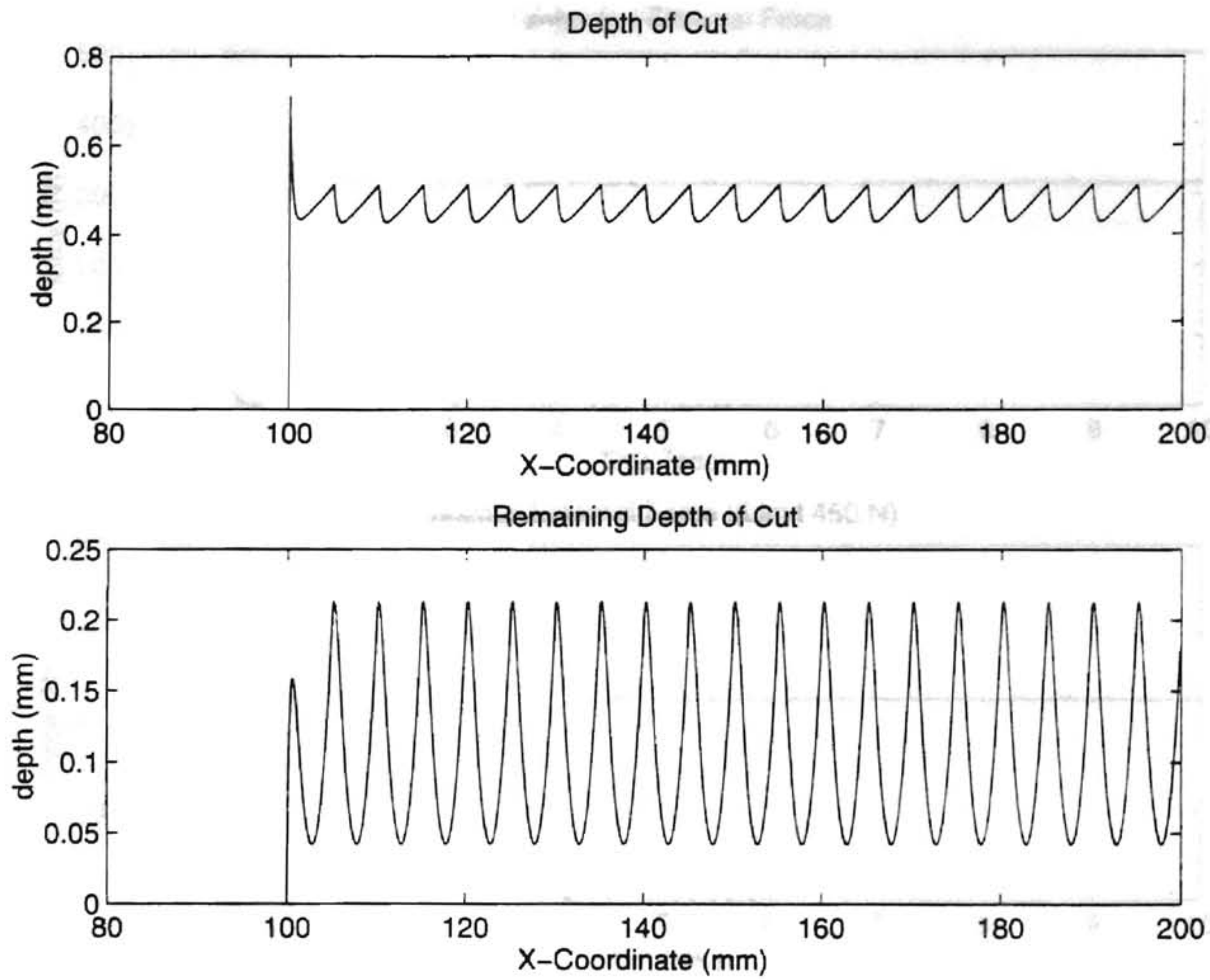

Figure 4.57 Results of Simulation 14 with Switching Control: Depth of Cut and

Remaining Depth of Cut

Scallop Burrs, DTG Workpiece, No Torque Limits

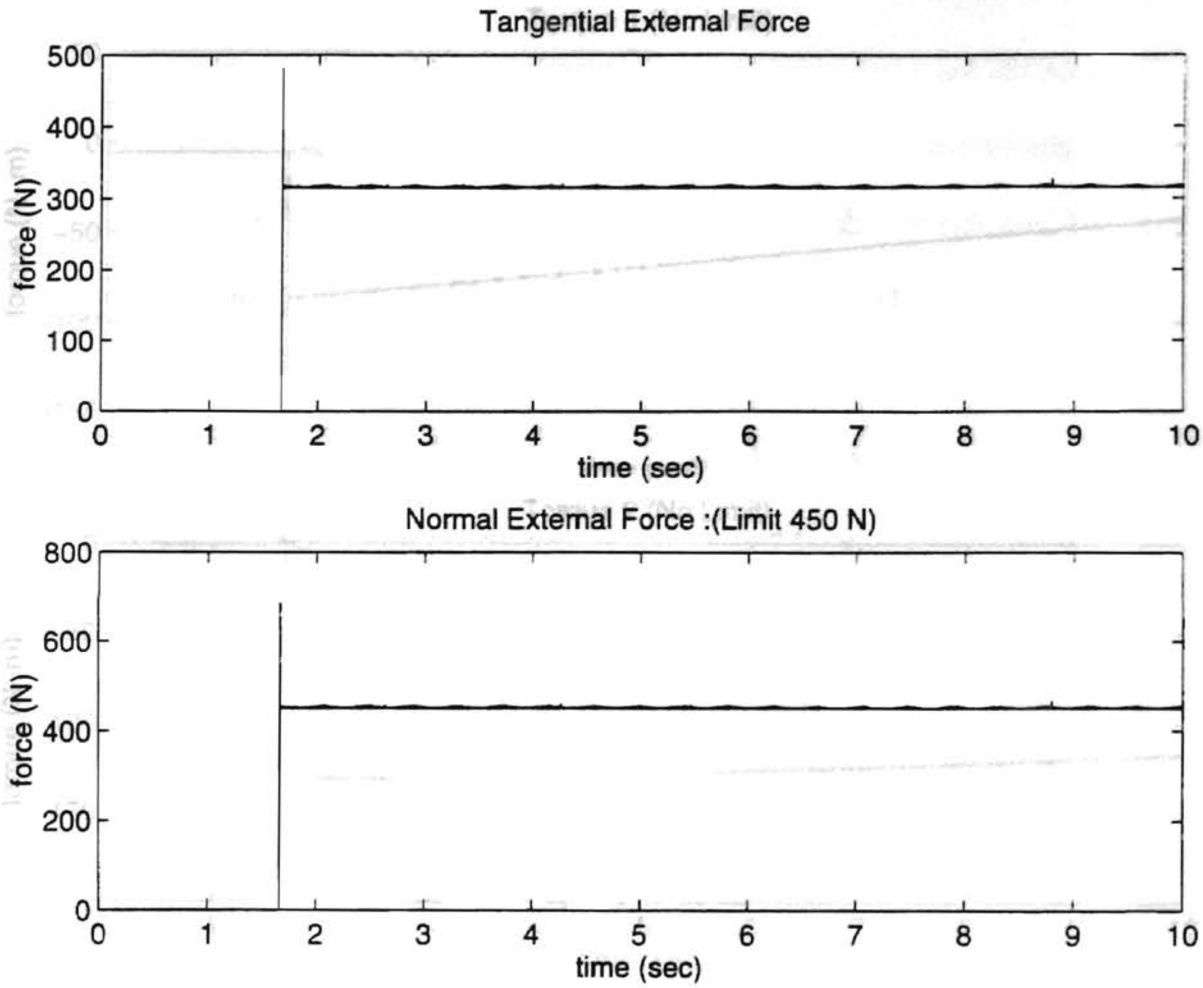

Figure 4.58 Results of Simulation 14 with Switching Control: External Forces

Scallop Burrs, DTG Workpiece, No Torque Limits

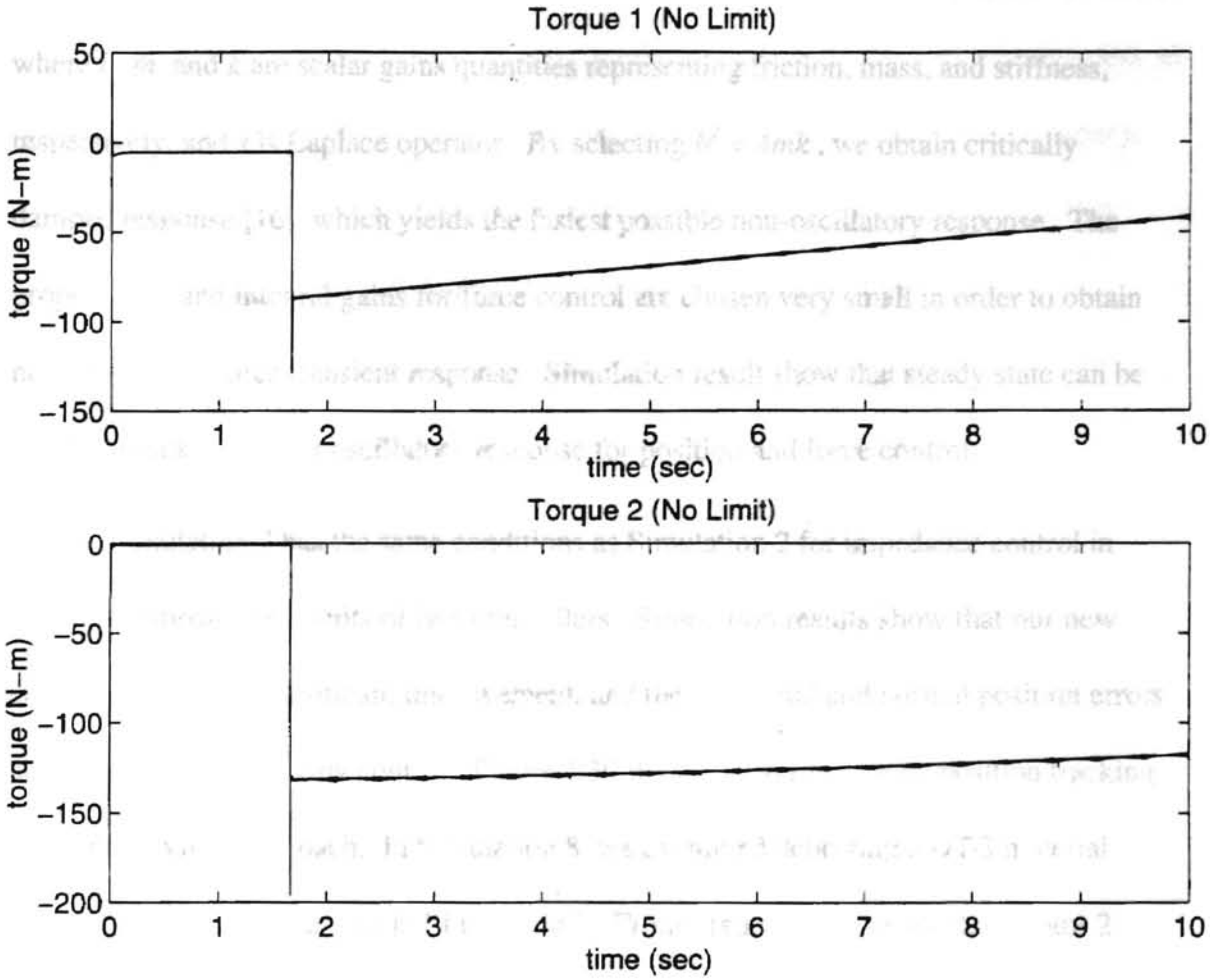

Figure 4.59 Results of Simulation 14 with Switching Control: Motor Torques

Scallop Burrs, DTG Workpiece, No Torque Limits

Discussion and Analysis for Switching Control

The position control parameters are chosen by considering the scalar characteristic equation of a position controller,

$$ms^2 + bs + k = 0 \tag{4.2}$$

where *b*, *m*, and *k* are scalar gains quantities representing friction, mass, and stiffness, respectively, and *s* is Laplace operator. By selecting $b^2 = 4mk$, we obtain critically damped response [16], which yields the fastest possible non-oscillatory response. The proportional and integral gains for force control are chosen very small in order to obtain non-oscillatory force transient response. Simulation result show that steady state can be reached quickly without oscillatory response for position and force control.

Simulation 7 has the same conditions as Simulation 2 for impedance control in order to compare the results of two controllers. Simulation results show that our new controller provides significant improvement, and the tangential and normal position errors are eliminated by this new control. Figure 4.30 illustrates very accurate position tracking using this control approach. In Simulation 8, we examined deburring a DTG material under the same conditions as in Simulation 7. From Figure 4.35, we see that Motor 2 reached its torque limit at numerous times throughout the simulation, which is the cause of large position errors in Figure 4.33 in both the tangential and normal directions. No controller can overcome this torque saturation situation, and in order to solve this problem, either smaller depth of cut should be commanded, or a higher-torque motor should be employed. We assume there are no motor torque limits in Simulation 9, and the results show a large improvement in Figure 4.36. However non-zero errors continue to occur, because the normal force limit was reached at numerous times, dictating switches to force control and giving up position accuracy, as shown in Figure 4.38. The force control regulated the normal grinding force reasonably well to the limit of 450 N as shown in Figure 4.38. The high-frequency force variations were caused by the irregularity of burrs, which were random-height sinusoidal in this simulation. In this case, smaller desired depth of cut in multiple passes of deburring and grinding should be employed in order to avoid the potential burning of workpiece or tool damage. Note from Figure 4.38 that switches between position and force control occur with high frequency in this case. Although, our simulation results do not indicate a potential stability problem with this frequent switching between two control modes, we have not developed a proof to guarantee stability for all deburring situations and all choices of controller gains.

In Simulations 10, 11, and 12, we employed large upset burrs to test the performance of our controller. Simulation results in Figure 4.40 for Simulation 10 with an ETG workpiece show that the grinding process did not reach the desired contour for large upset burrs because the torque of Motor 2 saturated at its limit for each upset, indicated in Figure 4.43. Again, we could employ smaller desired depths of cut or a higher-torque motor for Joint 2 to improve. This is demonstrated in Simulation 11, where we removed the torque limits on both motors. Figure 4.44 shows that a precise contour is achieved for the finished workpiece. In simulation 12, with torque limits removed, the grinding process reached the normal force limit when large upset burrs were encountered for a DTG material, requiring switching to force control, as seen in Figure 4.50. We have assumed in our modeling that cutting is instantaneous upon contact with a surface, such that impulsive forces and torques appear in our simulation results when the grinding wheel encounters large burrs. When the grinding wheel "jumps off" large burrs, it re-reaches the workpiece surface quickly, as seen in Figures 4.48 and 4.49.

Finally, we simulate our controller with scallop burrs for ETG and DTG workpieces in Simulations 13 and 14, respectively. Figure 4.52 shows periodic non-zero position errors for the ETG material, caused by torque saturation of Motor 2, shown in Figure 4.55. For the DTG workpiece with torque limits removed, Figure 4.56 shows larger position errors than for the ETG material. This is caused by reaching the normal force limit immediately, with force control in place throughout the simulation, as shown in Figure 4.58.

From our simulation results, we conclude that our controller can achieve an accurate finished workpiece edge for robotic deburring and grinding, but also provide the ability to control grinding forces to avoid potential damage to the workpiece and grinding tool. This controller appears to be more effective than controllers using impedance and hybrid impedance control. Like all controllers, however, the physics of the system prevent achieving accurate finishing on a single pass when force and torque limits are encountered. In the next chapter, we present conclusions of this work and recommendations for further study.

CHAPTER V

CONCLUSIONS AND RECOMMENDATIONS

Summary and Conclusions

In this study, we have focused on the control for position accuracy under force limits for a SCARA robot used for deburring and grinding. The following is a summary and relevant conclusions:

1. Based on traditional grinding mechanics, a grinding model previously developed for robotic deburring and grinding was employed. The grinding conditions were specified to calculate grinding forces for an easy-to-grind (ETG) and difficult-to-grind (DTG) workpiece material. Realistic force limits to prevent heat damage to the workpiece and tool breakdown for a selected grinding wheel were also determined and employed in simulations.
2. Stiffness calculations were conducted for the prototype robot employed in this study, the UC-Berkeley NSK SCARA robot, because this information was not available from the literature. The stiffness of the joint motors and robot links were estimated for worst-case conditions, which were then used to determine that the robot was sufficiently rigid to justify ignoring robot arm flexibility.

3. Two common control approaches for manipulators operating in constrained motion were investigated for robotic deburring and grinding. Simulation results showed that impedance control, which provides a stable and unified control structure for both free and constrained motion, may be suitable for "rough" deburring and grinding or edge following tasks. If the desired grinding force F_d is modeled well and surface geometry is known, desired forces may be commanded to increase the performance of impedance control. In contrast, hybrid impedance control, which provides independent force and position control in two orthogonal directions, produces large position errors, because displacement in the normal direction is adjusted indirectly by force control. For simple tasks such as edge-following or "peg-in-hole" operations, where non-zero contact force exists in the normal direction and zero contact force is assumed in the tangential direction, a hybrid impedance control scheme may be appropriate, but such control is unsuitable for robotic deburring and grinding.
4. A new approach to position and force control, called switching control, was proposed to increase accuracy in the finished workpiece profile using robotic deburring and grinding. This approach assumes that the primary requisite is highly accurate position, assuming the grinding forces remain below limits to protect workpiece and grinding tool. Otherwise, position accuracy is sacrificed to achieve force control to remain below these limits. This control approach is able to achieve good performance for grinding different types of burrs and materials. Position errors caused by insufficient motor torque can be addressed by using multiple passes of deburring with smaller depths of cut, or higher-torque motors. From simulation results, we conclude that this

controller can achieve an accurate finished workpiece edge for robotic deburring and grinding while providing a mechanism to regulate the grinding forces to avoid potential burning of the workpiece and damage of the grinding tool. It appears to be superior to impedance and hybrid impedance control.

5. Although our simulations indicate stability and good dynamic behavior with suitable gain choices for switching control, we were unable to prove stability. It is possible that unstable behavior under torque saturation and frequent switching may occur. This requires further study.
6. We assume the contact velocity between grinding wheel and workpiece is relatively small, such that no bouncing occurs on contact as material removal begins. For high contact velocities, "bounce off" may occur, and we have not been able to prove contact stability. More work is needed in this area.

Recommendations

Further investigations following this study are recommended as follows:

1. A detailed examination and model is needed to verify whether our assumptions regarding no bouncing at low contact velocities is valid and to determine conditions for stability at all contact velocities.
2. A proof of stability for our proposed switching control should be developed.
3. An experimental setup should be designed and a set of experiments conducted to verify the results of this study.
4. The proposed approach should be applied, both in simulation and in test, to follow a curved edge.
5. Because an accurate model of the dynamics of the interaction between the manipulator and the environment during deburring and grinding is difficult, an adaptive controller with on-line estimates of material removal rates and other system parameters, combined with the control scheme developed in this study, may result in more robust and realistic control performance. Such an investigation should be undertaken.

REFERENCES

1. Ananiev, A., "Robots In Finishing Operations," Fifth World Conference on Robotics Research, Cambridge, 1994, pp. 6-29 to 6-40.
2. Tool and Manufacturing Engineers Handbook: A Reference Book for Manufacturing Engineers, Managers, and Technicians, vol. 3, Dearborn, Mich. 1992.
3. Hong, D., Position/Force Control of Manipulators Used for Deburring and Grinding, M.S. Thesis, School of Mechanical and Aerospace Engineering, Oklahoma State University, Stillwater, OK., May, 1995.
4. Tarn, T. J., Wu, Y., Xi, N., and Isidori, A., "Force Regulation and Contact Transition Control," IEEE Control Systems, vol. 16, no. 1, pp. 32-40, February 1996.
5. Mills, J. K., and Lokhorst, D. M., "Control of Robotic Manipulators During General Task Execution: A Discontinuous Control Approach," International Journal of Robotics Research, vol. 12, no. 2, pp. 861-874, April 1993.
6. Hyde, J., and Cutkosky, M., "Contact Transition Control: An Experimental Study," Proceedings of the IEEE International Conference on Robotics and Automation, pp. 363-368, Atlanta, Georgia, 1993.

7. Volpe, R., and Khosla, P., "A Theoretical and Experimental Investigation of Impact Control for Manipulators," International Journal of Robotics Research, vol. 12, no. 4, pp. 351-365, August 1993.

8. Marth, G. T., Tarn, T. J., and Bejczy, A. K., "Stable Phase Transition Control for Robot Arm Motion," Proceedings of the IEEE International Conference on Robotics and Automation, pp. 355-362, Atlanta, Georgia, 1993.

9. Hogan, N., "Impedance Control: an Approach to Manipulation, Part I: Theory, Part II: Implementation, Part III: Applications," ASME J. Dynam. Sys. Meas. Control, vol. 107, no. 1, pp. 1-24, March 1985.

10. Spong, M. W. and Vidyasagar, M., Robot Dynamics and control, John Wiley & Sons 1989.

11. Hogan, N., "Stable Execution of contact Tasks Using Impedance Control," Proc. IEEE Int. Conf. Robot Autom., pp. 1047-1054, Raleigh NC, March 1987.

12. McCormick, W., and Schwartz, H. M., "An Investigation of Impedance control for Robot Manipulators," The International Journal of Robotics Reaserch, vol. 12, no. 5, pp. 473-489, 1993.

13. Colgate, E., and Hogan, N., "Robust Control of Dynamically Interacting Systems," Int. J. of Control, vol. 48, no. 1, pp. 65-88, 1988.

14. Kazerooni, H., Sheridan, T., and Houpt, P., "Robust Compliant Motion for Manipulators, Part I: The Fundamental Concepts of Compliant Motion, Part II: Design Method," IEEE J. Robot. Automation, vol. RA-2, no. 2, pp. 83-91, June 1986.

15. Raibert, M., and Craig, J., "Hybrid Position/Force Control of Manipulators," ASME J. Dynam. Sys. Meas. Control, vol. 102, no. 2, pp. 126-133, June 1981.

16. Craig, J. J., Introduction to Robotics Mechanics & Control: Second Edition, Addison-Wesley Publishing Company, Inc., 1989.

17. Anderson, R. J., Spong, M. W., "Hybrid Impedance Control of Robotic Manipulators," IEEE J. of Robotics and Automation, vol. 4, no. 5, pp. 549-556, October 1988.

18. Pagilla, P. R., Control of Constrained Nonlinear Mechanical Systems: Applications to Robot Manipulators, PH.D. Dissertation, Mechnical Engineering, University of California, Berkeley, CA, 1996.

19. Kang, C.G., Kao, W. W., Boals, M., and Horowitz, R., "Modeling Identification and Simulation of a Two Link Scara Manipulator," The Winter Annual Meeting of ASME, Chicago, 1988, v11, pp. 393-407.

20. Hahn, R. S., and Lindsay, R. P., "Principles of Grinding," 5 part series in Machinery, July-Nov. 1971.

21. King, R. S., and Hahn, R. S., Handbook of Modern Grinding Technology, Chapman and Hall, New York, 1986.

22. Malkin, S., Grinding Technology: Theory and Applications of Machining with Abrasives, Ellis Horwood Limited, 1989.

23. Mechatronic Actuators, Cat. No E3153, NSK Ltd., 1994.

24. Higdon, A., Ohlsen, E. H., Stiles, W. B., Weese, J. A., and Riley, W. F., Mechanics of materials, 3rd Edition, John Wiley and Sons, 1976.

25. Roark, R. J., and Young, W. C., Formulas for Stress and Strain, McGraw-Hill Book Company, 1975.

26. Kazerooni, H., "On the Robot Compliant Motion Control," ASME J. Dynam. Sys. Meas. Control, vol. 111, pp. 416-425, September, 1989.

27. Slotine, J.-J. E. and Li, W., Applied Nonlinear Control, Prentice Hall, 1991.

28. Kazerooni, H., Bausch, J. J., and Kramer, B. M., "An Approach to Automated Deburring by Robot Manipulators" ASME J. Dynam. Sys. Meas. Control, vol. 108, pp. 354-359, December, 1986.

29. MATLAB Reference Guide, (1995), Natick, Mass., The Math Works, Inc.

30. SIMULINK User's Guide, (1995), Natick, Mass., The Math Works, Inc.

APPENDIX

APPENDIX A

NSK ROBOT SPECIFICATIONS

MOTION & CONTROL
NSK

Mechatronic Actuators

Direct Drive Actuators
High-Precision Linear Positioning Tables
Robot Modules
Positioning Actuator
Monocarrier C series

CAT. No. E3153

PREFACE

We would like to express our deepest gratitude for your interest in NSK products. For your convenience, NSK has edited the catalogs usually issued individually for Mechatronic Products, in order to integrate them into a general catalog of NSK Mechatronic Actuators. In addition, the technical expertise contained in this catalog is supported by the latest reserch and development, and information is offered beyond that in the usual product-only catalog.

This catalog is divided into two product sections.

A. Direct Drive(DD) Acuators

B. High-Precision Linear Positioning Tables and Actuators

The brief features of the products are as follows.

A. DD Acuators

①Megatorque Motor : Driving a load directly coupled without using a reduction gear.

②Megathrust Motor : Linear Motor offering rapid and highly precise positioning.

③Mega Indexer : Numerically controlled direct drive rotary table which is compact and indexes at high speed.

B. High-Precision Linear Positioning Tables and Actuators

①High-Precision Linear Positioning Tables : High-precision Linear Positioning Tables using NSK Ball Screw and NSK Linear guide.

②Robot Modules : A wide variety of mono-axis linear positioning modules which is easy to combine into Cartesian robot.

③Positioning Actuator : Compact linear positioning actuator which is economical and easy to operate

④Monocarrier C serise : Monocarrier M series with motor, cover and controller. Compact and rigid linear actuator.

We hope this catalog is very helpful for your design needs.

1994-9

1.5 Standard Product Series

1.5.1 specifications

Motor Model 0408, 0608, 0810, 1010, 1410 are standard.
Motor Model 0404, 0602, 0604, 0606, 0806 1006
1413, 1420, are semi-standard.

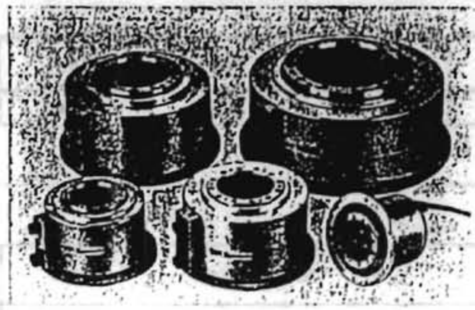

Photo 1.1 Standard Product Series

Items	Motor Model	0404	0408	0602	0604	0606	0608	0806	0810
Motor	Max. Torque*1 (N·m)	3.9	9.8	5.8	14.7	24.5	39.2	52.9	88.2
	Max. Current/phase*2 (A)	3/1.5	6/3		6/6			7.5/7.5	
	Winding Voltage*2 (VDC)	165/330							
	Max. Friction Torque (N·m)	1		3				4.5	
	Allowable Axial Load*5 (N)	1760		3729				4500	
	Allowable Moment Load*5,*6 (N·m)	19		58				78	
	Axial Rigidity (mm/N)	2.55×10^{-5}		4.08×10^{-6}				3.06×10^{-6}	
	Moment Rigidity*6 (rad/N·m)	3.06×10^{-6}		3.57×10^{-6}				2.55×10^{-6}	
	Rotor Inertia J(MR²) (kg·m²)	0.002	0.0023	0.0038	0.005	0.007	0.0075	0.016	0.02
	Mass (kg)	4.5	6.5	9	11	12.5	14	20	24
	Environment conditions	Operation Temp. : 0°C ~40°C Humidity : 20%~80%, Indoor use only							
	Basic Specifications	Rate : continuous, Protection : totally Enclosed, Non-Vented Insulation : F, Winding Insulation Test : AC 1500V for one minute							
	compatible Driver Unit Type	EM0404	EM0408	EM0602	EM0604	EM0606	EM0608	EM0806	EM0810 EP0810
Motor Driver Coupling	Main AC Line Voltage (VAC)	3φ/1φ 220V±10% 50/60Hz or 1φ 100~128V 50/60Hz							
	Contol AC Line Voltage(VAC)	1φ 90~240V 50/60Hz							
	Main AC Line Power Cap.*2,*3 (KVA)	1/0.5	1.5/0.5	1/1	1/1.5		1/1.5 2	1/2	1.5/2 3
	Max. Speed (rps)	4.5		3					
	Resolver Resolution*4 (counts/rev)	409600/102400		614400/153600					
	Resolver Accuracy (arc-sec)	±60		±30					
	Resolver Repeatability*4 (arc-sec)	±3.2/±12.8		±2.1/±8.4					

*1 In case of the operation at zero speed for long periods, see Megatorque motor output torque characteristics (A100 page)
*2 The first figure indicates main AC line 110V, the second indicates main AC line 220V.
*3 The second line indicates in case that the compatible driver unit is EP type.
*4 The first figure indicates 12 bit resolver resolution, the second indicates 10 bit resolution.
*5 When more load capacity is required, the additional bearing is necessary. Consult with NSK.
*6 Allowable moment load and moment rigidity are mesured in case of the motor mounted on the rigid base.

SI unit System : 1N = 0.102kgf = 0.225lb
1N·m = 0.102kgf·m = 0.738ft·lb

NSK

	Items \ Motor Model	1006	1010	1404	1410	1413	1420
Motor	Max. Torque*1 (N·m)	88.2	147	88.2	245	294	490
	Max. Current/phase*2 (A)	7.5/7.5					
	Winding Voltage*2 (VDC)	165/330					
	Max. Friction Torque (N·m)	5.4		7.9			
	Allowable Axial Load*5 (N)	9500		19600			
	Allowable Moment Load*5,*6 (N·m)	156		392			
	Axial Rigidity (mm/N)	1.43×10^{-6}		1.01×10^{-6}			
	Moment Rigidity*6 (rad/N·m)	1.53×10^{-6}		3.06×10^{-7}			
	Rotor Inertia J(MR²) (kg·m²)	0.07	0.075	0.2	0.27	0.32	0.61
	Mass (kg)	31	40	39	73	90	150
	Environmental Conditions	Operation Temp. : 0°C ~40°C Humidity : 20%~80%, Indoor use only					
	Basic Specifications	Rate : Continuous, Protection : Totally Enclosed, Non-Vented Insulation : F, Winding Insulation Test : AC1500V for one minute					
	Compatible Driver unit type	EM1006	EM1010 EP1010	EM1404	EM1410 EP1410	EP1413	EP1420
Motor Driver Coupling	Main AC Line Voltage (VAC)	3φ/1φ 220V±10% 50/60Hz or 1φ 100~128V 50/60Hz					
	Contol AC Line Voltage (VAC)	1φ 90~240V 50/60Hz					
	Main AC Line Power Cap.*2*3 (KVA)	1/2	1.5/2.5 3.5	1/2	1.5/2 3.5	3.5	4
	Max. Speed (rps)	3					
	Resolver Resolution*4 (counts/rev)	614400/153600					
	Resolver Accuracy (arc-sec)	±30					
	Resolver Repeatablility*4 (arc-sec)	±2.1/±8.4					

*1 In case of the operation at zero speed for long periods, see Megatorque motor output torque characteristics (A100 page)

*2 The first figure indicates main AC line 110V, the second indicates main AC line 220V.

*3 The second line indicates in case that the compatible driver unit is EP type.

*4 The first figure indicates 12 bit resolver resolution, the second indicates 10 bit resolution.

*5 When more load capacity is required, the additional bearing is necessary. Consult with NSK.

*6 Allowable moment load and moment rigidity are measured in case of the motor mounted on the rigid base.

SI unit System : 1N=0.102kgf=0.225lb
1N·m=0.102kgf·m=0.738ft·lb

1.5.2 Speed Torque Characteristics

(1) Driven by EM Driver unit (AC220V)

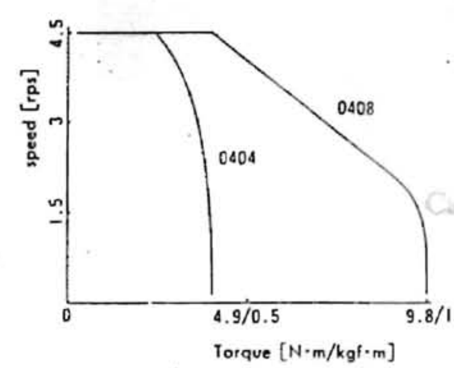

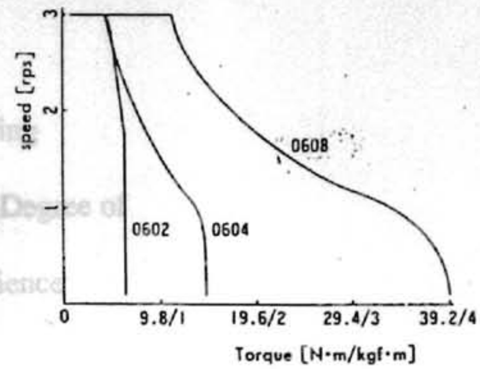

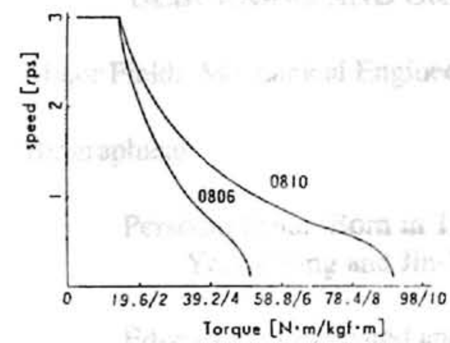

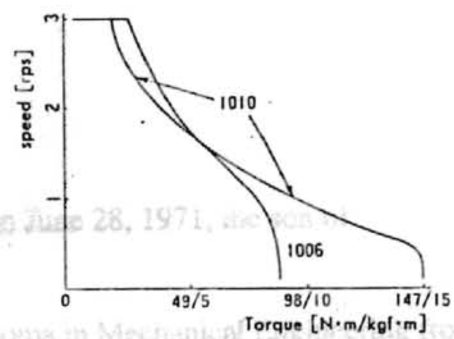

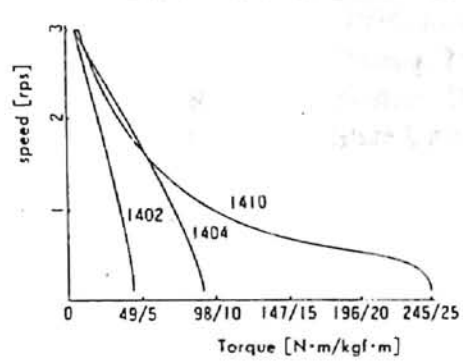

(2) Driven by EP driver unit (AC220V)

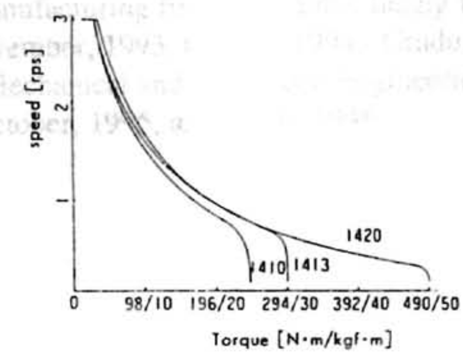

Fig.1.5

Fig.1.6

2

VITA

Kuo-Shu Ting

Candidate for the Degree of

Master of Science

Thesis: A NEW METHOD OF POSITION AND FORCE CONTROL FOR ROBOTIC DEBURRING AND GRINDING

Major Field: Mechanical Engineering

Biographical:

Personal Data: Born in Taipei, Taiwan, on June 28, 1971, the son of Yeong Ting and Jin-Yueh Lin.

Education: Graduated and received a diploma in Mechanical Engineering from Mingchi Institute of Technology, Taipei, Taiwan in June, 1991. Completed the requirements for the Master of Science degree with a major in Mechanical Engineering at Oklahoma State University in August 1996.

Experience: Engineering Intern, Formosa Plastics Group, Taiwan, ROC, from September, 1986, to June, 1991; Manufacturing Engineer, Yih-Chaung Laser Inc., Hsin-Chuang, Taipei, from November, 1993, to June, 1994; Graduate Research Assistant, Department of Mechanical and Aerospace Engineering, Oklahoma State University, from October, 1995, to August, 1996.